PROTON-AIR INELASTIC CROSS-SECTION AT THE ENERGIES ABOVE 10^{18} EV

by

Konstantin V. Belov

A dissertation submitted to the faculty of
The University of Utah
in partial fulfillment of the requirements for the degree of

Doctor of Philosophy

Department of Physics

The University of Utah

August 2005

THE UNIVERSITY OF UTAH GRADUATE SCHOOL

SUPERVISORY COMMITTEE APPROVAL

of a dissertation submitted by

Konstantin V. Belov

This dissertation has been read by each member of the following supervisory committee and by majority vote has been found to be satisfactory.

	Chair: Pierre Sokolsky
	Mikhail Raikh
	Ben Bromley
	Kai Martens
	Andrej Cherkaev

THE UNIVERSITY OF UTAH GRADUATE SCHOOL

FINAL READING APPROVAL

To the Graduate Council of the University of Utah:

I have read the dissertation of Konstantin V. Belov in its final form and have found that (1) its format, citations, and bibliographic style are consistent and acceptable; (2) its illustrative materials including figures, tables, and charts are in place; and (3) the final manuscript is satisfactory to the Supervisory Committee and is ready for submission to The Graduate School.

Date

Pierre Sokolsky
Chair, Supervisory Committee

Approved for the Major Department

Pierre Sokolsky
Chair/Dean

Approved for the Graduate Council

David S. Chapman
Dean of The Graduate School

ABSTRACT

More than 3000 extensive air showers with energies above $10^{18}eV$ were observed in stereo mode by the HiRes stereo nitrogen fluorescence detector. Energy and X_{max} were determined for each event. The proton-air inelastic cross-section was measured using the X_{max} distribution and a newly developed deconvolution method. The results are found to be in good agreement with previous measurements by AKENO and Fly's Eye.

To my wife, Polina Belova, for her endless encouragement and patience.

CONTENTS

LIST OF FIGURES

LIST OF TABLES

ACKNOWLEDGEMENTS

I wish to thank my advisor Prof. Pierre Sokolsky who guided me throughout my work. He was patient while I was "testing the waters". His advice was deeply physically motivated and always pointed me in the right direction. Thanks also to Zhen Cao. Our numerous and sometimes endless discussions contributed to the arrival of the final result.

I also wish to thank all members of the HiRes collaboration who built and maintained our cosmic ray detectors and spent sleepless nights, which always seem to be endless, collecting invaluable cosmic ray data. These highest quality data lay the foundation for this dissertation.

I owe a lot of thanks to my wife, Polina Belova, who kept supporting this "enterprise" from the beginning, when I had to move over the ocean for my graduate study, throughout many years of research, till the end, when I was writing this dissertation and did not have much time for my family again, as usual. Without her support, encouragement and endless patience this work would never have become a reality.

This research was funded by the National Science Foundation through its support of research at the University of Utah. Finally, I would like to thank the US Army Dugway Proving Ground personnel for hosting the HiRes detector sites.

CHAPTER 1

INTRODUCTION

The properties of the proton have intrigued researches since the beginning of the 20th century, when the scientific community accepted the very existence of the proton as the fundamental building block of matter. Among other proton properties, the probability of its interaction with matter, described by the term "cross-section" is of primary interest. The arrival of modern accelerators greatly increased that interest. Accelerators provide researchers with a stable beam of particles to study at any desired energy, up to the accelerator limit. That limit is currently of the order of 1 TeV for the most powerful accelerator - the Tevatron. Knowledge of the proton interaction properties at the higher energeies is crucial for our understanding of matter. Extremely high energies were dominant in the very young Universe and those very first hadronic interactions formed the world we see today. We know that particles with energies higher than 10^{20} eV do exist in today's Universe. Such particles can be found in cosmic rays (CR).

The creation and propagation of ultra-high energy CR (UHECR) is still a mystery even after a century of extensive study. Many fundamental questions remain to be answered:

- How do CR particles get accelerated to the ultra-high energies? Modern theories fall short of clearly explaining this.
- Which objects can potentially be the sources of UHECR? Some experimentalists [1] do see a correlation between CR arrival direction and some powerful cosmic objects, but others [2] do not.
- How do UHECR propagate? Charged particles with the energy above $6 \times 10^{19} eV$ should not be able to reach the earth from the distant sources if Graizen-Zatsepin-Kuzmin (GZK) cut-off, described in Section 3.2, is true [3, 4]. Yet, we do not see any powerful enough cosmic objects within GZK allowed distances.

A more detailed discussion on these and other subjects is in Chapter 3.

While still mysterious, CR are the only source of ultra-high energy particles.

1.1 Motivation

Hadronic cross-section measurements are done extensively at accelerator energies. The most puzzling discovery recently made with the help of modern accelerators is that the proton cross-section is rising with energy. In other words, the higher the relative energy of two particles the greater the chances of their interaction. Since all modern theories of proton cross-section are derived to accommodate the accelerator data and are thus empirical, none of them can accurately predict the proton cross-section at higher energies than accelerators can provide.

Few cross-section measurements done at ultra-high energies using CR data, [5, 6] seem to indicate that proton cross-section rises with energy. Limited statistics, however, as well as the measurement errors do not allow us to make a conclusion about the nature of this rising law. Statistical deficiency is mostly due to the very low CR flux at highest energies. The only way to overcome this is to build larger detectors and operate them for a longer time. An alternative can be a space based CR fluorescence detector, which has been recently proposed [7, 8]. On the other hand, there is no known way to obtain event by event measurements using CR data. Thus, the statistical nature of CR measurements, finite detector resolution combined with relatively tricky, and model dependent measurement techniques account for larger measurement errors.

The purpose of this work is to provide the very first proton-air inelastic cross-section measurement at $10^{18.5}$ eV. This measurement is done using High Resolution Stereo Fluorescence Detector (HiRes) with greatly improved energy and spatial resolution (see Chapter 5 for details about the HiRes detector). A special deconvolution method has been developed to obtain a p-air cross-section from the CR data. The new technique helps to improve systematic errors as well as reduce the model dependance. The technique is described in detail in Chapter 7.

1.2 Cosmic Ray Observations

Very low UHECR flux makes direct observations impossible. Indirect observations are done by using the earth's atmosphere as a giant detector, thus compensating for the flux deficiency. Once a high energy particle enters the atmosphere, a cascade of secondaries develops. Such a cascade can be observed by either:

- a ground array, which registers the number of charged particles (electrons and muons) at the detector level;

- a Cerenkov light detector, which measures the amount of light due to Cerenkov radiation;
- a fluorescence detector, which measures the amount of fluorescence light produced by secondary particles in the atmosphere.

A ground array usually consists of a number of scintillator counters spread over a large area in the form of a grid. Each counter measures the number of charged particles and their arrival time. The resulting air shower lateral profile at the detector level is then obtained by interpolation over all triggered counters. The scintillator counters are sometimes buried under the ground to cut off electrons and only count muons, which penetrate much deeper into the ground. The same effect can be achieved by using different shielding materials on top of the counter. The ground array can be considered a much cheaper version of one huge scintillator counter, covering a large area. Although it is very difficult to calculate the primary energy of the incident CR particle from the number and the distribution of the charged particles at only one "slice" of the shower, significant cost benefits and relative simplicity coupled with 24-hour duty cycle contributed to the recent success of the ground arrays in CR research.

A Cerenkov light detector uses the fact that CR particles are moving in the atmosphere faster than the speed of light, thus emitting a cone of light in UV range. A Cerenkov detector usually consists of several light detector stations separated by hundreds of meters. The detectors measure the amount of light and the time of arrival to each station to reconstruct the Cerenkov light cone and hence the air shower parameters. Since light flashes caused by high energy CR are still very dim, the observations are possible during only moonless nights, thus reducing the duty cycle of such a detector.

An air fluorescence detector measures fluorescence light produced by air atoms, mostly nitrogen, excited by the air shower secondary particles. Unlike Cerenkov radiation, fluorescence light is emitted isotropically, along the shower core. This allows for a precision reconstruction of the air shower profile, which is the number of charged particles vs the atmospheric slant depth. In turn, a precisely reconstructed shower profile leads to increased accuracy in the primary energy and arrival direction measurement. The shower profile has a maximum when ionization losses exceed the bremsstrahlung. This point of shower maxima is of the greatest interest in p-air cross-section measurement. It can be measured directly using the air fluorescence technique. Despite suffering from the same lower duty cycle as air Cerenkov detectors, the air fluorescence technique has given very

interesting results in the last several decades. An in depth discussion about extensive air showers initiated by UHECR is provided in Chapter 4.

A hybrid detector, which is a ground array working in conjunction with an air fluorescence detector, could improve the air shower measurements even further. The first attempt to look at the data from a hybrid detector demonstrated that two different techniques can greatly enhance each other [9].

In case of indirect observations, a special technique is necessary to obtain the results from observable data. The development of such a technique and its application to the CR data, collected by the High Resolution Fly's Eye (HiRes) stereo fluorescence detector, forms the greatest part of this dissertation.

The HiRes stereo fluorescence detector is located in Dugway Proving Ground, about 120 miles west of Salt Lake City, Utah. Dugway's desert atmosphere has proven to be better than the U.S. Standard Desert Atmosphere, containing fewer aerosols on average, thus, having a longer attenuation length for UV light. With more than 300 sunny days a year this makes the location one of the best to place a fluorescence detector.

The HiRes stereo detector consists of two detector stations, separated by 12.6 km. Such a separation makes the detector optimal for observations of the highest energy CR in stereo. Although each station can work as an independent, monocular CR detector, stereo observations greatly improve the accuracy of CR shower geometry reconstruction. This in turn leads to a better arrival direction measurement as well as better energy, and X_{max} resolution, the key measurements for the cross-section study. Only stereo CR data are used for this cross-section study. High quality stereo data, described in Chapter 6, are a step ahead compared with previous cross-section measurements [5, 6]. For a more detailed description of the HiRes stereo fluorescence detector, the reader can refer to Chapter 5.

Extensive air shower simulations were conducted in order to develop and verify the proposed measurement technique, simulate the detector response and obtain the p-air inelastic cross-section from the observable CR data. Significant improvements in the interaction models incorporated into the data simulation packages made this possible. A description of the data simulation techniques is given in Section 7.3.2.1 and in Chapter 8.

The last chapter of this dissertation, Chapter 9, is dedicated to the physics results obtained from UHECR data and their discussion.

CHAPTER 2

HADRONIC CROSS-SECTION

The cross-section is a link between theoretical models and experimental data. The cross-section is measured in units of barns. One barn equals $10^{-24} cm^2$. Thus, the cross-section is measured in units of area. However, the cross-section is a Lorentz invariant measure of the probability of an interaction in a two-particle initial state. It should be noted that the cross-section value is different for different particle species. For example, the proton-proton and the proton-air cross-sections are not equal.

2.1 Cross-Section Definitions

In case of elastic scattering, if a particle is scattered into a solid angle $d\Omega$ the cross-section is usually denoted as $d\sigma$ and is defined as:

$$\frac{d\sigma}{d\Omega} = \frac{1}{F}\frac{dN}{d\Omega}, \tag{2.1}$$

where F is the total particle flux and N is the number of particles detected within $d\Omega$. In case of a collider experiment, the value

$$L = \int \rho_1 \rho_2 u d^3 r \tag{2.2}$$

is referred to as the luminosity. ρ_1 and ρ_2 are the densities of interacting particles and u is their relative velocity. The average event rate is:

$$\frac{dN}{dt} = L\sigma. \tag{2.3}$$

In case of a fixed target experiment, we can define the cross-section as:

$$\sigma = \frac{N_{obs}}{AB\tilde{n}l}, \tag{2.4}$$

where N_{obs} is the observed number of events, A is the event loss in the experiment ($A \leq 1$), B is the effective number of particles in the beam, $\tilde{n}$ is the target number density and l

is the target thickness. The effective number of particles in the beam can be calculated using:

$$B = \int_0^l N_b e^{-\frac{x}{\lambda_1}} dx, \tag{2.5}$$

where N_b is the number of particles in the incident beam, and λ_1 is the interaction length, which is defined as the mean free path for neither elastic nor quasi-elastic interactions. The number density $\tilde{n}$ is related to the mass density of the target ρ_t as:

$$\tilde{n} = \frac{N_A \rho_t}{A}, \tag{2.6}$$

where N_A is Avogadro number and A is the atomic mass of the target. The interaction length is related to the cross-section through:

$$\lambda_1 = \frac{1}{\tilde{n}\sigma} \tag{2.7}$$

The total p-air cross-section corresponds to the following sum:

$$\sigma_{p-air} = \sigma_{p-air}^{inel} + \sigma_{p-air}^{el} + \sigma_{p-air}^{q-el}, \tag{2.8}$$

where σ_{p-air}^{inel}, σ_{p-air} and σ_{p-air}^{q-el} are inelastic, elastic and quasi-elastic portions of the total cross-section correspondingly. An inelastic interaction is an interaction that leads to new particles creation. An elastic collision is a collision in which no new particle species are born. A quasi-elastic interaction is one that does not fall into either of the two categories above. A nucleus excitation by a projectile particle would be an example of a quasi-elastic interaction. The term "inelasticity" is used to describe which portion of the primary energy particle goes to new particles creation. "Multiplicity" refers to the average number of particles created in an interaction.

Only the inelastic cross-section σ_{p-air}^{inel} can be measured using cosmic ray data. The measurement of σ_{p-air}^{inel} at ultra-high energies is the primary goal of this work.

2.2 Hadronic Interaction Models

Modeling the cross-section behavior as a function of energy allows us to extrapolate the cross-section values up to the ultra-high energies where direct cross-section measurements by accelerators are not possible. On the other hand, cosmic ray data in combination with a sophisticated measurement technique allow for an indirect cross-section measurements at the ultra-high energies. These cosmic ray measurements are not only extremely interesting

by themselves, but also greatly influence theoretical models by providing the necessary feedback.

All modern cross-section models that can be extrapolated up to the ultra-high energies are QCD inspired. They use the concept of the standard model (SM) for elementary particles and forces. In the framework of the SM, a hadron is composed of quarks. Gluons are the force-carrying particles for strong interactions between quarks and, subsequently, hadrons. A gluon or a quark are often referred as a partons. In QCD partons can form complex particles called pomerons, or parton ladders between interacting partons, see Fig 2.1. Interactions between hadrons are described in terms of pomeron exchange with so called hadronic mini-jets. Details about QCD and strong interaction models can be found elsewhere in the literature [10]. A variety of hadronic interaction models predict the atmospheric air shower profile in a good agreement with the experimental data. These models differ by their intrinsic parameters such as the hadronic cross-section, inelasticity and multiplicity. These parameters influence air shower development. Despite these intrinsic differences, the resultant air shower profiles, predicted by different models are

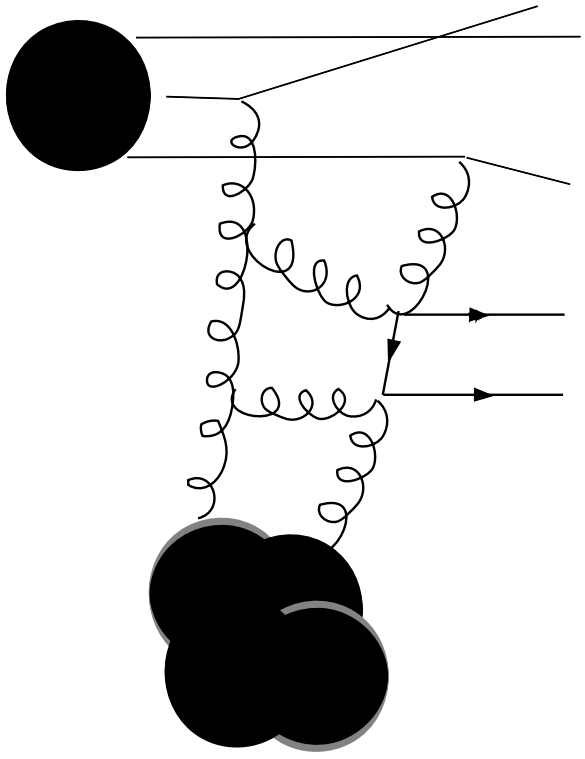

Figure 2.1. Parton Ladder.

very similar (see Fig. 2.2).

A lower inelastic cross-section in one model, for example, is compensated for by a higher multiplicity in another. This results in the number of charged particles at a particular slant depth to be similar. The cross-section values predicted by different models at accelerator energies agree very well with each other and with experimental data. This is the energy region where the models get tuned. However, the higher the energy the more divergence exists between models. This does not come as a surprise, because of the different mechanisms providing the cross-section rise with energy.

A variety of interaction models are currently under development by different theoretical groups: DPMJET 2.5 [11, 12], NEXUS 2 [13], QGSJET 01 and SIBYLL 2.1 [14, 15], HDPM [16], VENUS [17] and others. We will only briefly and very qualitatively describe the models which were used for the MC simulations for this study. The reader can find their detailed description and more references in the literature cited above.

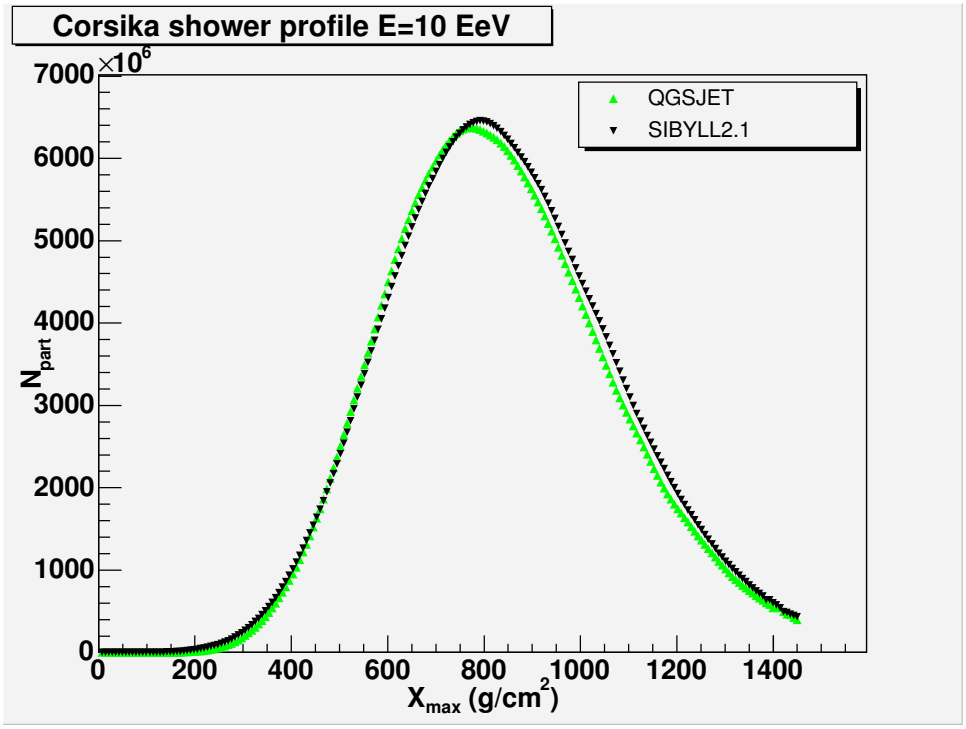

Figure 2.2. MC shower profile by different models.

2.2.1 QGSJET and SIBYLL

Two interaction models used for MC simulation for this study are the Quark Gluon String model with minijets (QGSJET) and SIBYLL. QGSJET and SIBYLL have similar underlying physics assumptions about the hadronic interactions. Pomeron exchange models the low p_T interactions. The momentum distribution functions for valence and sea quarks are determined using Regge singularities. A pair of QCD strings simulates the exchange of soft gluons that are responsible for the interactions of hadrons. Subsequent fragmentation of the QCD strings into colorless hadrons leads to new particle creation. QGSJET differs from SIBYLL by allowing multiple pairs of strings to be created. The interactions above 40 TeV in the c.m. frame are dominated by small jet production. The cross-section increase in SIBYLL is driven by the production of minijets. In QGSJET, the soft Pomeron is replaced by a "semihard" Pomeron in which a middle piece of the soft Pomeron is replaced by a QCD parton ladder. The "semihard" Pomeron produces minijets and controls the entire interaction. Due to these intrinsic differences, the model predictions about the cross-section value at ultra-high energies differ. Inelastic cross-section, multiplicity and inelasticity are the model parameters that control the shower development in the atmosphere. The lower cross-section value in QGSJET model is compensated by the other parameters resulting in very similar air shower profile predicted by both models. SIBYLL is described in detail in [14]. Ref. [15] describes the QGSJET model.

2.3 Model Predictions and Previous Measurements

The p-air inelastic cross-section values calculated using some of the interaction models are shown on Fig. 2.3. Previous cross-section measurements using CR data are shown in the same plot. As seen from the plot, all models predict cross-section values rising with energy. Predictions diverge at ultra-high energies, however. It should be noted, that previous cross-section measurements by the Fly's Eye fluorescence detector (marked as Baltrusaitis at al. in the figure, [5]) and by the Akeno ground array (denoted as Honda at al. in the figure, [6]) were performed using different measurement techniques described in [5] and [18]. In those measurements, an exponential tail of the distribution of the average depth of the shower maximum was used to obtain the attenuation length Λ, which was then related to the interaction length by means of a Monte Carlo simulation study. The resultant measurement is very sensitive to the interaction model used for the

Monte Carlo simulations. Cross-section measurements at the accelerator energies as well as theoretical research greatly influenced the interaction models. Those older results have been recently recalculated by Block [19]. As a result, the measured cross-section values have been reduced by 10-15%, (see Fig. 2.4). One of the goals of this work is to develop a measurement technique that is much less sensitive to the interaction model used for MC simulations.

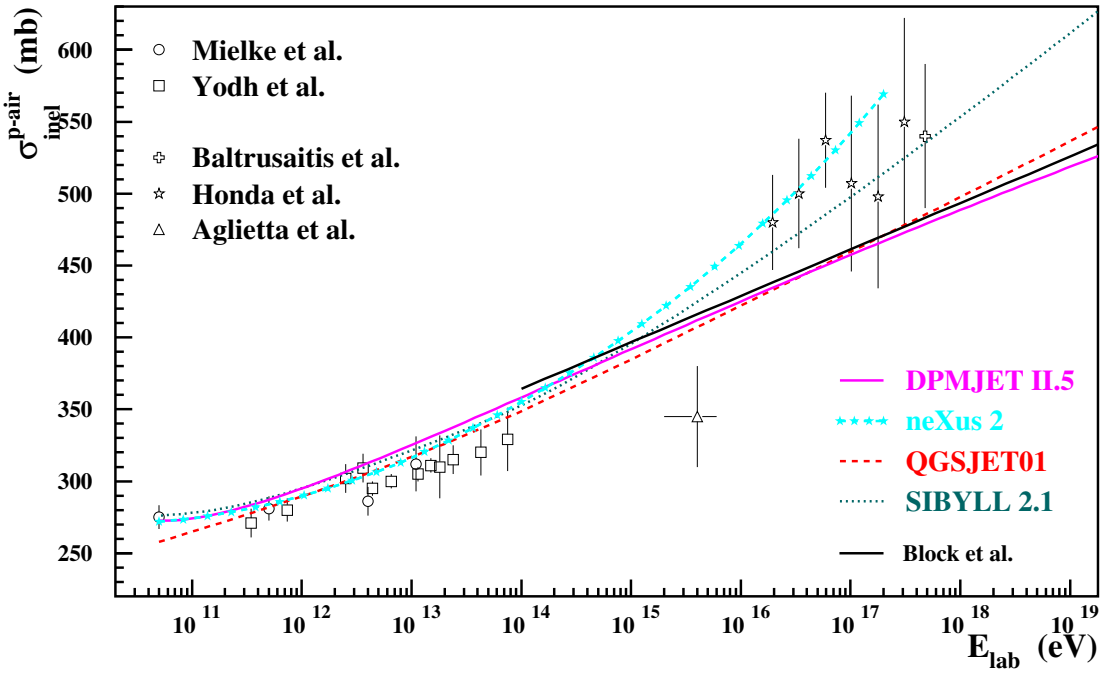

Figure 2.3. Cross-section values.

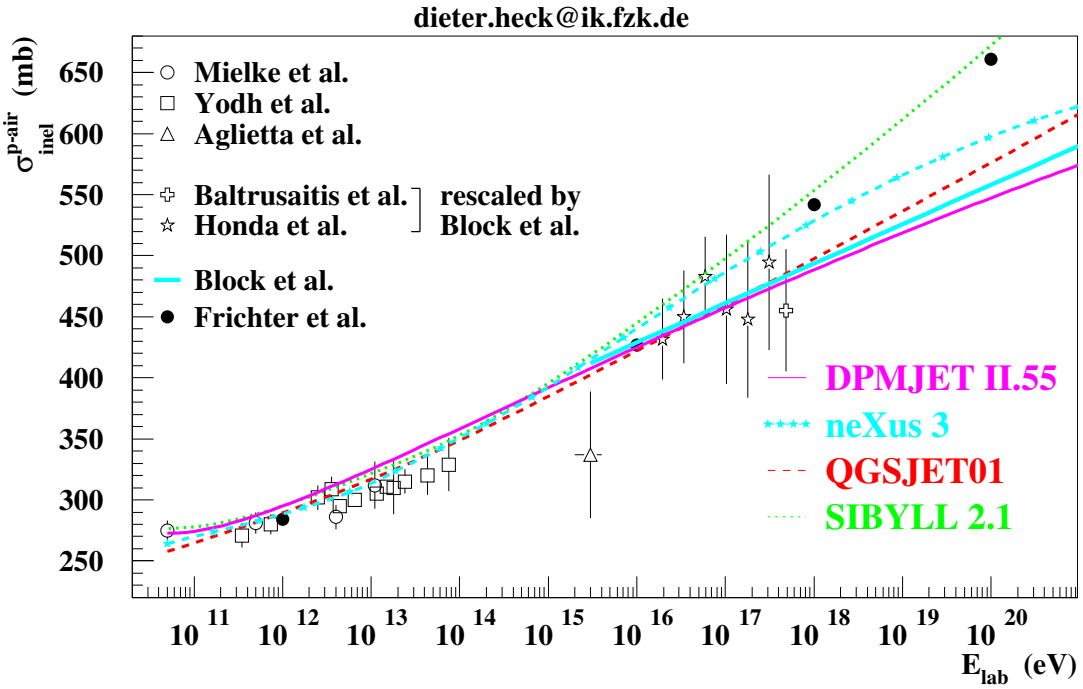

Figure 2.4. Rescaled cross-section measuremnts.

CHAPTER 3

COSMIC RAY PHYSICS

Cosmic rays (CR) are the only known source of ultra-high energy particles. Detected CR particles sometimes have energies above 10^{20} eV [20, 21], many orders of magnitude higher than the most powerful accelerators can achieve. CR origins and propagation are still a mystery. Detection of the CR poses significant challenges as well. Yet, researchers, who want to use such highly energetic particles, have no other alternative, but to turn to CR.

3.1 Cosmic Ray Origin

After about a century of CR study, there is no clear answer about the origin of ultra-high energy cosmic rays (UHECR).

One uncertainty comes from the fact, that aside from gamma rays and neutrinos, CR are charged particle, and thus are subject to a deflection by the galactic and extragalactic magnetic field. This makes CR associations with any known object extremely challenging. Another uncertainty comes from the fact that there is no established theory that could provide an acceleration mechanism responsible for the highest energy particle detected on earth. There is yet another unknown. Even if an acceleration mechanism could be found, photodisintegration should prevent particles with energies higher than 5×10^{19} from reaching the earth if they are produced at distances greater than 50-100 Mpc, so called GZK distance, see section 3.2. However, we do observe CR particles with energies more than 10^{20} [20, 21]. It implies two possibilities:

- the GZK concept is incorrect, if the particles are produced more than the GZK distance from the earth;
- UHECR particles we observe are produced within the GZK distance from the earth. This would make questionable the whole class of possible acceleration models, since we do not observe any powerful UHECR source candidate within the GZK distance.

Two major classes of CR acceleration models are currently under consideration:

- bottom up models;
- top down models.

In the case of the bottom up models, CR particles created with relatively low energy get accelerated up to the observed energies.

One of the first such scenarios was proposed by Fermi [22]. The Fermi statistical mechanism assumes that the charged particles can collide with moving magnetic clouds in interstellar space. The clouds should have much greater energy than the particles. The particles will gain energy in the case of a head-on collision, and lose energy if a following collision. The probability for a head-on collision is $(v + V)/V$ and is higher than the probability for a following collision $(v - V)/V$. Here we assume v to be the particle velocity and V to be the cloud velocity in the same reference frame. The particle would gain energy until statistical equilibrium between the degrees of freedom inside the chaotically moving cloud and the particle is reached. This puts a theoretical limit on the particle energy. A lower limit comes from the energy transfer rate. Longair [23] showed that the number of particles with energy E is proportional to:

$$E^{1+\tau/T}, \tag{3.1}$$

where T is the time a particle stays within the cloud, and $\tau = \frac{1}{4R(V/c)^2}$ with R to be the number of collisions per second. The beauty of the Fermi statistical model is the power law CR spectrum, which comes naturally here. However, because $V \ll c$ and the particle mean free part in the cloud is on the order of one parsec, the energy limit of this model falls well below the observed CR flux.

Another statistical model was proposed by Bell [24] and Blanford and Ostriker [25]. In this model, a supernova shock wave is responsible for the charged particle acceleration with a maximum energy up to 10 TeV. Ormes and Protheroe [26] demonstrated that if the ratio in the shock matter of the velocity in front of the shock to the velocity behind the shock, $V_{shock}/V_{trail} \approx 4$, then the resulting energy spectrum will be $\sim E^{-2}$. This model falls short in explaining the origin of the highest energy CR particles as well.

A galactic wind model can be considered as a development of the supernova shock wave acceleration model. The solar wind is a well-known phenomenon. A correlation between the low energy cosmic rays and the solar cycle has been found [27]. The excess of He,

N, O, Ne and Fe has also been observed [28] during the quiet period of the solar cycle. Extending the idea of the solar wind onto the galactic scale results in a similar model of CR acceleration. The galactic wind would be capable of accelerating a charged particle to much higher energies than the solar wind, as the large scale would lead to an extended time when acceleration is possible. If it exists, the galactic wind termination shock would consist of a hot gas with entrapped magnetic field lines moving at a supersonic speed. Charged particles could bounce on magnetic irregularities gaining a small energy each time. The cumulative effect, however, can be large. Jokipii and Morfil [29] estimated the resulting proton energy to be around 10 EeV. Compared to protons, iron has 26 times the charge, thus 1/26 of the gyromagnetic ratio. This would result in of about 10 times higher energy limit for iron. No such iron, however, will reach the earth due to its photospallation to protons.

Another group of the acceleration models within the bottom-up concept is direct acceleration models. Such models should have an extremely powerful electromagnetic field in order to accelerate charged particles directly up to the energy of interest. Longair [23] and Hillas [30] propose a quickly rotating neutron star with typical magnetic filed strength of 10^{12} gauss as a good candidate. The rotation period of about 30 revolutions per second translates into an electomotive force of 10^{18} eV. According to several other authors [31] an accretion disk of a black hole can generate a 10^{19} eV electromotive force. The energy loss in the high density matter surrounding the object is the main problem for all these models. The leading mechanisms for the energy loss are electron-positron production, meson photoproduction and photonuclear fission.

Recent data [20, 21] strongly suggest that CR events with the energies above 10^{20} eV do exist. The acceleration mechanisms provided by the statistical or direct acceleration models, however, fail to convince many researchers. Using realistic parameters for the fields straight and surrounding matter density for most of the models it is not possible to explain particle acceleration up to the highest observed energies. Thus, so called "top-down" models models gain more and more popularity. These models assume the existence of primordial objects taking their beginning in the early universe. When such an object decays, it undergoes a transition from an absolute symmetry state with massless particles, to the present "imperfect" Universe, where we observe broken symmetries and massive particles. Enormous energy is freed up during this transition. Some of the energy can be transferred to the observed UHECR.

The primordial objects that get most of the attention are superconducting cosmic strings, magnetic monopoles and the decay of massive particles.

The expansion of the early universe can potentially leave behind topological defects in a loop-like form of cosmic strings [32]. Magnetic monopoles are thought to be the product of this expansion as well. These defects are leftovers of the Universe's transition from a perfectly symmetric state with massless particles to the present broken symmetry state with massive particles. The existence of cosmic strings could be indirectly confirmed by the observed gravitational lensing [33], as a string would appear to the outside observer as having a very large mass. A cosmic string decay into ultra-heavy fermions and then to "ordinary" elementary particle [34, 35] could potentially create a source of UHECR.

Some authors [36] propose that the large portion of UHECR are the decay products of massive Z-bosons. The bosons are thought to be produced by scattering of ultra-high energy cosmic neutrinos on cosmological relic neutrinos. In this scenario, very distant cosmological objects are thought to be the source of high energy cosmic ray neutrinos. These cosmic ray neutrinos resonantly annihilate on the relic-neutrino background producing Z-bosons. These massive relic neutrinos form clusters of large galactic halos. They might constitute a significant fraction of the hot dark matter [37]. These Z-bosons are highly boosted with $\gamma \sim 10^{11}$. They decay instantly producing so called "Z-bursts" – collimated jets of photons and hadrons. This mechanism solves the GZK puzzle, but the required number of neutrinos is comparable with the universe's total luminosity.

Only an extensive and detailed study of the CR energy spectrum can bring us closer to understanding of which model or combination of models can best explain the production of UHECR.

3.2 Cosmic Ray Propagation

In order to reach the earth, CR particles born in our galaxy have to travel throughout the interstellar medium, or through the interstellar medium of their native galaxy, the intergalactic medium and through the interstellar medium of our galaxy. They will mostly encounter dust and gas clouds, magnetic fields and photons on their way.

The magnitude of chaotic and regular galactic magnetic fields is though to be about the same, on the order of few microgauss. Apart from simple bending of the CR trajectories, a diffusive motion of the CR particles will be produced by these fields. Although not very important for EeV particles and above, this diffusion can significantly affect the lower

energy ones. A PeV particle would have to travel through about 10 g/cm^2 of matter at galactic distances [38]. The proton has about 70 g/cm^2 mean free path at these energies and will not be affected. The effect on the heavier nuclei will be much more pronounced as their mean free path is comparable with 10 g/cm^2. This, in turn, will affect the composition of the CR arriving at the earth.

Since the intergalactic magnetic fields are estimated to be 1/100 of the galactic ones, they should not significantly deflect particles with energies of 30 EeV and above. A typical CR particle travels through 0.2 g/cm^2 of matter in intergalactic space [38], thus the probability of interaction can be safely ignored. However, relic radiation can alter the CR spectrum at the high end. This possibility was originally suggested by Greisen [3] and, independently, by Zatsepin and Kuzmin [4] in 1966. The density of the relic photons is about 500 per cm^3. Their 2.7 K temperature would translate to about 10^{-4} eV in laboratory reference frame, but will be as high as 300 MeV in the 50 EeV proton reference frame. 300 MeV is the threshold for $N^*(1236)$ resonance production:

$$\gamma + p \rightarrow N^*(1236) \rightarrow^{n\pi^+}_{p\pi^0} \tag{3.2}$$

which will be followed by:

$$\pi^+ \rightarrow \nu_\mu \mu^+ \rightarrow \nu_\mu \overline{\nu}_\mu \nu_e e^+ \tag{3.3}$$

or by:

$$\pi^0 \rightarrow \gamma\gamma. \tag{3.4}$$

Three neutrinos or two photos will be produced as a result of this interaction. Since the interaction is inelastic, the primary proton will lose energy and one should expect a cutoff of the CR spectrum observed from the earth at about 6×10^{19} eV.

3.3 Observed Cosmic Ray Spectrum

Although CR spectrum is not central for this thesis, it is too important and too unique to be skipped.

The observed CR spectrum is shown in Figure 3.1. The spectrum is the compilation by S. Swordy, the Unoversity of Chicago, of several measurements by different experiments, [40, 41, 42, 43, 44, 45, 46]. The most noticeable features of the CR spectrum are:

- steeply falling power law flux;
- clearly observed points at which the spectral index changes.

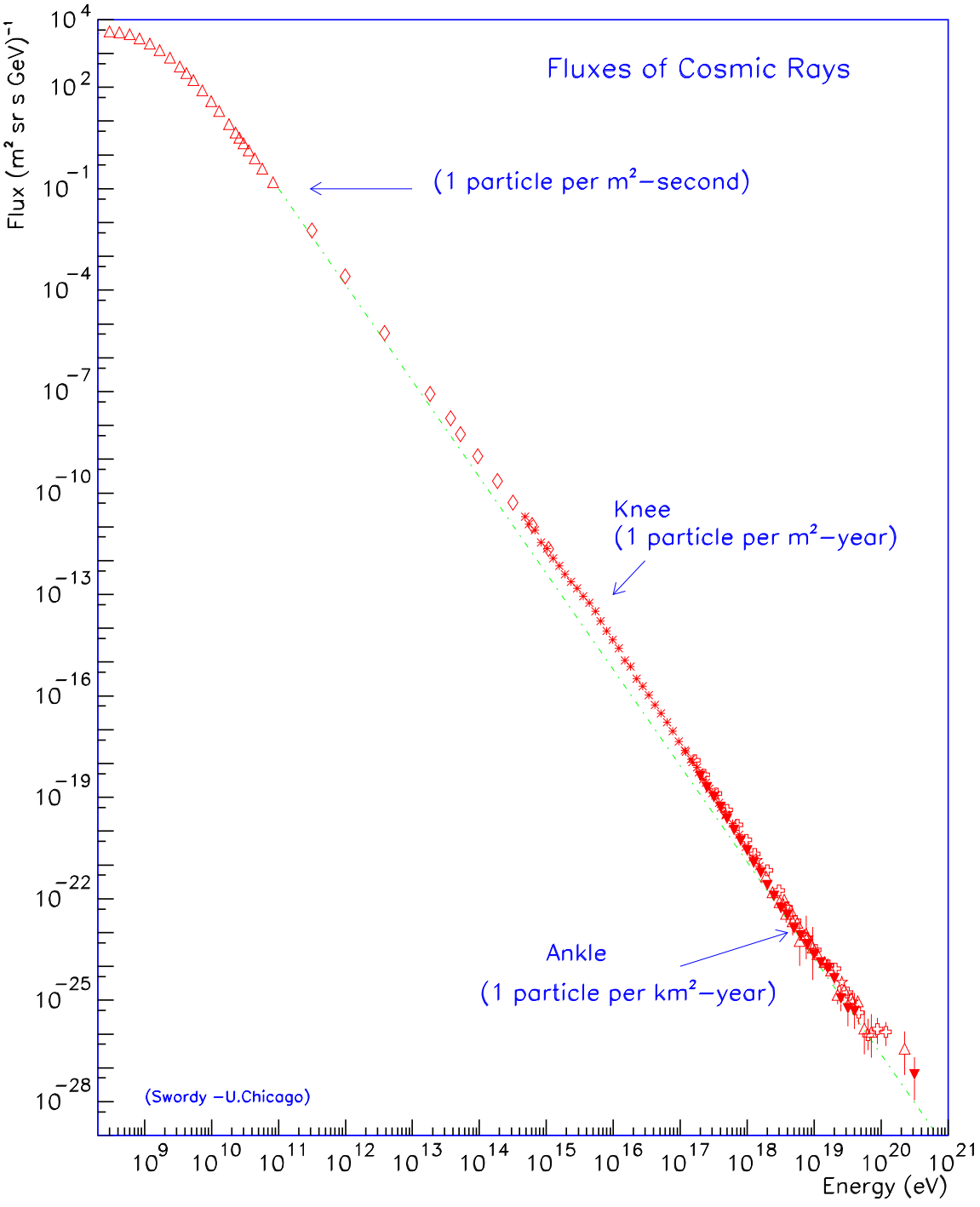

Figure 3.1. Measured cosmic ray spectrum. Adapted from [39].

The measured flux spans many orders of magnitude. The spectrum follows approximately E^{-3} power law with clearly visible changes at around $10^{15} - 10^{16}$ eV, referred to as the "knee" and around 10^{19}, referred to as the ankle. The slope change at the knee is from about -2.7 to -3.1. with the slope recovering at the ankle. These spectrum features can provide important information about CR sources and CR propagation. In a simplified approach, one can say that the knee can be attributed to exhaustion of the statistical acceleration mechanisms to push the particles beyond $10^{15} - 10^{16}$ eV. On the other hand, the gyroradius R_g can be calculated as:

$$R_g = \frac{m\gamma v}{ZeBsin\theta}, \tag{3.5}$$

where B is the magnitude of the magnetic field, m, v and Z are the particle mass, velocity and charge correspondingly, γ is the Lorentz factor and θ is the angle between the particle direction of movement and the magnetic field. The magnetic field can be estimated using Zeeman splitting of the 21 cm hydrogen line or Faraday rotation or the alignment of dust. The spin axis of the aspherical dust grain should align along the direction of the ambient magnetic field due to the paramagnetic relaxation [47]. According to [23] it has a magnitude of about $1 - 10 \times 10^{-6} G$. A $10^{18} eV$ proton would have $R_g \sim 500$ parsecs. This is about the thickness of the galactic disk. Thus, protons of this energy would have a chance to escape the Galaxy and one should definitely expect some change in the spectrum around this energy. This is often referenced as the "leaky box" model. According to [48], the power needed to maintain the present day galactic cosmic ray flux is about 1.5×10^{41} erg/s, which constitutes about 1/3 of the total power provided by the galactic supernovas. Supernova shock, however, can not be responsible for particle acceleration to energies higher than 10^{16} eV [49].

Finally, many detected events with energy above 10^{20} eV stimulate discussions about the GZK cutoff validity and push for alternative acceleration mechanisms hunt. A rebound of the spectrum above the GZK cutoff would indicate that top-down acceleration mechanisms are present.

W. Springer [50] used HiRes stereo data in his recent work on the CR energy spectrum at $10^{18.5}$ eV and above. Figure 3.2 shows that part of CR flux consistent with the flux predicted by GZK cutoff. The spectrum measured by AGASA [21] does not indicate any cut-off however. The two experiments use different technique that can contribute to the controversy. More statistics is needed to make a finale decision about GZK cutoff very existence and its influence on the UHECR spectrum.

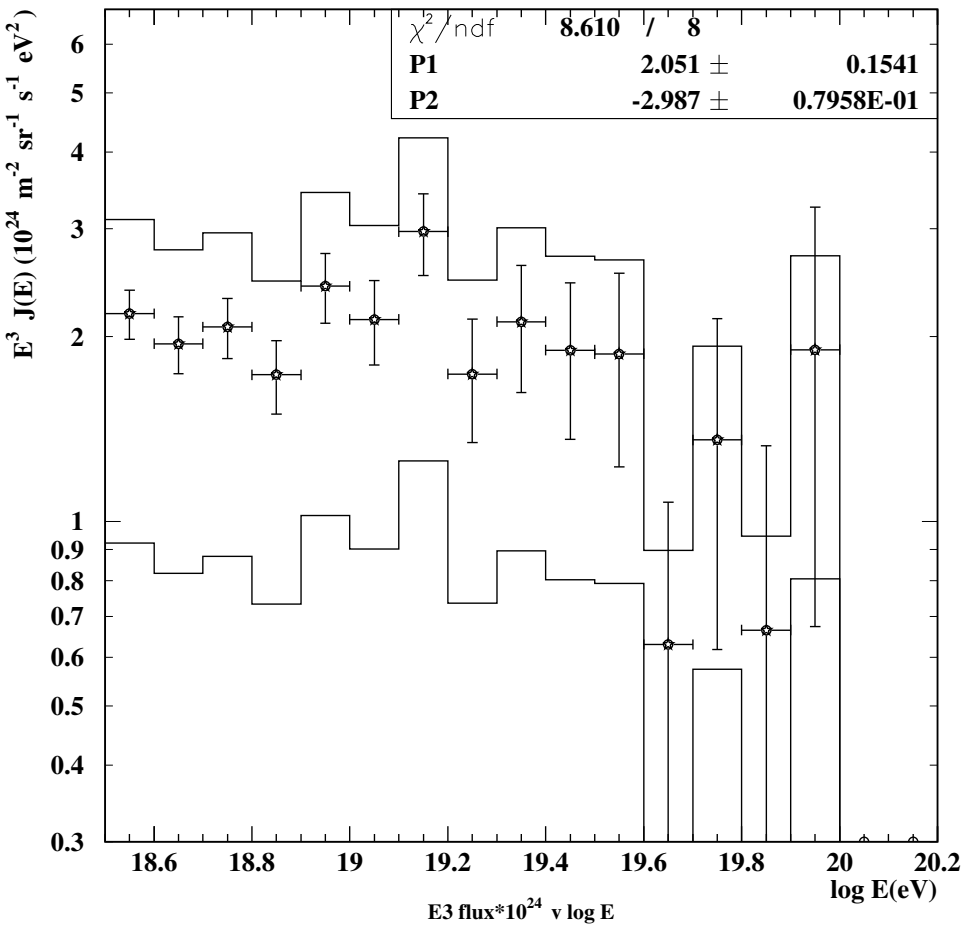

Figure 3.2. Cosmic ray flux above $10^{18.5}$ eV. HiRes stereo preliminary measurement, [50].

3.4 Observed Cosmic Ray Composition

The observed CR composition is very important for this cross-section study. Fortunately, there is an indication that the composition is predominantly light at the energies of interest. This means that CR flux is dominated by protons at 10^{18} eV and above. The most recent HiRes composition study [51] indicates that there might be not more than 20% of heavy nuclei at 10^{18} eV and above. Figure 3.3 shows the measured mean value of X_{max} as a function on energy. Modeling with QGSJET interaction model results in two bounding curves, shown in the Figure 3.3 as well. The upper curve is for pure proton composition, while the lower one is for pure iron composition. Based on this study, one can conclude that the UHECR composition is slowly changing and predominantly light.

For this cross-section study, it was assumed that iron contributes no more than 20% at 10^{18} eV. More composition studies have to be done in order to confirm and refine the above numbers.

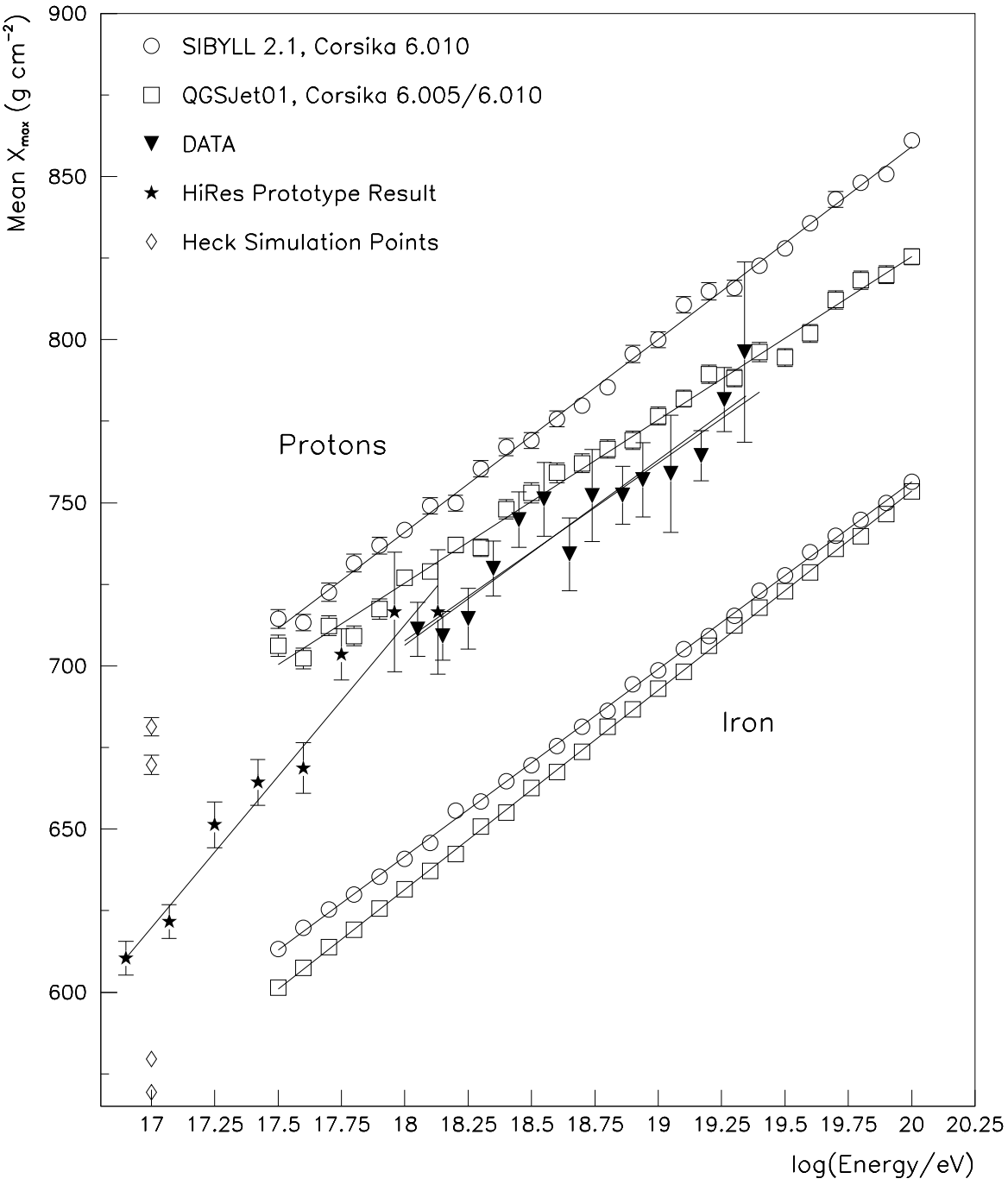

Figure 3.3. UHECR composition.

CHAPTER 4

EXTENSIVE AIR SHOWERS

UHECR measurements are indirect. The properties of the CR particles have to be studied using secondary products of their interaction with the air molecules. The fluorescence technique, as well as the ground array measurements, rely completely on the measurements of extensive air showers, produced by the primary CR particles. The extensive air showers produced by UHECR in the earth's atmosphere are the primary subject of this chapter.

An extensive air shower starts when a relativistic CR particle interacts with an air nucleus. In 78% of cases the target is a nitrogen nucleus. The primary particle interactions with the air nuclei lead to the primary particle energy loss and the production secondary particles. The subsequent decay and interaction of secondary particles creates a cascade – an air shower. The number of charged particles can reach 10^{11} at shower maximum for a 10^{20} eV primary. The shower can be kilometers long in the atmosphere and can laterally extend to hundreds of meters at ground level. The charged particles can be detected on the ground by particle counters arranged in large arrays. As the shower develops, Cherenkov light as well as scintillation light is emitted. Both can be seen by UV sensitive detectors on the ground or from space.

Unlike an accelerator experiment, where all or most secondaries can be accounted for and the initial energy can be reconstructed, CR experiments rely on statistical models of the showers to obtain the parameters of the primary interaction. Such models are usually a combination of phenomenological description of the shower development and fundamental knowledge of the particle interactions. Even then, it is not possible to determine the primary composition on event by event basis. The models are usually implemented in specialized Monte Carlo simulation packages like COSMOS [52], CORSIKA [53], AIRES [54]. The shower parameters used for Monte Carlo simulation are also used to reconstruct real CR events.

Three major components are used to describe air shower development:

- hadronic core;
- an electromagnetic cascade.
- a muonic component;

The hadronic shower is fed by the first two components, through the decay of neutral and charged particles correspondingly. The decaying particles are pions and kaons in both cases, where the most energy of the initial impact ends up. Charged pions decay into muons and neutrinos with a branching fraction of 99.987%. Weakly interacting neutrinos have almost zero chances to be detected from subsequent interaction until they reach the ground. The energy loss to neutrino can be estimated using only theoretical models. Muons can be detected on the ground. Neutral pions decay into two photos with subsequent pair production and bremsstrahlung.

4.1 The Shower Hadronic Core

Strong interactions are dominant in the hadronic core. The first interaction of the primary nucleon with the target will produce mostly pions and kaons. Pions will account for about 2/3 and kaons for about 1/10 of the debris [55]. The rest are neutrons, protons and other nucleons. Particle inelasticity, multiplicity and cross-sections are used to describe the strong interactions. Inelasticity is the fraction of energy available for particle production in the laboratory reference frame. Multiplicity is the number of particles produced as a result of the interaction. The multiplicity is different for different particle species. The interaction cross-section describes the probability for a particular interaction. An inelastic cross-section, thus, would describe the probability of an inelastic interaction, an interaction when new particles are born. The inelastic cross-section very much determines the shape of the air shower. The physics behind strong interactions is not yet completely understood. Thus, such parameters as inelasticity, multiplicity and the cross-section can not be directly derived from modern QCD theory. Phenomenological models are used to predict these parameters. These models are designed to fit the accelerator data, when direct measurements are available. Extrapolation of these models several orders of magnitude in central mass energy up to UHECR energies can not be guaranteed accurate. Different models predict different extrapolated values for the above parameters.

A simple superposition model such as the wounded nucleon model is used to describe air showers produced by nuclei. Such a shower is considered to be a superposition of A showers each with energy E/A, where A is the atomic mass and E is the primary energy. Strong forces have a very short range. The proton will interact with some nucleus inside the target nuclei. A wounded nuclei model takes into account the short range nature of the strong forces introducing "wounded" nucleons – those that participate in the interaction. Because a nucleon binding energy is only about 8 MeV, we can assume that the proton interacts independently with wounded nucleons. Mathematically it is described by the Glauber multiple scattering formalism. This model predicts that the nuclei initiated showers develop earlier in the atmosphere and have lesser fluctuations than the proton initiated ones. Another approach is a "fragmentation" model [56]. This model is derived from low energy cosmic ray data analysis and correctly describes the average shower behavior, but results in larger fluctuations [57].

4.2 The Shower Muons

The charged pions will decay via:

$$\pi^{\pm} \rightarrow \mu\pm + \nu \tag{4.1}$$

The branching fraction for this reaction is .99987. Thus, almost all charged pions will decay this way. Even taking into account time dilation, only a handful of charged pions will reach the ground. Muons, however, can be easily detected by ground arrays. Some energy will be lost to neutrinos. This energy loss estimation is model dependent.

4.3 Electromagnetic Cascade

The neutral particles decay:

$$\pi^0 \rightarrow \gamma + \gamma \tag{4.2}$$

starts the electromagnetic cascade. The shower grows through the pair production:

$$\gamma \rightarrow e^- + e^+ \tag{4.3}$$

and bremsstrahlung:

$$e^- \rightarrow e^- + \gamma \tag{4.4}$$

or:

$$e^+ \rightarrow e^+ + \gamma. \tag{4.5}$$

Electrons can be detected by a ground array. Because UHECR particles are moving through the atmosphere faster than the speed of light, they produce Cherenkov radiation. CR particles also produce fluorescence (scintillation) light, by exciting Nitrogen atoms, (see section 4.4). Both Cherenkov radiation and scintillation photons can be detected by UV sensitive telescopes.

The turning point in the shower growth is when the energy loss via ionization exceeds the energy loss via bremsstrahlung. At this point, the shower will start to diminish. Muons, however, have a relatively long half-life and small ionization losses. As a result, the muon number as a function of atmospheric depth will not drop as fast as the number of other charged particles.

4.4 Air Fluorescence

Data used in this analysis were collected by the HiRes – an air fluorescence detector. It measures scintillation light in the atmosphere, which is used as a giant calorimeter. Excited nitrogen molecules are the primary source for the atmospheric fluorescence. Charged particles of the shower e-m cascade (see the previous section) excite air nitrogen molecules, which in turn emit the fluorescence light. The spectrum of this emission is in the near-ultraviolet region (300-400 nm). The atmosphere has very low absorbtion in this region. A scattering length exceeds 25 km. The fluorescence yield (the number of photons emitted per meter per ionizing particle) is almost independent on the altitude up to about 15 km. This makes the air fluorescence an ideal tool for CR study. A measured air fluorescence yield spectrum is shown in Figure 4.1. The intensities are normalized to 1.0 at 337 nm. A precise knowledge of the fluorescence yield spectrum is crucial for the accurate measurement of the CR spectrum. A new experiment [59] is under way to improve the accuracy of the previous fluorescence yield spectrum measurements.

A detailed discussion about the air fluorescence and its application to CR study is given in [60].

4.5 Air Shower Parameters

The shower parameters that are subject to study include:

- the longitudinal development profile;
- the lateral particle density distribution;
- the point of first interaction;

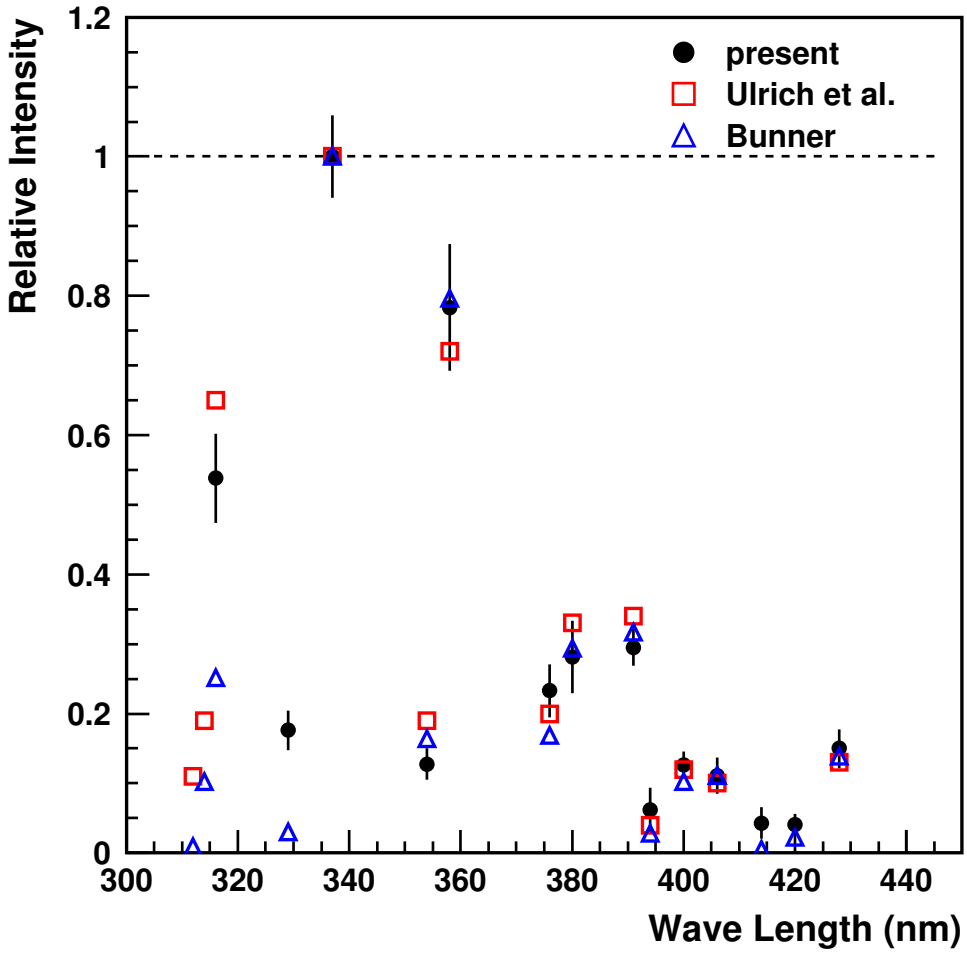

Figure 4.1. Relative photon intensities in air at 1013 hPa. Adapted from [58].

- the depth of the shower maximum.

These parameters are described in detail in Chapter 8.

CHAPTER 5

HIRES STEREO FLUORESCENCE DETECTOR

The purpose of this chapter is to give the reader a general idea about the High Resolution Fly's Eye Stereo Fluorescence Detector design, operation and calibration. The detector improvements and additional calibration attempts made since previous HiRes Collaboration publications are given a deeper look. For detailed information about the detector and the calibration procedures, the reader is referred to [61].

5.1 High Resolution Fly's Eye Stereo Fluorescence Detector

High Resolution Fly's Eye Stereo Fluorescence Detector (HiRes stereo) consists of two detector stations (eyes) located in the Western Utah Desert and separated by 12.6 km. The detector eyes were commissioned at different times. HiRes1 was commissioned in 1997, and HiRes2 went online in December 1999. The later date is also the starting point for stereo observations.

Several physics and budgetary considerations played their role in the detector site selection:

- generally very good weather means more high quality data and less complications during the data processing;
- the clear Utah atmosphere has on average fewer aerosols than the U.S. Standard Desert Atmosphere, and thus has less attenuation in the UV – a great advantage for a fluorescence detector;
- since the aerosol concentration drops with height above ground, placing both detector stations on top of the hills reduces the aerosol influence even further;

- HiRes1 occupies the same hill where the HiRes Prototype Detector and The University of Utah Fly's Eye detectors were previously located, thus utilizing the existing infrastructure;
- the separation between HiRes1 site and the newly selected HiRes2 site makes a stereo aperture appropriate for observations of CR with energies above 10^{18} eV.
- a reasonably easy road access to the top of both hills helped to keep infrastructure investments at minimum.
- because both sites are located at Dugway Proving Ground, which is a U.S. Military base, security is not an issue.

Each detector eye can operate independently, in monocular mode. Stereo mode however is the preferred one as it greatly improves the resolution of the key CR measurements done by the detector. Below is a more detailed description of both detector eyes.

5.2 HiRes1

The Hires1 detector is located on the top of Little Granite Mountain in Dugway, Utah. It succeeded the High Resolution Prototype Detector, which, in turn, was built on the same basic principals as the very successful University of Utah Fly's Eye detector, which was in operation from 1981 to 1992 [62]. "HiRes" class of detectors employs bigger stationary mirrors, photo-multiplier tubes (PMT) with a smaller field of view ($1^\circ \times 1^\circ$) and more advanced, sample and hold (s/h) type of electronics. The HiRes Prototype Detector was operational from 1994 to 1996 at the same location. It had 14 mirrors in five "rings", covering a field of view from 3° to 60° in elevation. A detailed description of the HiRes Prototype detector can be found elsewhere [63]. Mirrors looking at higher elevation contribute much less to the CR event rate, especially for highest energy events, which tend to develop air showers deeper in the atmosphere. The decision was thus made to build a "one ring" detector with azimuthal coverage of almost 360°. Its one ring field of view is from 3° to 17° in elevation. The lower field of view boundary reduces the effect of low level aerosols.

The HiRes1 detector consists of 20 almost identical units, usually referred as mirrors, a central timing and a YAG laser calibration system. Each mirror includes a spherical mirror, a photo-sensitive camera and an electronics rack. The entire detector is controlled by a central computer utilizing an Ethernet network. A schematic detector layout is shown

in Figure 5.1. The detector mirrors are sheltered in standard garage buildings, like the one shown in Figure 5.2, usually in pairs. The buildings are scattered on the top of the hill. Figure 5.3 shows the detector infrastructure on the hill. Several complementary systems provide crucial weather information and serve the purpose of calibration. The major detector components are described below.

5.2.1 Mirror

The purpose of the HiRes mirror is to collect UV light and to focus it on a sensitive camera. The HiRes mirrors are spherical, made of four cloverleaf shaped glass segments coated with aluminum. The total mirror area is 5 sq.m. The mirror form, camera obscuration and spaces between PMTs reduce the effective mirror area to 3.84 sq.m.

5.2.2 UV Sensitive Camera

The main sensitive element of the HiRes detector is its UV camera. The UV camera consists of 256 PMTs arranged in 16×16 grid called clusters, (see Figure 5.4). The field

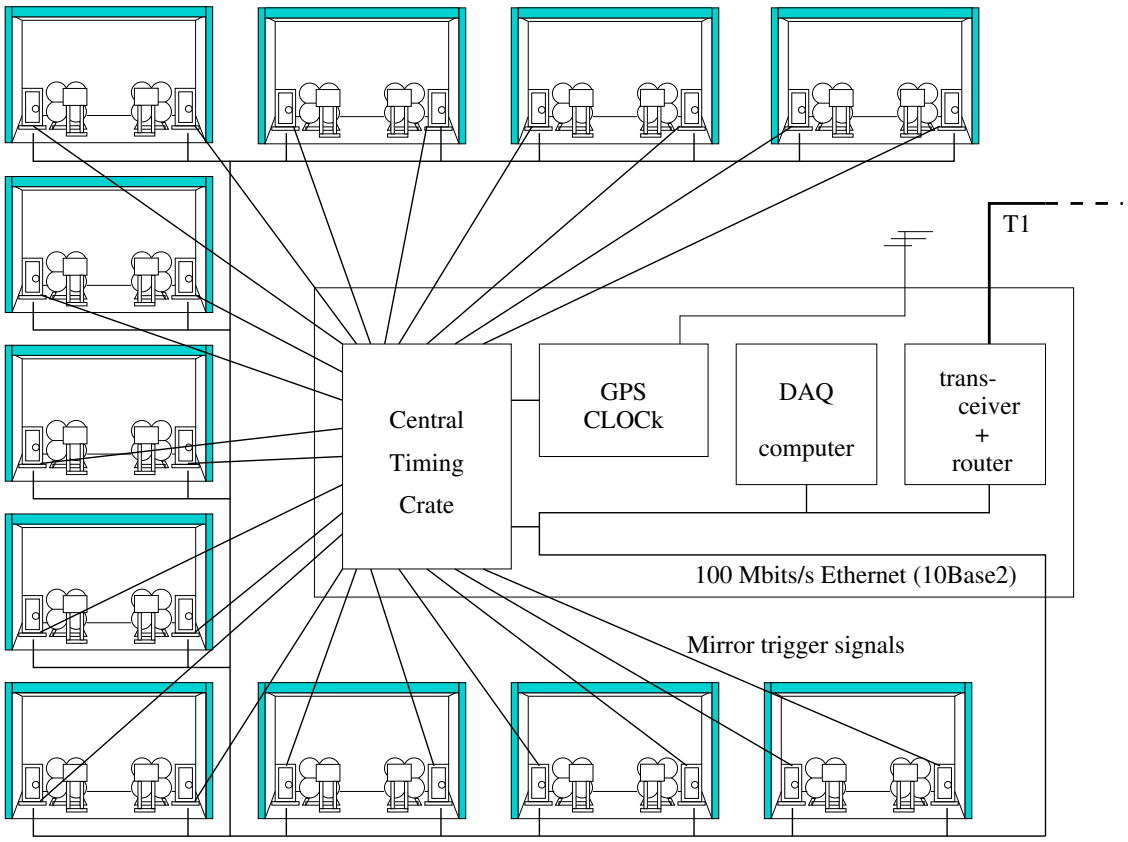

Figure 5.1. BigH detector schematic diagram.

Figure 5.2. HiRes mirror shelter.

of view of each PMT is approximately 1°. Tightly packed into the cluster, they provide about 16° × 14° field of view for the camera. EMI and Philips PMTs are used in HiRes1 clusters. Both types have very similar parameters. Each PMT had been thoroughly tested before installation into the cluster. PMTs have maximum light sensitivity in the UV range. However in order to further reduce the skynoise, a narrow band UV filer is placed in front.

5.2.2.1 PMT

A PMT is the main sensor of the detector. The PMT is an electronic vacuum tube, with a hexagonal window – photocathode and a chain of cathodes (see Figure 5.5). A voltage of about 1000 V is distributed over the cathodes, as shown in the Figure 5.6. A photo-electron produced by the photocathode is multiplied by the cathode chain by about 5–6 orders of magnitude, producing a charge pulse. The PMT gain dependance on the applied voltage can be described by an empirical formula:

$$G = V^{\beta} e^{\alpha}, \tag{5.1}$$

where V is the applied voltage, the parameters α and β are determined during PMT scanning, as described in section 5.4.1.1.

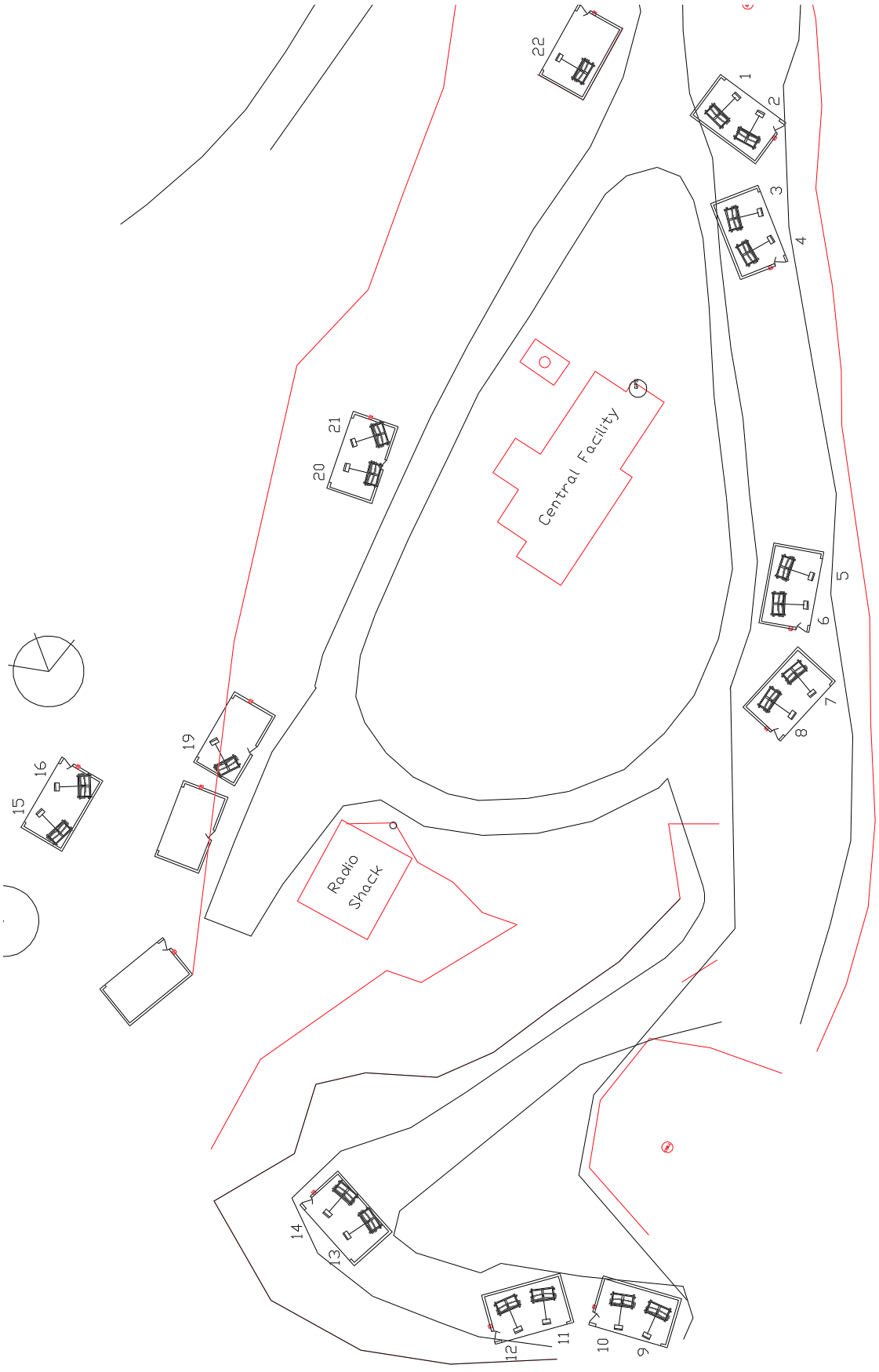

Figure 5.3. BigH detector layout.

Figure 5.4. Main detector camera.

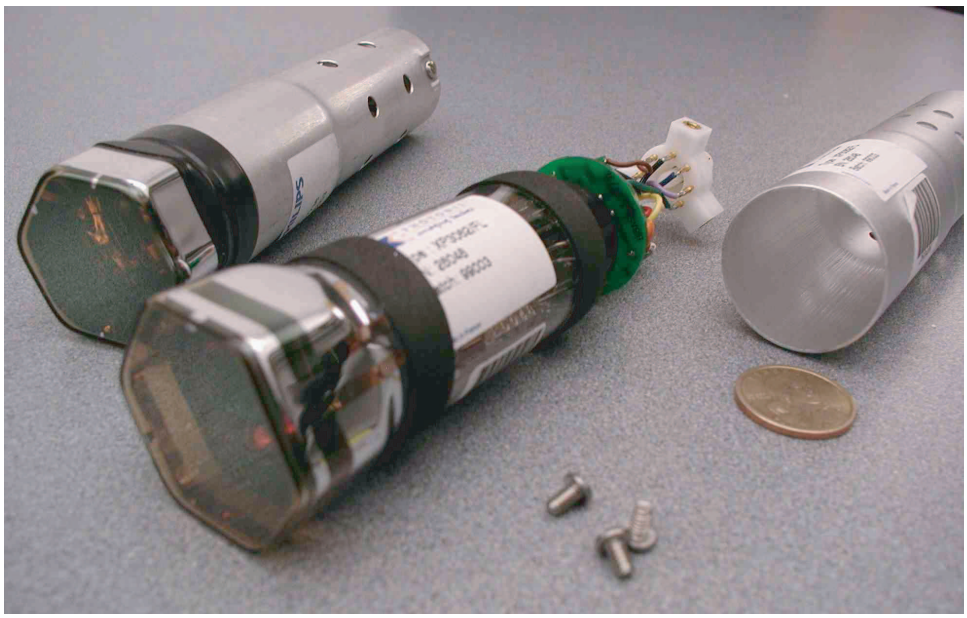

Figure 5.5. Photo multiplier tube.

The signal pulse, amplified by a preamplifier, enters the OMB (see Section 5.2.3) for further processing.

5.2.2.2 UV Filter

A UV filter is placed in front of each detector camera in order to cut off the visible light and reduce sky noise. Figure 5.4 shows the main detector camera with the open UV filer. The filter transmission is shown in Figure 5.7.

5.2.3 Electronics Rack

A HiRes Electronics Rack holds high and low voltage power supplies as well as all mirror readout system:

- a main CPU board with Motorola 68030 processor;
- a“garbage” board;
- 16 readout boards, called ommatidial boards by analogy with ommatidial nerves in fly’s eye;
- a trigger logic board;
- a PPG board.

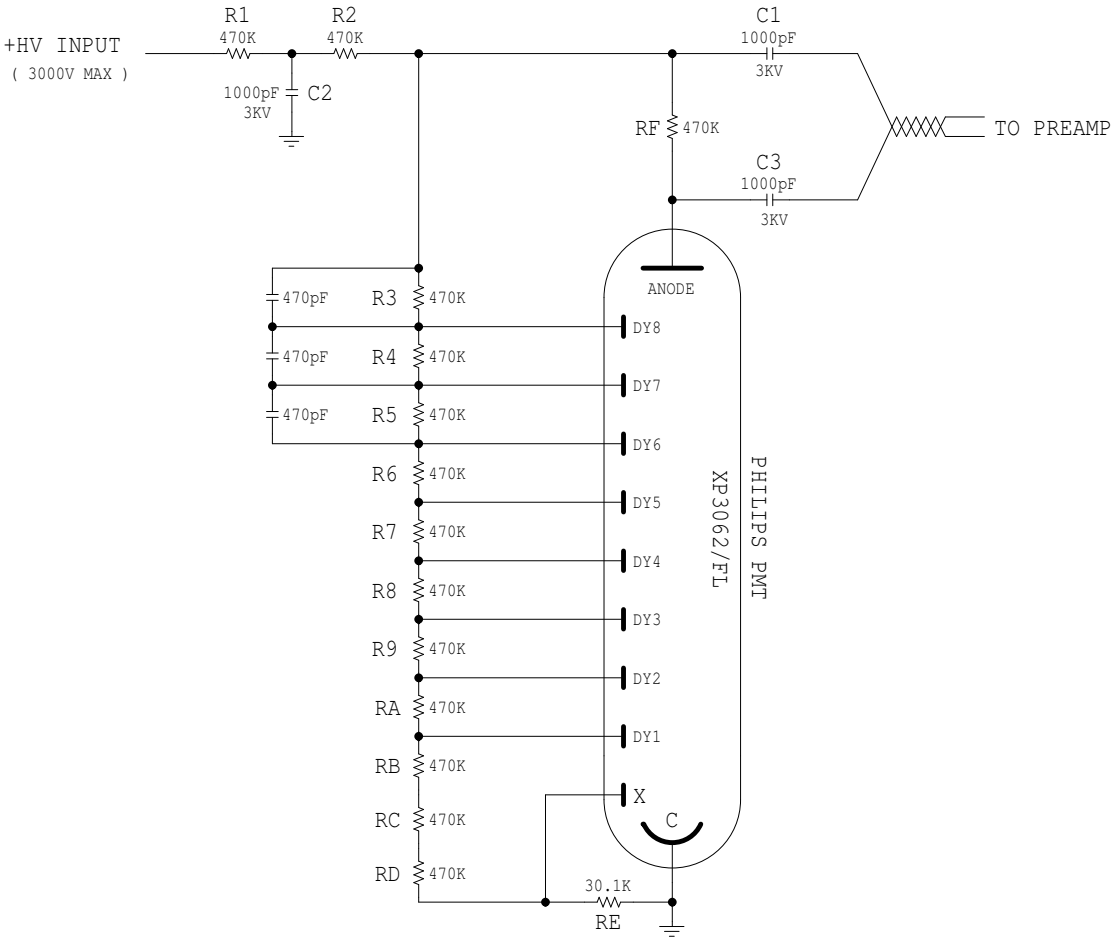

Figure 5.6. HV diagram.

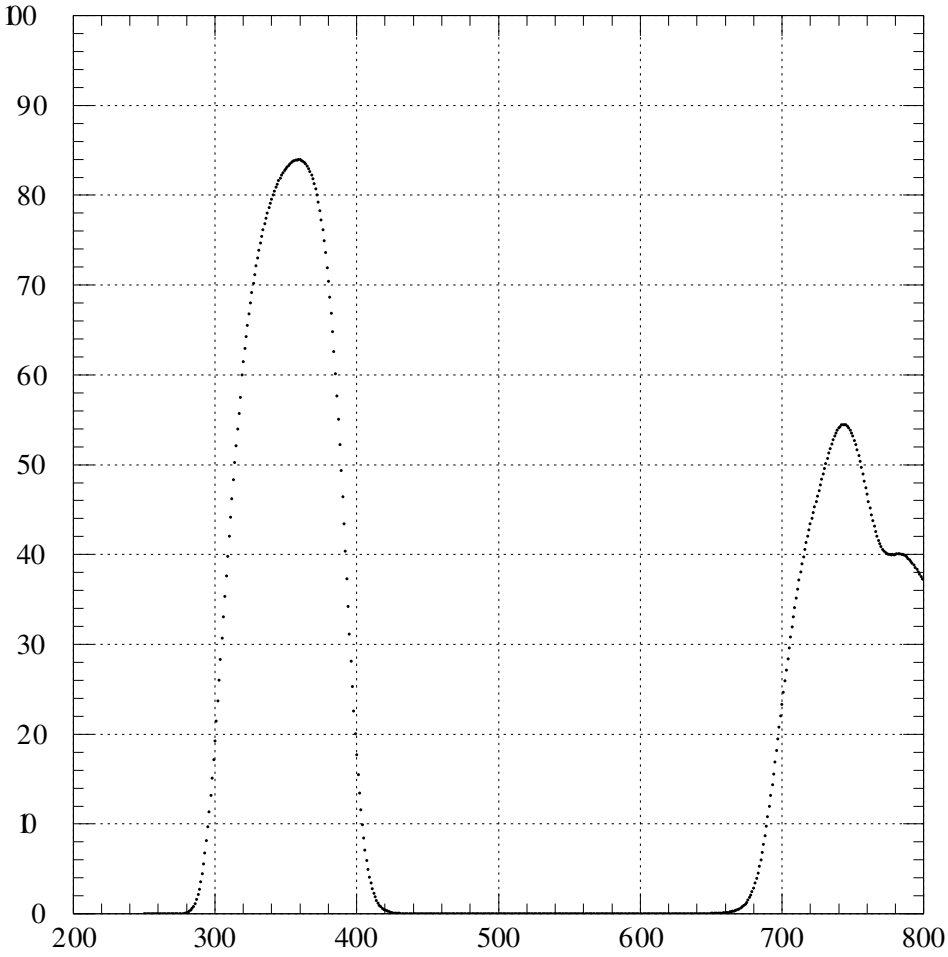

Figure 5.7. UV filter transmission.

The electronic rack diagram is shown in Figure 5.8. The CPU board is the main processing and communication center of the mirror electronics. The ommatidial boards (OMB) contain secondary amplification, integration and analog to digital conversion (ADC) circuits as well as the trigger circuits. Each OMB controls a 4×4 matrix of tubes, called a subcluster. The OMB also has a trigger logic microcontroller. The functions of the garbage board include numerous diagnostic readouts, temperature monitoring and the door control. The trigger board makes the trigger decision on the mirror level. A programmable pulse generator (PPG) is located on a separate board. It serves as a diagnostic and a calibration tool by injecting various length and amplitude pulses into the HiRes electronic channels.

There are two versions of the HiRes electronics in operation: Rev.3 and Rev.4. In the case of a Rev.4 mirror, integration channel A with a 100 ns low-pass filter and a 600 ns delay line and channel B with 375 ns low-pass filer and 1600 ns delay line are used simultaneously. These mirrors utilize a 16-bit ADC. Rev. 3 mirrors use only one channel B identical to the channel B of Rev. 4 mirrors. A 12-bit ADC is used in Rev.3 mirrors. The rest of the electronic circuitry is identical for both revisions of the HiRes electronics. The HiRes1 electronic channel is shown in Figure 5.9.

The basic mirror operation logic is as following. The PMT signal is first amplified by a preamplifier, mounted on the back of each PMT. The PMT signal is than directed into channel B of Rev.3 mirrors or channels A and B of Rev.4 mirrors. Channel A of the Rev. 3 mirrors is not used. See Figures 5.10 and 5.11.

After getting through the low-pass filter, the signal is analyzed by a tube trigger module. If the signal is above a threshold, than the trigger module flips to the "trigger" state and the signal integrator is started. To insure the integration of the entire pulse, the PMT signal arrives at the integrator with a delay. The integration gate is $5.6\mu sec$. The tube is kept in the trigger state for $25\mu s$, called a "hold-off" time. The tube can not be triggered again during this time. The OMB will keep the charge and timing information for each triggered tube during the hold-off time. The information about all triggered tubes within the subcluster is analyzed by a 64K ROM microcontroller, shown in Figure 5.12, which serves as a lookup table. To trigger a subcluster, it has to have three tubes triggered with two being hexagonally adjacent. The subcluster will remain in the triggered state as long as the trigger conditions are satisfied. The subcluster trigger signal is sent to a mirror trigger board, shown in Figure 5.13, which is another 64K

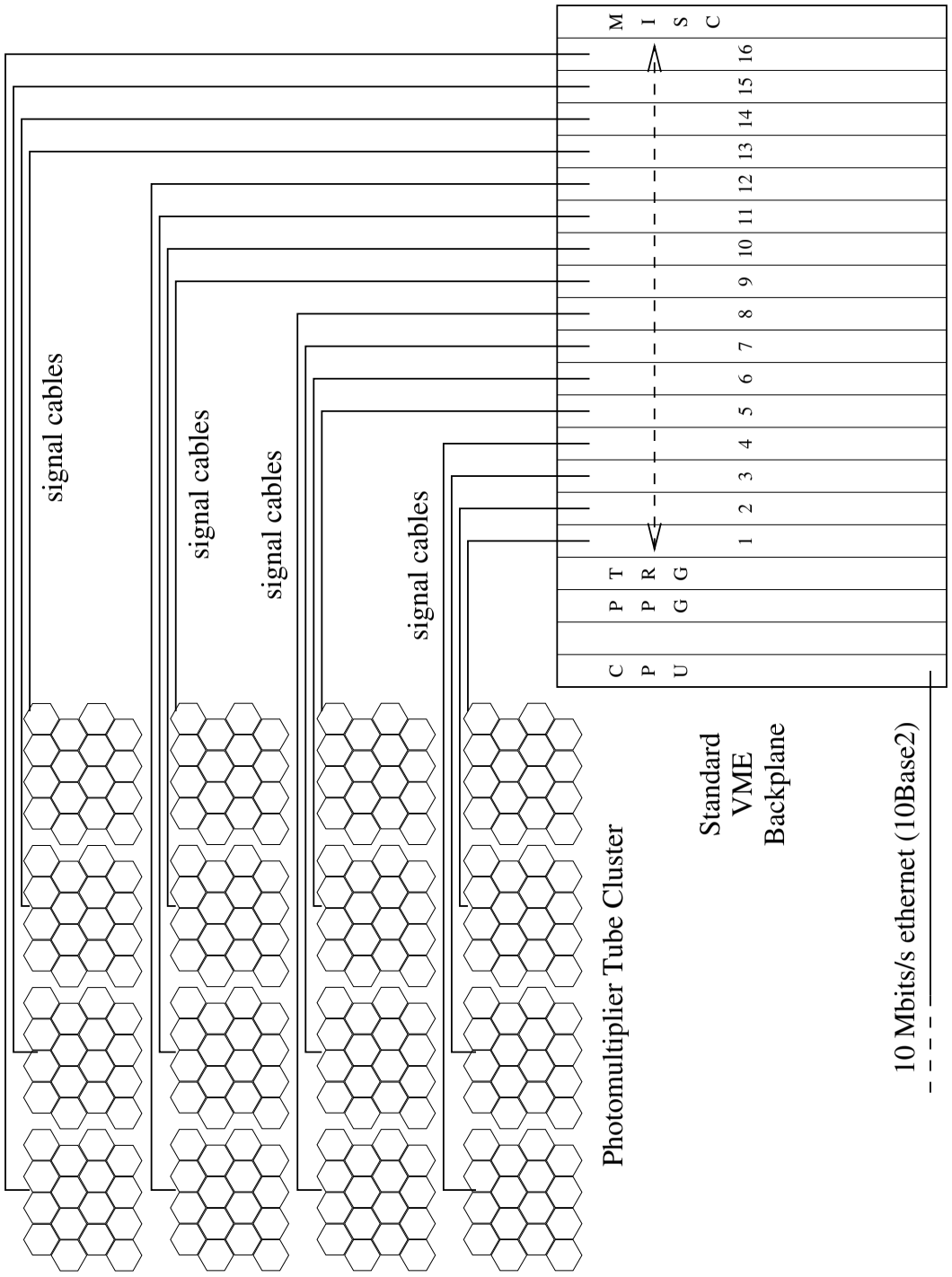

Figure 5.8. HiRes1 electronics rack diagram.

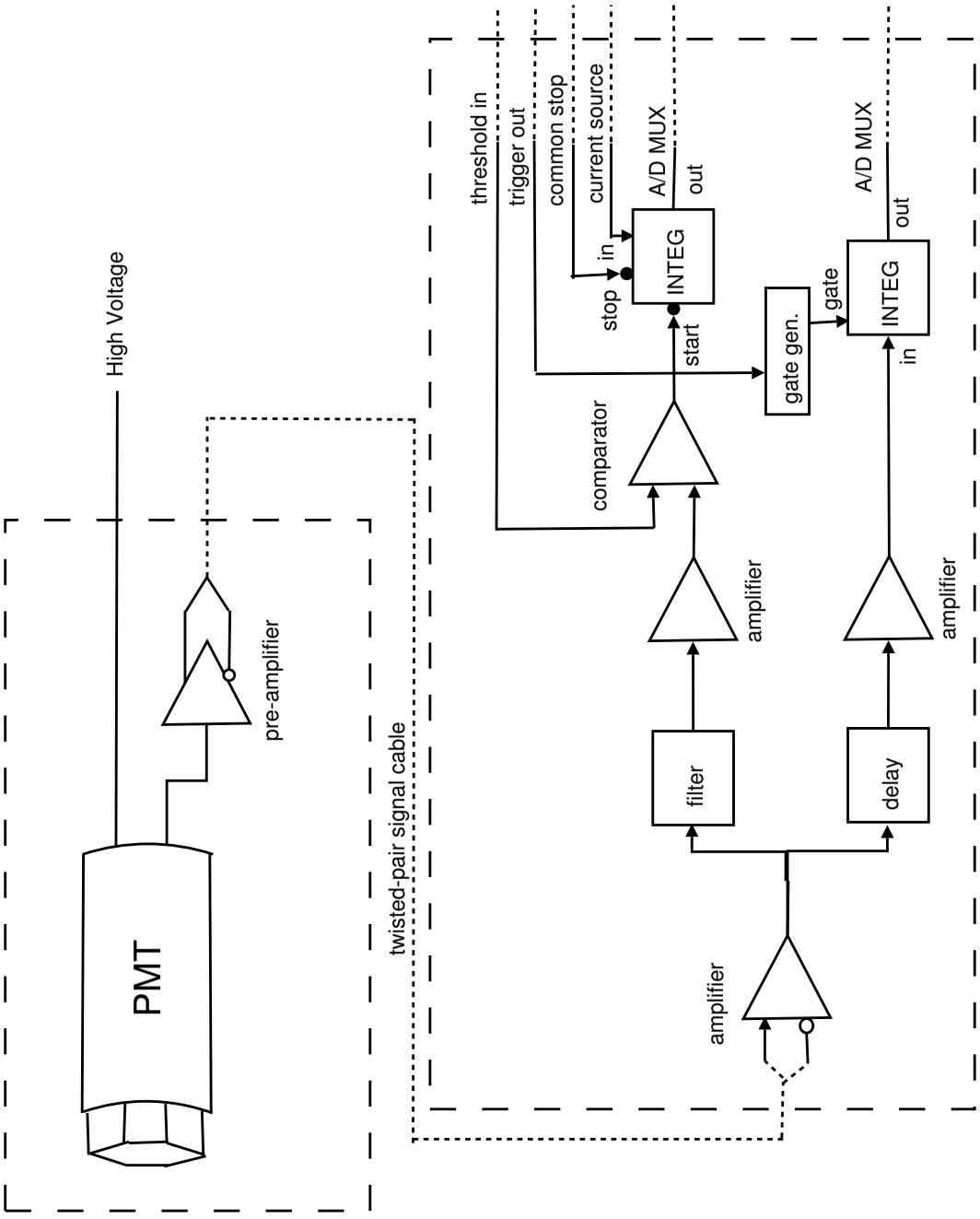

Figure 5.9. HiRes1 electronic channel diagram.

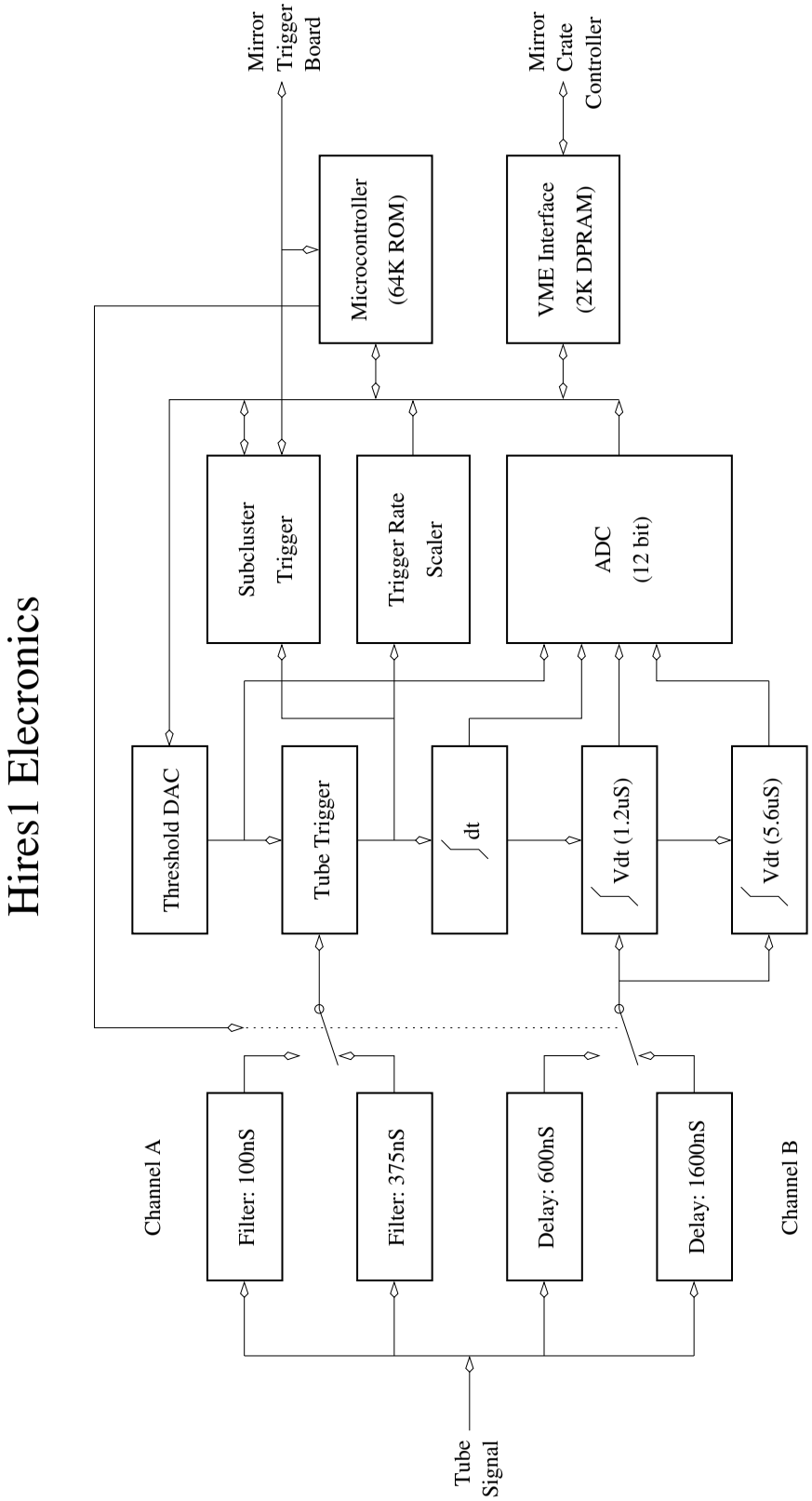

Figure 5.10. Rev. 3 ommatidial board diagram.

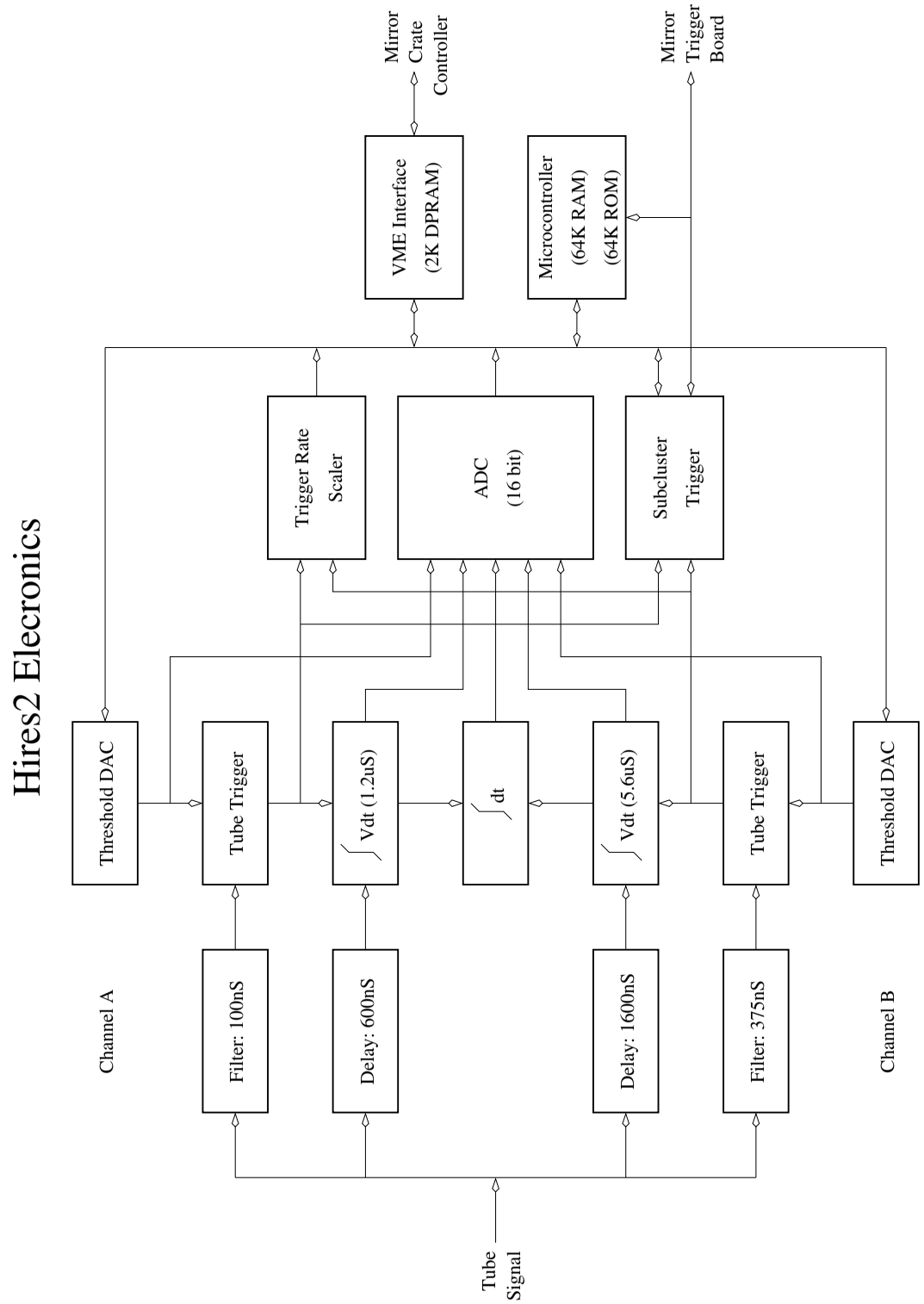

Figure 5.11. Rev. 4 ommatidial board diagram.

ROM lookup table. To form a mirror trigger, three subclusters should be triggered, with two diagonally or orthogonally adjacent. In this case, another $25\mu s$ will be added to the tubes hold-off time. The tubes that are not already triggered will be allowed to do so. This is done to prevent a track cut-off. At the end of the hold-off time, the mirror trigger is sent to the detector Central Timing (CT) to get the absolute time for this trigger. This time is accurate within 25 nsec. As soon as the absolute time is received, the mirror is prohibited from triggering for 8 msec. This is referred to as the mirror dead time. During the mirror dead time, the CPU board will read the timing and charge information from every triggered tube, including the tubes which did not participate in the trigger formation. When the readout is finished, the data packet is sent to the central Data Acquisition System (DAQ) and the mirror is permitted to trigger again.

A typical mirror trigger rate is about 30–120 events/min. The trigger rate is adjusted automatically by changing the tube thresholds. This allows for a compromise between collecting a lot of sky noise and missing some CR events. Too many noise triggers will lead to an increased mirror dead time thus, reducing overall CR trigger rate.

There are other supplemental systems mounted on the HiRes electronics rack. For more details the reader is referred to [64].

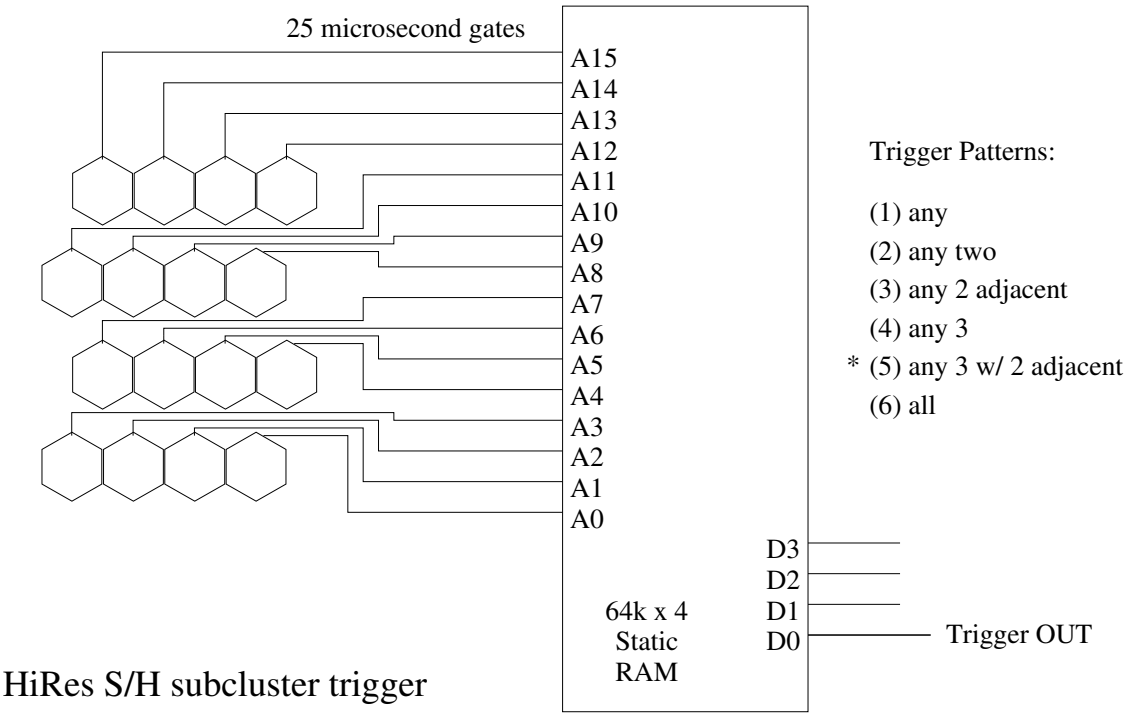

Figure 5.12. HiRes1 subluster level triggering.

5.2.4 Central Timing

The CT rack is located in the HiRes main facility. It provides GPS timing to various HiRes systems as well as hosting some supplemental systems, like the high voltage relay board. Wilkinson [61] gives a good description of the HiRes precision timing systems.

5.2.5 YAG Calibration Laser

A YAG calibration laser is located in the central facility building. It operates at 355 nm wavelength sending the light pulses to the detector mirrors through a network of optical fibers. Three fibers go to each mirror. One goes to the center of each mirror illuminating the the UV detector camera directly. This fiber is referred to as the mirror fiber. Two fibers, usually referred to as the cluster fibers, go to each side of the camera, illuminating the mirror. The light bounces from the mirror back to the camera. This allows us to follow the change in mirror reflectivity.

The HiRes1 detector is described in detail in [64].

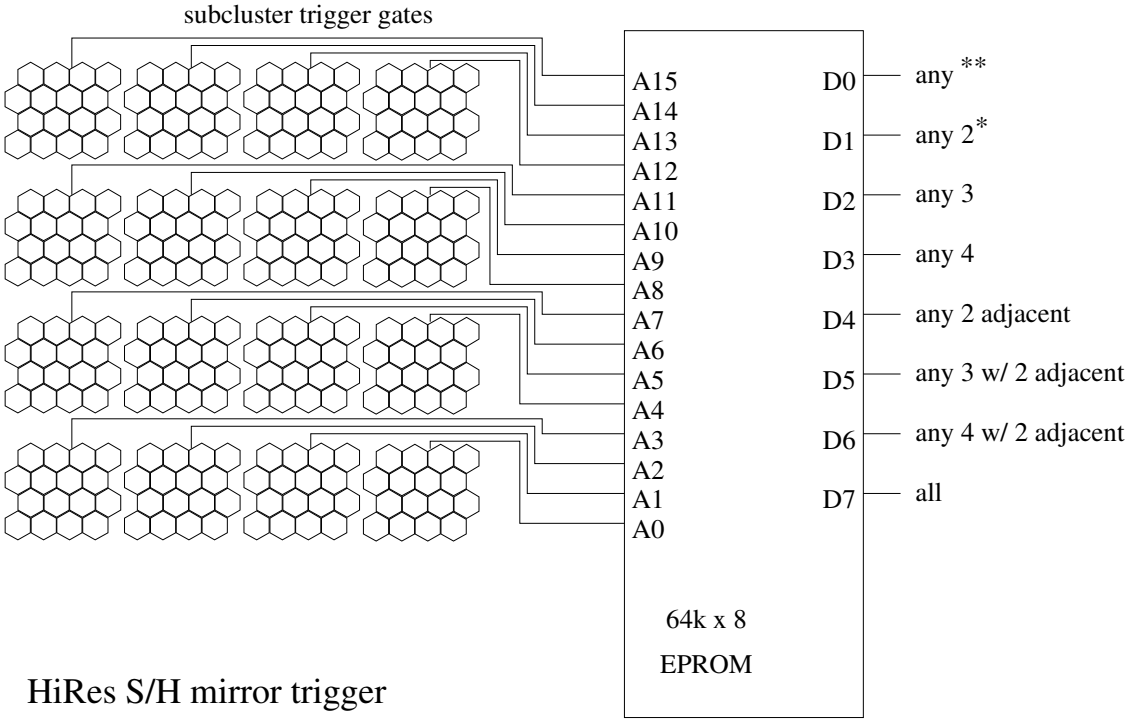

Figure 5.13. HiRes1 mirror level triggering.

5.3 HiRes2

The HiRes2 (FADC) detector is located on a flat top at Camel's Back Hill, 12.6 km south-west of HiRes1. It consist of 42 mirror arranged in one circle, see Figure 5.14. The mirror coverage is in the form of two rings, from 3° to 31° in elevation, and about 340° in azimuth. The mirrors are sheltered in standard buildings with garage doors. They are connected to each other and to the central data acquisition system, located in the central facility, by two fast optical links with network traffic going into opposite directions. See Figure 5.15.

5.3.1 Central Data Acquisition System

The central data acquisition system consists of:

- a central host computer;
- a VLink module;
- a GPSmodule;
- two clock modules.

See Figure 5.15.

The central host computer is a VME PC running the Linux operating system. It provides allocation of 32 MB of memory for direct access by the VLink module. The VLink module is a specially designed VME master. Interrupt service is not required by the PC when VLink accesses its memory with a speed of 20 MB/sec using block transfers. The VLink module is linked to the MLink modules in the mirrors via two optical fibers going around the detector in closed rings. It is also connected to the mirrors via additional equidistant optical fibers through the clock modules. These links provide a 10 MHz synchronization signal as well as limited central control and the program code to each mirror.

5.3.2 Mirror

The HiRes2 Mirror is identical to the one used by HiRes1.

5.3.3 UV Sensitive Camera

The UV sensitive camera is similar to one used for HiRes1. It contains 256 photo-multiplier tubes, arranged in a grid of 16×16. A number of design improvements

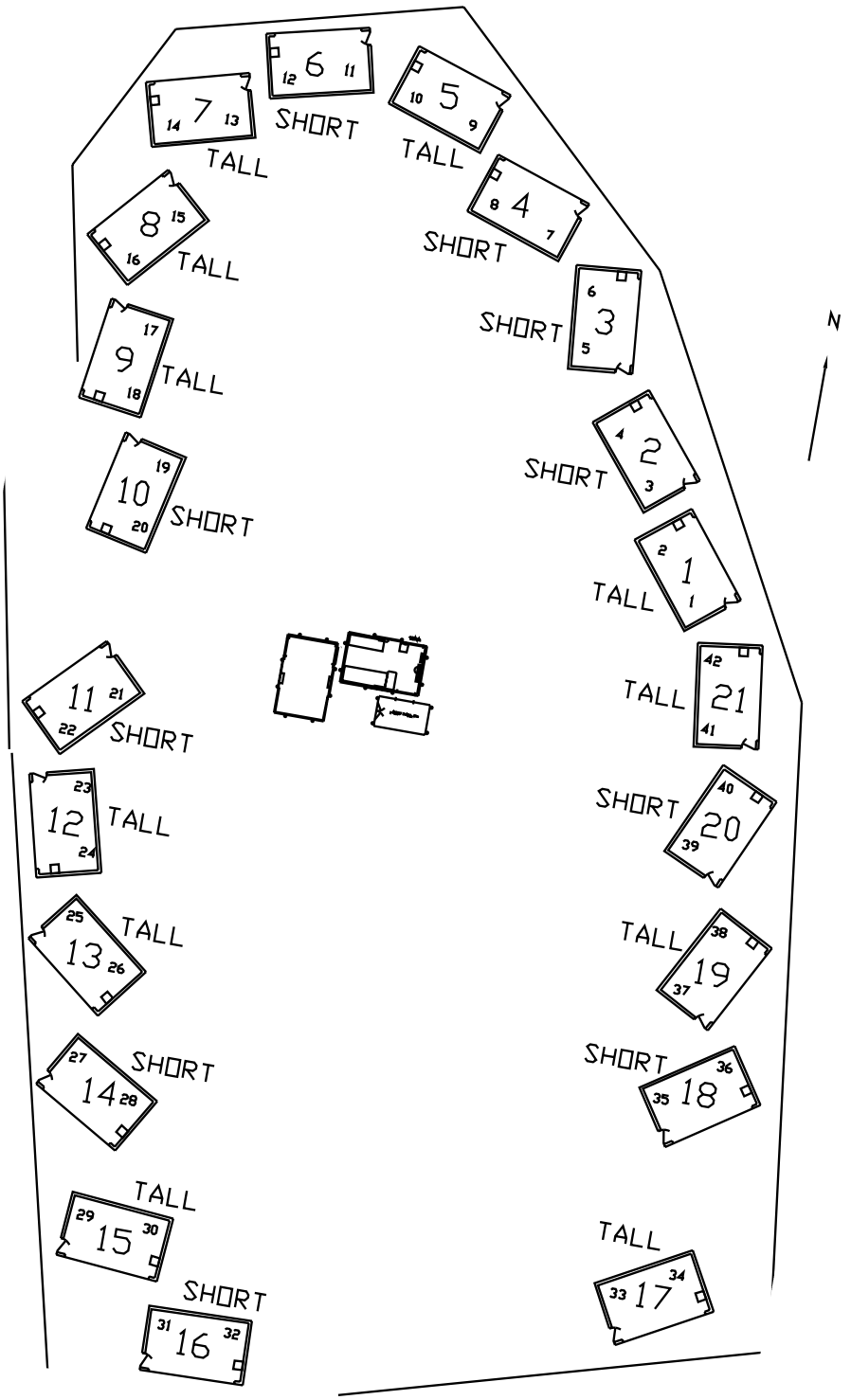

Figure 5.14. FADC detector layout.

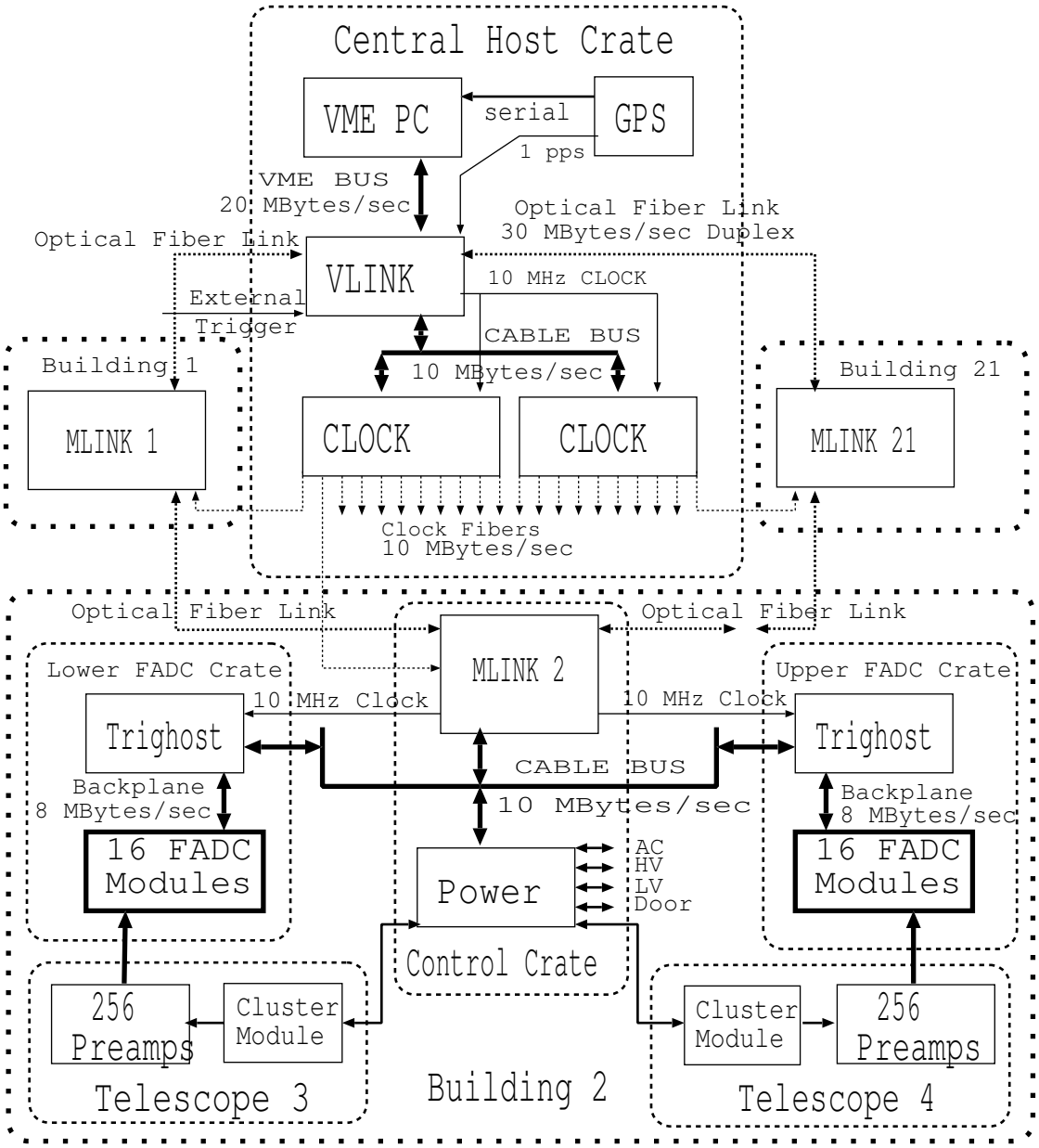

Figure 5.15. FADC detector diagram.

were implemented into FADC UV sensitive camera based on the experience with HiRes prototype and HiRes1 detectors. These improvements eliminate some problems with HiRes1 clusters such as HV arcing and dust accumulation. To reduce the PMTs gain fluctuations, the HiRes2 clusters contain a software controlled heater to maintain a stable temperature within. The temperature uniformity within the cluster is maintained using passive heat exchangers and convection.

The HiRes2 cluster box also contain a programmable test pulser, light level, temperature and voltage monitoring circuits. The programmable test pulser generates pulses of different form and time span. It is used to diagnose hardware problems and for calibration purposes in the same way as the PPG is used in HiRes1.

5.3.3.1 PMT

Only PMTs made by Philips are used in HiRes2 detector (see tubes description in 5.2.2.1). In addition, the tubes for some FADC clusters were specifically selected to have similar gain dependance on the high voltage, described by equation 5.1. The tube selection was done by first calculating the gain difference over the range of applied voltages between all tube pairs using the following formula:

$$D_{i,j} = \frac{\int_{V_{min}}^{V_{max}} [V^{\beta_i} e^{\alpha_i} - V^{\beta_j} e^{\alpha_j}] dV}{\int_{V_{min}}^{V_{max}} V^{\beta_i} e^{\alpha_i} dV}, \tag{5.2}$$

where V_{min} and V_{max} are the minimum and the maximum applied high voltage. Parameters α and β are determined during the PMT scanning in the lab, (see Section 5.4.1.1 below). This tube selection makes the cluster gain drift more uniform for the entire cluster. Gains at 1000 V for four sets of 270 tubes selected for the clusters are shown in Figure 5.16 (see details in my technical note on PMT selection [65]).

The tube gains were adjusted to the same value by altering a resistor in the tube HV chain. This provides better gain uniformity throughout the cluster and was done before assembling the tubes into the cluster boxes.

5.3.3.2 UV Filter

The HiRes2 UV filter serves the same purpose and and is identical to the HiRes1 filter. See 5.2.2.2 for a description.

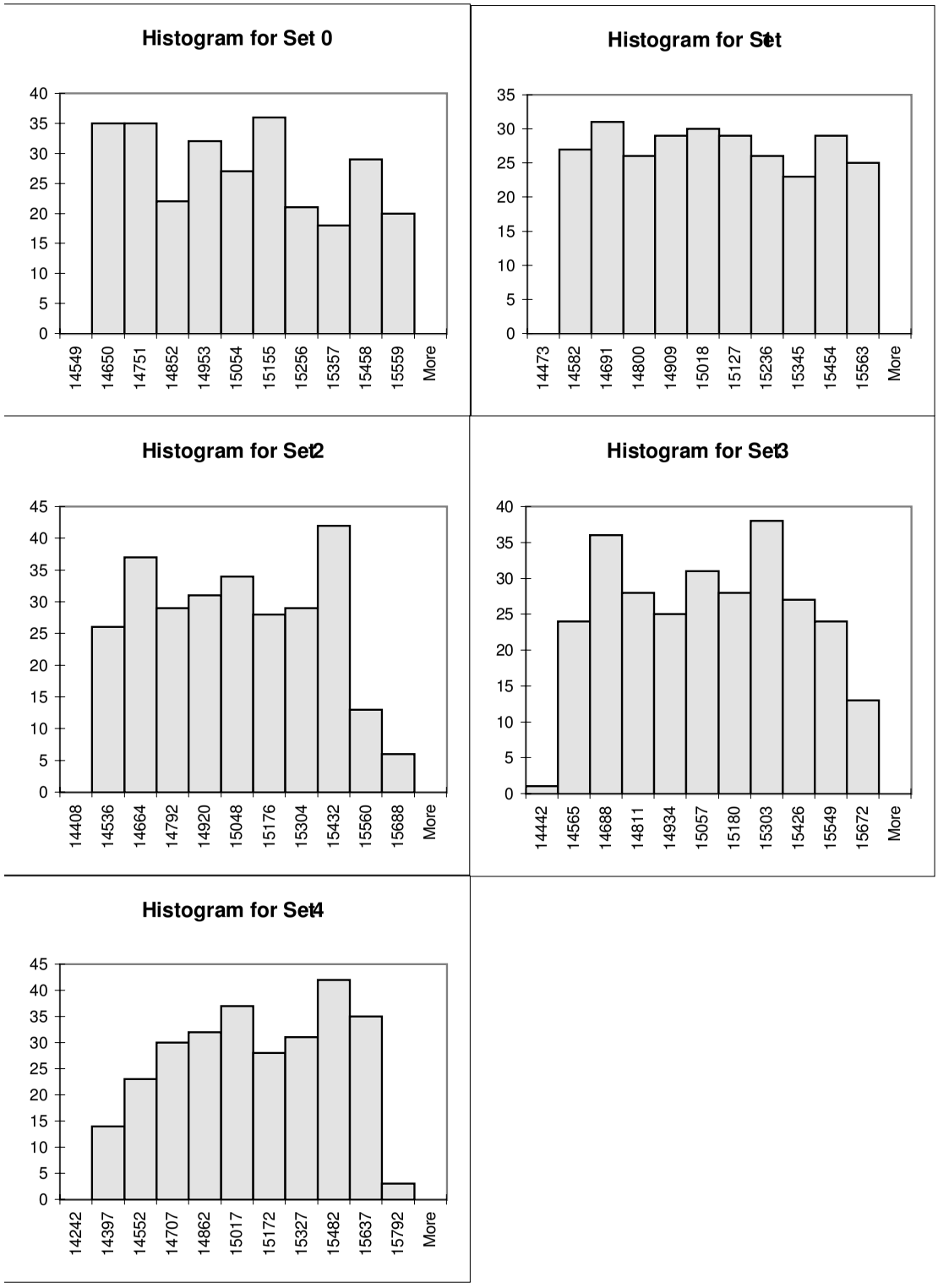

Figure 5.16. Tube gain distribution for selected PMT sets.

5.3.4 Electronics Rack

There are 21 electronics racks for this detector. Each rack holds electronics for two mirrors. The rack hosts:

- a low-power control crate;
- two FADC crates;
- a power supply.

The control crate contains the following modules:

- an MLink module, which is responsible for mirror communications via optical fiber link;
- a power module, which controls power supplies;
- a heat exchanger;
- heaters;
- programmable test pulsers;
- the door controls;
- temperature, light level, voltages and door status monitors.

Each FADC crate contain:

- a Trighost module;
- 16 identical FADC modules.

The Trighost module provides trigger processing as well as control and communications. The FADC modules split responsibility for the signal processing for each mirror. One board processes the signal for a column of 16 PMTs. The initial signal amplification and pulse shaping is similar to HiRes1 and is done by the preamplifier, mounted on a circuit board together with the tube. The preamplifier output is transmitted to the FADC board where it is passed through an RC filter and another amplification stage. The gain and the offset of each tube signal are controlled individually at this stage. Next, the signal is digitized every 100 ns by an 8 bit analog to digital converter. A four-pole

120 nS digital filter ensures that 1 FADC count of the signal measurement is equal to 1 photoelectron. An 8K ring buffer delays the signal by 819 μs to give enough time for the first level triggering. This trigger can be formed by a local trigger board, a nearby mirror trigger board or by the central host.

Two analog sums of 16 tubes forming a vertical column or a horizontal row are also analyzed. Each sum is digitized twice: with lower gain and with longer filter time. The digitization with the lower gain improves the dynamic range while the digitization with longer filter time serves the purpose of a comparison with the thresholds. These threshold are software adjustable. The Trighost module analyzes comparison signals to form a first level trigger, also referred as a "pipelined" trigger. The first level trigger is formed if there are two or more different three-fold coincidences found, which are followed by a 5 μs time interval without a coincidence, or the coincidence stays on 102.4 μs. A three-fold consistence means a group of three or more adjacent or next-to-adjacent rows or columns.

If a trigger is formed, it is stored in a trigger queue and also sent to the neighboring mirrors. The trigger module also commands the data transfer from the ring buffer to the secondary data buffer.

Once the first level trigger is formed, the data are transferred from the ring buffer to a 32K secondary memory, the data buffer, in preparation for possible future processing. The time window for data storage is centered on the trigger time and is 3 times + 12.6 μs wider than the first level trigger lasted, but can not exceed 200 μs. The capacity of the data buffer is 3.2 ms, which corresponds to about 100 typical CR events. In theory, it is enough to completely eliminate dead time.

With 819 μs delay, the trigger module has enough time to analyze the all the triggers. Local and distant triggers are combined in time intervals and stored to be processed by the DSP on the FADC board to form a confirming trigger.

The FADC board DPS's first scan the data stored due to the first level trigger. The data is first scanned with a single pole digital filer to check the presence of nearby pulses. The time scale of the filter is the same as for the trigger hardware filter, but the threshold is two times lower. Individual tubes within the hardware trigger time window are scanned. The lower threshold is needed to identify if the signal is split between two tubes. Once a pulse is identified, the corresponding tube ID is sent to the trigger board, together with the pulse time and value.

Identification of at least three pulses will force an addition pattern recognition search. A confirming trigger is formed if a cluster of three neighboring tubes has triggered. The definition of neighboring in this case is six immediate neighbor tubes plus six next neighbor tubes which fill the cracks in between the first six.

Most of the random noise and other uninteresting events can be filtered out at this level. All the trigger recipients are informed about the confirming trigger result.

The data, corresponding to the confirmed trigger, are read from the data buffer and stored on the permanent computer memory in the network packet format for off line processing.

5.3.5 YAG Calibration Laser

The HiRes2 YAG calibration laser is very similar to the HiRes1 one, (see 5.2.5). The light is delivered to the mirrors the same way, via optical fibers. In addition, the HiRes2 YAG laser has a filter wheel, which allows the light output to change by automatically placing filters of different transparency in the laser beam. Girard at al. give a detailed description of the FADC YAG calibration laser in [66].

For more details about FADC system the reader is referred to [67].

5.4 Calibration

HiRes is an air fluorescence detector. Air shower parameters, including energy, are determined by measuring the amount of fluorescence light produced by the shower. In order to measure those parameters correctly, two major components must be well understood:

- the detector response to fluorescence light;
- amount of light scattered in the atmosphere on its way from the shower to the detector.

Both the detector calibration and the atmospheric calibration are briefly described below.

5.4.1 Detector Calibration

5.4.1.1 PMT Calibration

It is important to know the total photocathode area, the tube sensitivity across the surface and the overall tube gain for each PMT. A special testing facility has been built

at the University of Utah to test photomultiplier tubes prior to installing them into the cluster. The facility consists of a 325 nm HeCd laser, focusing elements and a moving x-y table. All components are mounted on an optical table and placed into a dark box. The facility is controlled by a computer. Each tube is scanned by a laser beam falling normally on the photocathode. The size of the beam spot is less than 1 mm. The tube response is measured at 418 points across the tube surface area. The tube gain as a function of the applied voltage is measured at seven points on the tube surface. The tube rejection criteria are:

- too small a photocathode area;
- nonuniform tube response across the surface;
- low gain.

The tubes with similar gain dependance on applied voltage are put into the same cluster. This helps to reduce the PMT gain variations with high voltage change within one cluster. PMTs made by EMI and Philips have a similar response function to that shown in Figures 5.17, 5.18, 5.19 and 5.20. This function is used in the data processing and for MC simulations. The response function fluctuations are small for the same brand of tubes passing the selection criteria. This allows for one, average response function to represent the entire brand in data processing and MC simulations. Ref. [68] gives details about the PMT scanning setup, procedure and results.

5.4.1.2 Mirror Reflectivity

In order to measure the amount of light coming from the air shower, the mirror reflectivity must be known with adequate accuracy. The reflectivity of HiRes mirrors was measured several times during the life of the experiment and found to vary only slightly from mirror to mirror and from measurement to measurement. The most recent absolute reflectivity measurement was done using a specially constructed reflectometer [69]. 24 points across the mirror were measured, as illustrated in Figure 5.21. Based on these data, the reflectivity behavior was modeled as a function of wavelength [69, 70]. In this model, the HiRes1 mirror reflectivity R is approximated by:

$$R = -348.4 + 2.796\lambda - 6.232 \times 10^{-3}\lambda^2 + 4.676 \times 10^{-6}\lambda^3. \tag{5.3}$$

The HiRes2 mirror reflectivity is approximated by:

$$R = -268.6 + 2.523\lambda - 6.131 \times 10^{-3}\lambda^2 + 4.933 \times 10^{-6}\lambda^3. \tag{5.4}$$

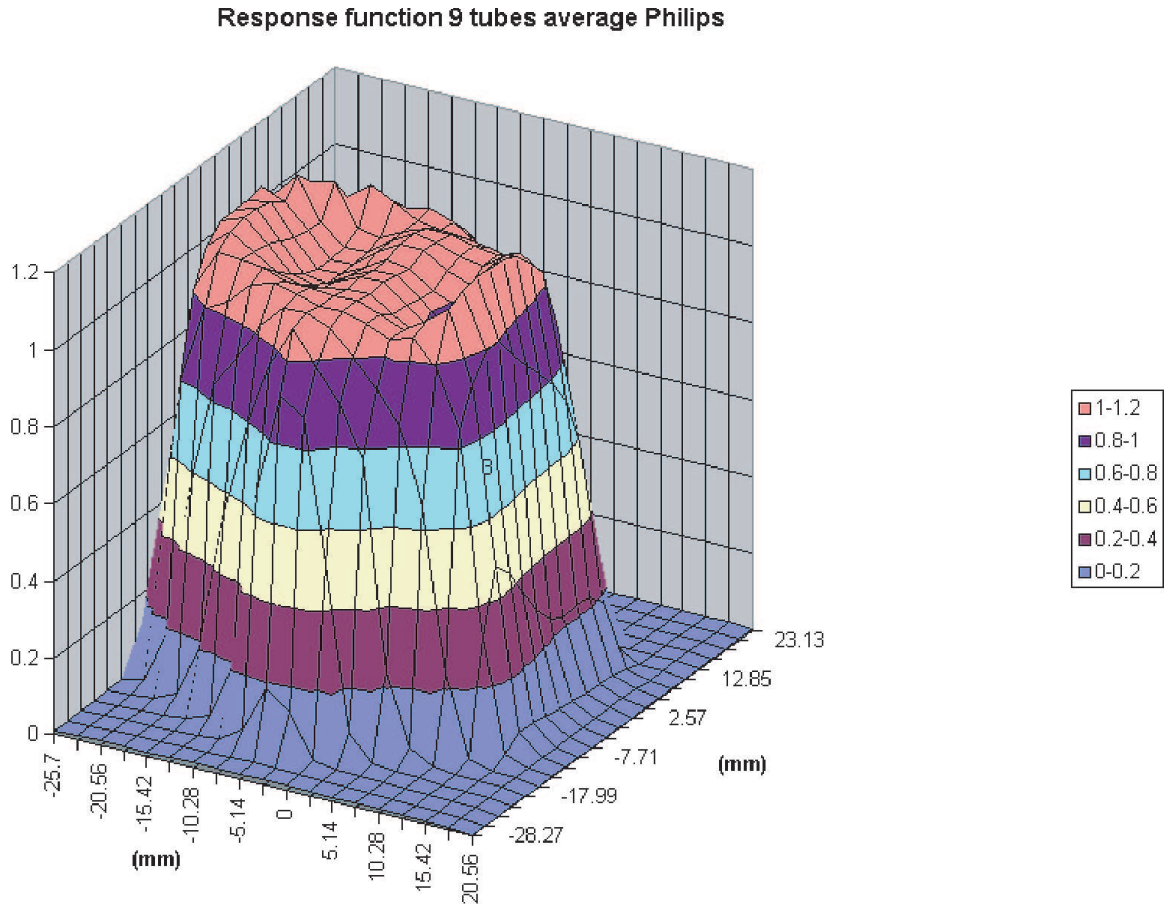

Figure 5.17. Philips PMT response function.

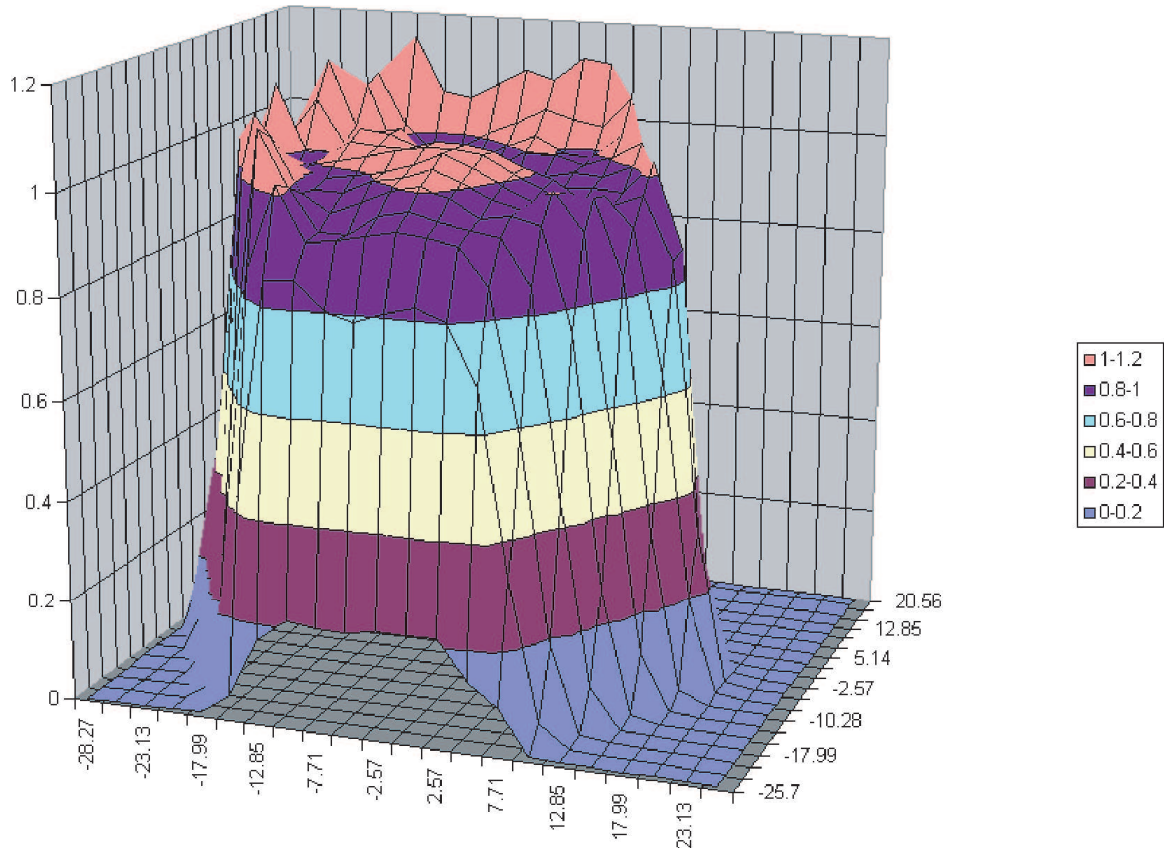

Figure 5.18. EMI PMT response function.

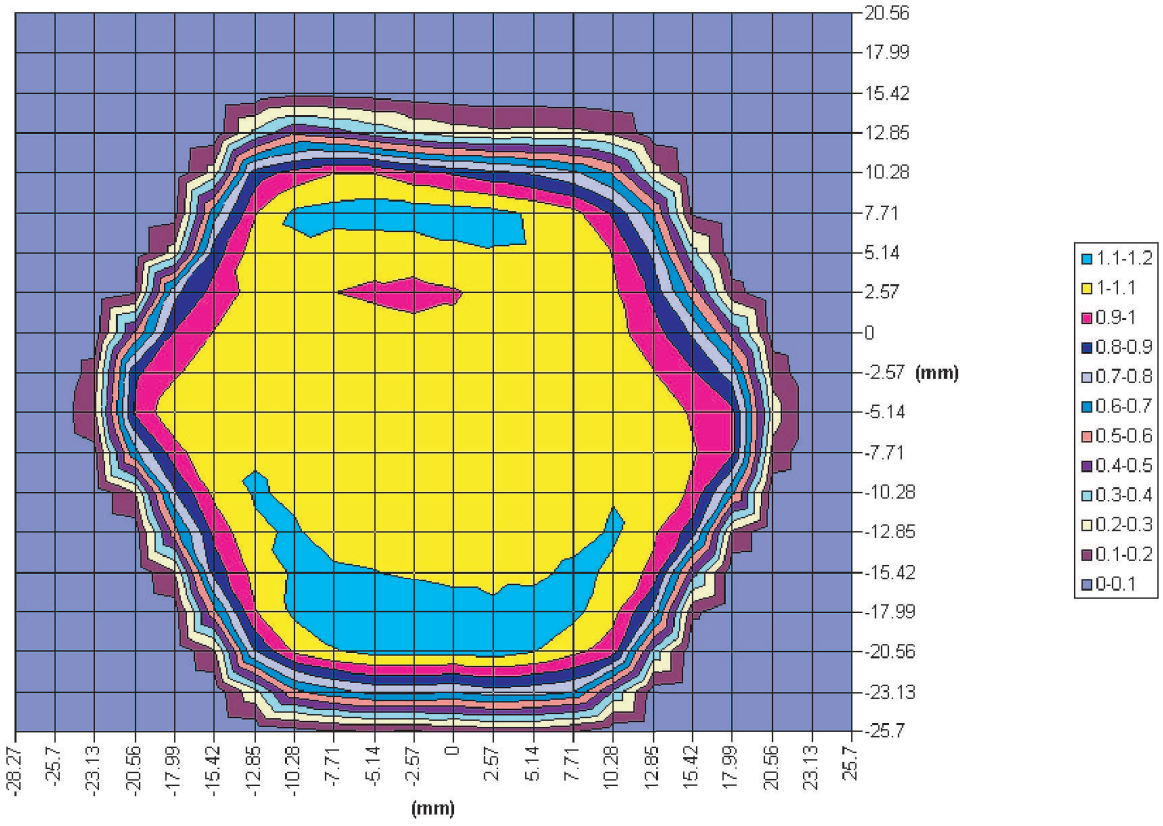

Figure 5.19. Philips PMT response function. Surface projection.

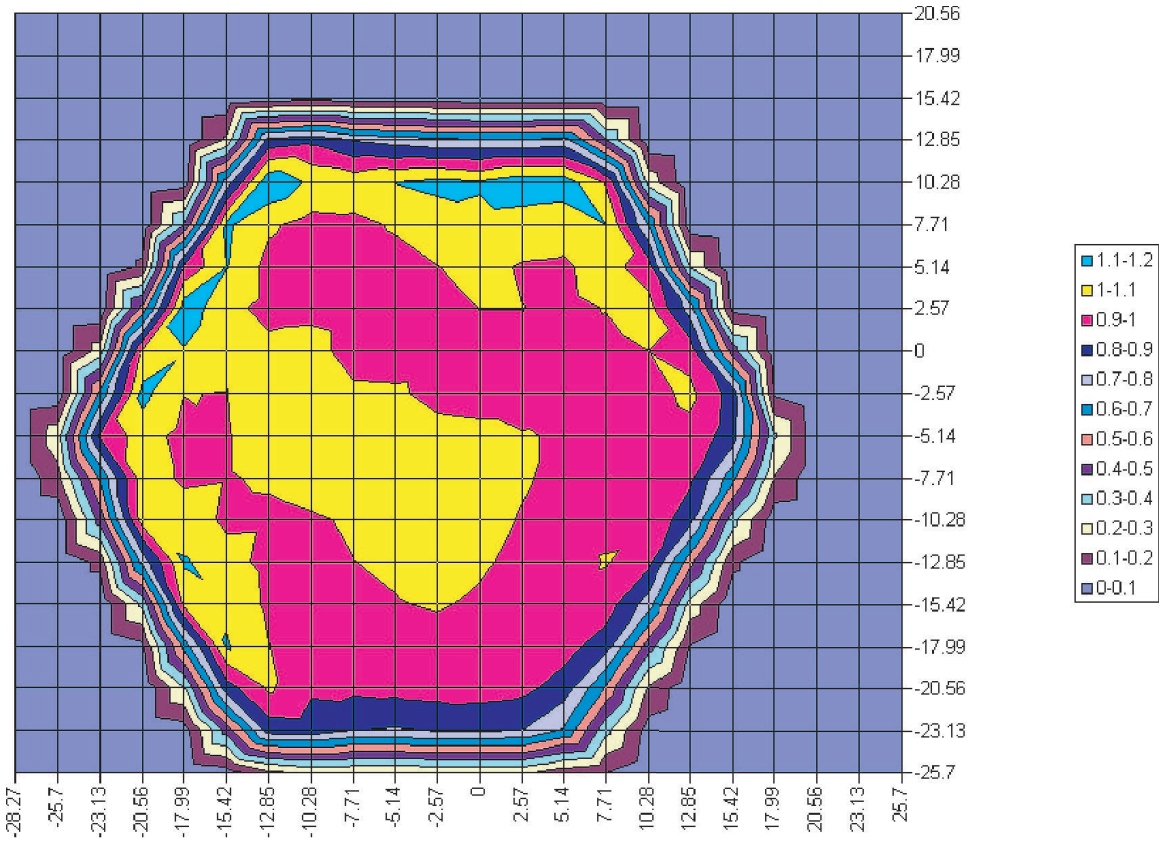

Figure 5.20. EMI PMT response function. Surface projection.

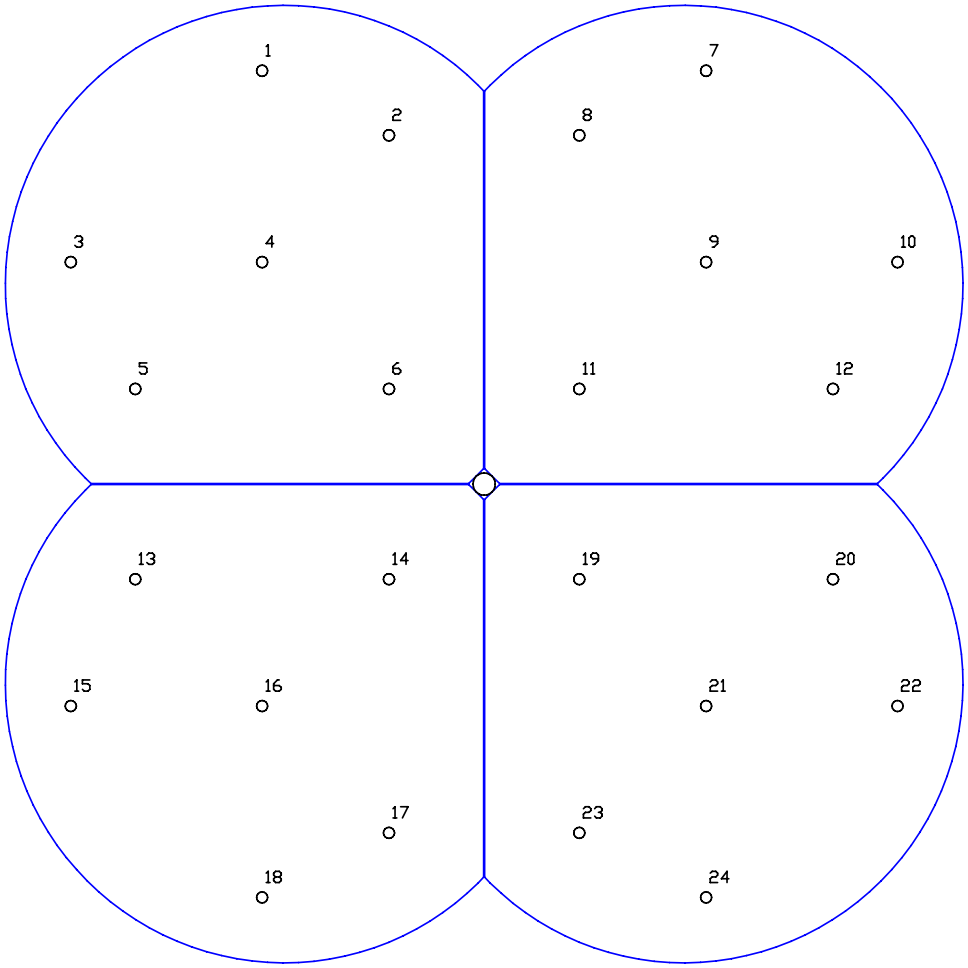

Figure 5.21. Mirror reflectivity measurement points.

Both model responses are plotted in Figure 5.22. The lower curve corresponds to 5.3 and the upper one corresponds to 5.4. Figure 5.23 shows the measured reflectivity for all 20 HiRes1 mirrors approximated by 5.3. The same curves for 42 HiRes2 mirrors and using 5.4 are shown in Figure 5.24.

In order to get the absolute reflectivity for each mirror, one has to multiply 5.3 or 5.4 by the relative mirror reflectivity R_m provided in Table 5.1.

The HiRes2 mirrors were anodized several years after the HiRes1 and at different facilities. These factors explain the observed difference in the mirror reflectivity between the two sites.

To measure a relative change in mirror reflectivity, a YAG laser is used nightly. Pulses of UV light illuminate each mirror from the cluster and the light reflected back to the camera, provides a relative mirror reflectivity measurement. These nightly measurements

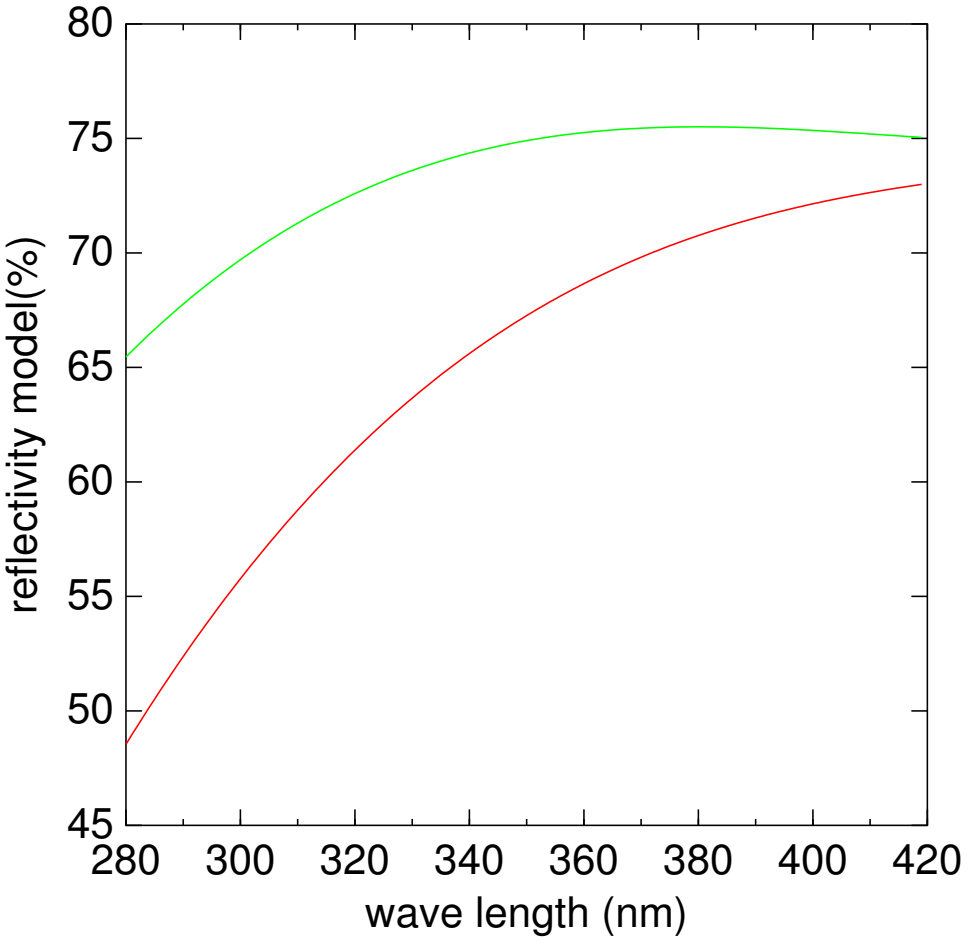

Figure 5.22. Mirror reflectivity models.

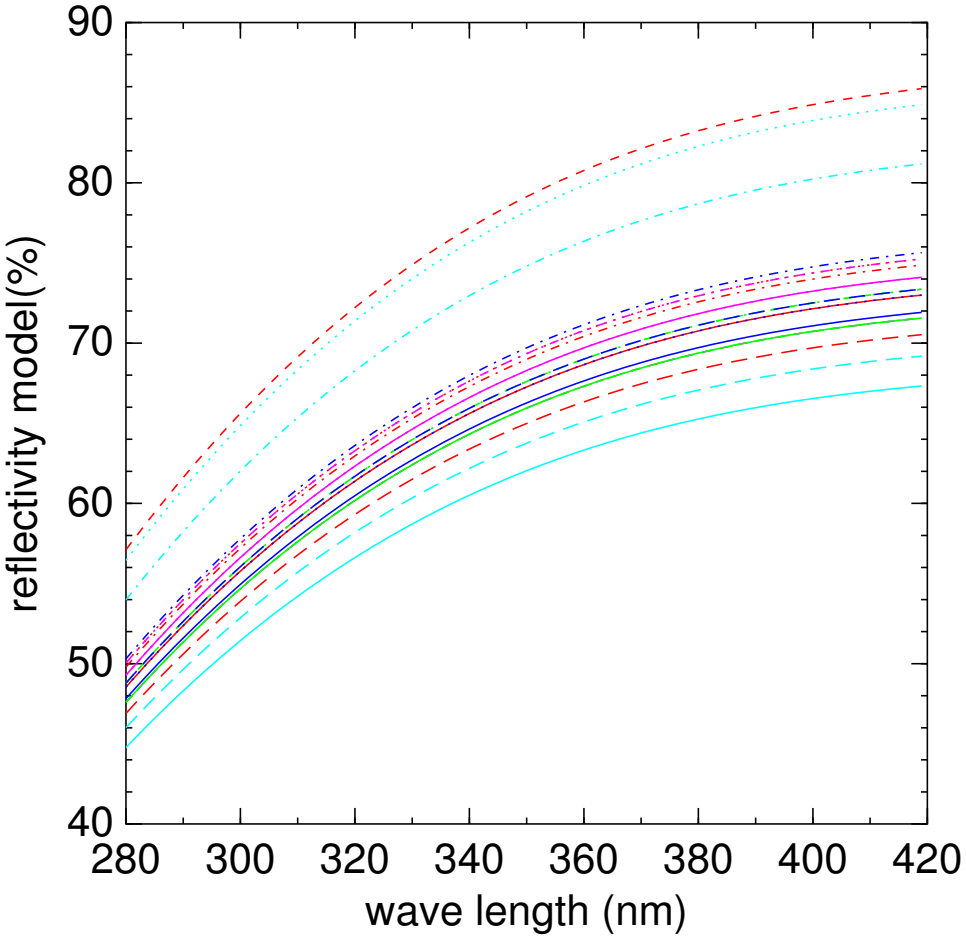

Figure 5.23. HiRes1 mirror reflectivity.

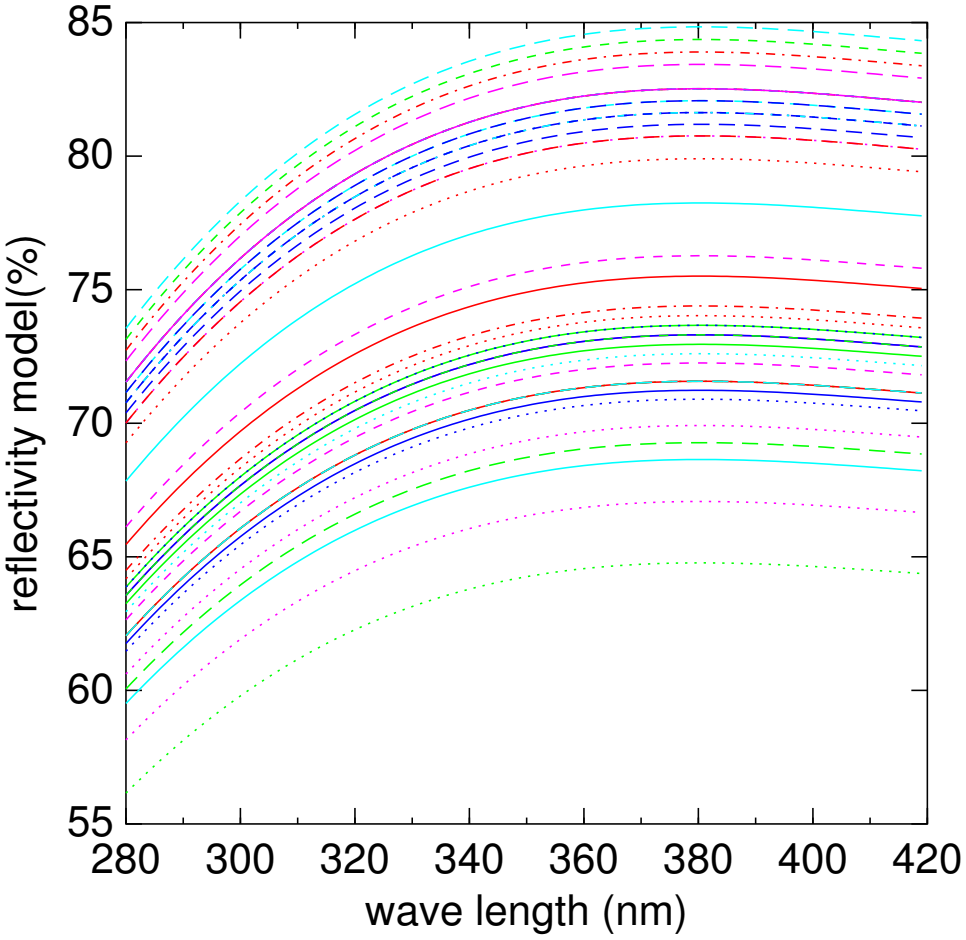

Figure 5.24. HiRes2 mirror reflectivity.

Table 5.1. Relative mirror reflectivities.

HiRes1		HiRes2			
mir	R_m	mir	R_m	mir	R_m
1	0.985	1	0.943	22	1.087
2	0.922	2	0.909	23	0.917
3	1.005	3	0.858	24	1.105
4	1.015	4	0.888	25	0.948
5	1.026	5	1.111	26	0.971
6	1.036	6	1.081	27	1.036
7	1.112	7	1.081	28	1.093
8	1.005	8	1.117	29	0.926
9	0.980	9	1.010	30	0.985
10	0.966	10	0.948	31	1.093
11	1.005	11	1.075	32	1.093
12	0.948	12	1.124	33	0.971
13	0.980	13	0.966	34	0.958
14	1.015	14	0.971	35	1.070
15	1.032	15	0.980	36	1.087
16	1.000	16	0.939	37	0.948
19	1.163	17	0.962	38	0.976
20	0.980	18	0.948	39	1.093
21	1.031	19	1.070	40	1.058
22	1.176	20	1.093	41	0.976
		21	1.081	42	0.995

help to monitor the mirror reflectivity change. The accumulation of dust affects mirror reflectivity. Using the YAG laser calibration, it was found that the reflectivity increases right after mirror washing and than slowly falls until it stabilizes at 80-85%.

Until a recent study [69, 70] that accurately measured the reflectivity for each mirror, an 80% reflectivity was used for all the mirrors. This number was an average of the previous measurements and was less accurate.

5.4.1.3 UV Filter Transmission

The filter transmission coefficient as a function of wavelength is shown in Figure 5.25. Small variations across the filter surface as well as between different filters are ignored and 0.81 is used as the transmission coefficient for all HiRes filters during data processing and MC simulations.

5.4.1.4 YAG Laser Calibration

The HiRes YAG calibration laser is used at the beginning and at the end of each night the detector collects the data measuring the relative change in the detector response. Each calibration session starts with 500 YAG laser shots to the mirror fiber followed by 500 shots to the cluster fibers. After the mirror doors are opened, the procedure is repeated. This allows us to follow the PMTs gain change, mirror reflectivity change and to estimate

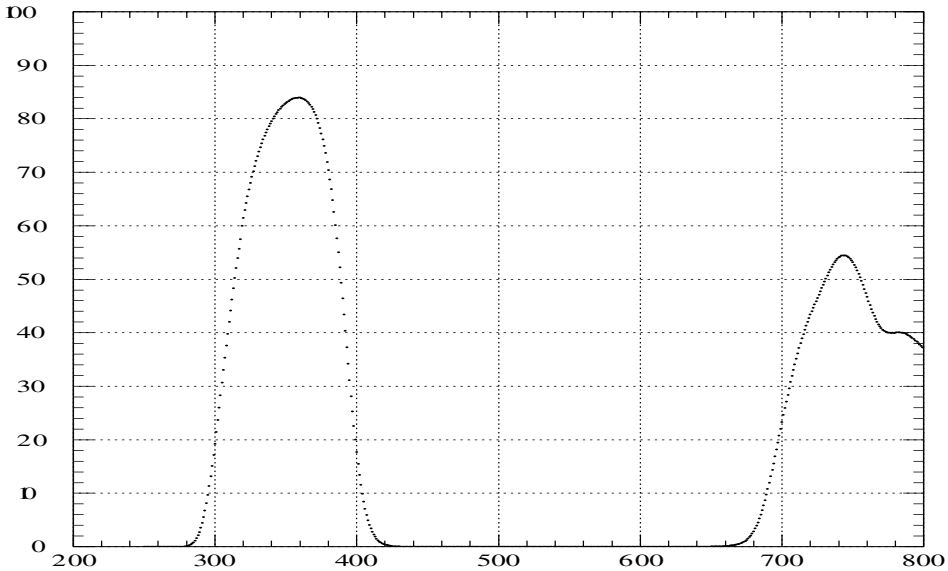

Figure 5.25. HiRes UV filter transmission (%) vs wavelength (nm).

the sky noise.

PMT gain is measured as number of photo-electrons per QDC count. Figure 5.26 shows the average PMT gain as a function of time for one of the HiRes1 mirrors. The PMT gain fluctuation due to all possible causes are about 10%.

The absence of a tube response to YAG light would indicate an inoperative PMT.

5.4.1.5 RXF Calibration

The Roving Xenon Flasher (RXF) provides an absolute calibration of the system. It is a standard candle delivering 12,000 photons/PMT. It has been calibrated using a Hybrid Photo Diode (HPD) (see section 5.4.1.6). During the RXF calibration, the flasher is placed in the center of each mirror illuminating the cluster. It is possible to check the PMT linearity by placing neutral density filters with known optical transmission in front of the RXF. Poisson statistics can also be employed for the same purpose. Indeed, the following equation will hold:

$$N_{pe} = (1 + \alpha) \times \frac{\mu^2_{QDC}}{\sigma^2_{QDC}}, \tag{5.5}$$

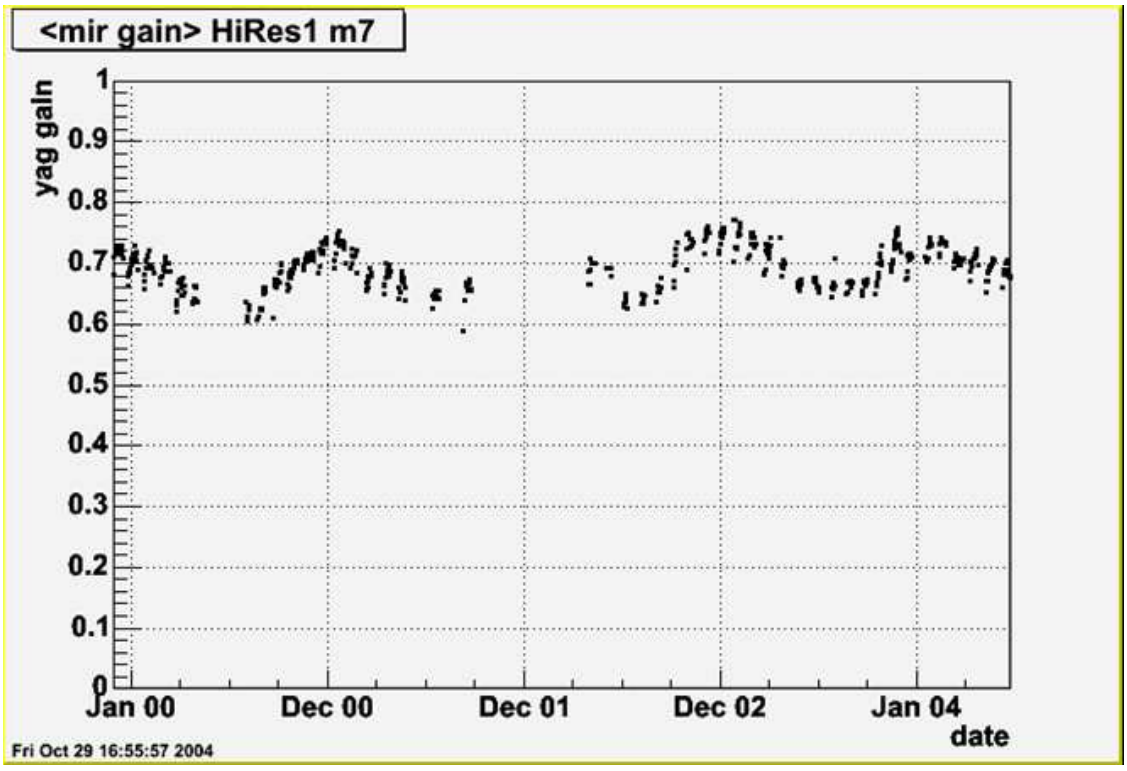

Figure 5.26. PMT gain variations.

where N_{pe} is the number of photo-electrons, μ^2_{QDC} is the mean and $\sigma^2 QDC$ is the standard deviation of the signal. Once statistics is accumulated, eq. 5.5 provides an accurate measurement of the PMT gain.

The gain measurement utilizing the filter method is shown in Figure 5.27. A single YAG measurement is also shown on the same plot.

RXF calibration takes significant amount of time, and thus, can be done only on a periodic basis between the runs.

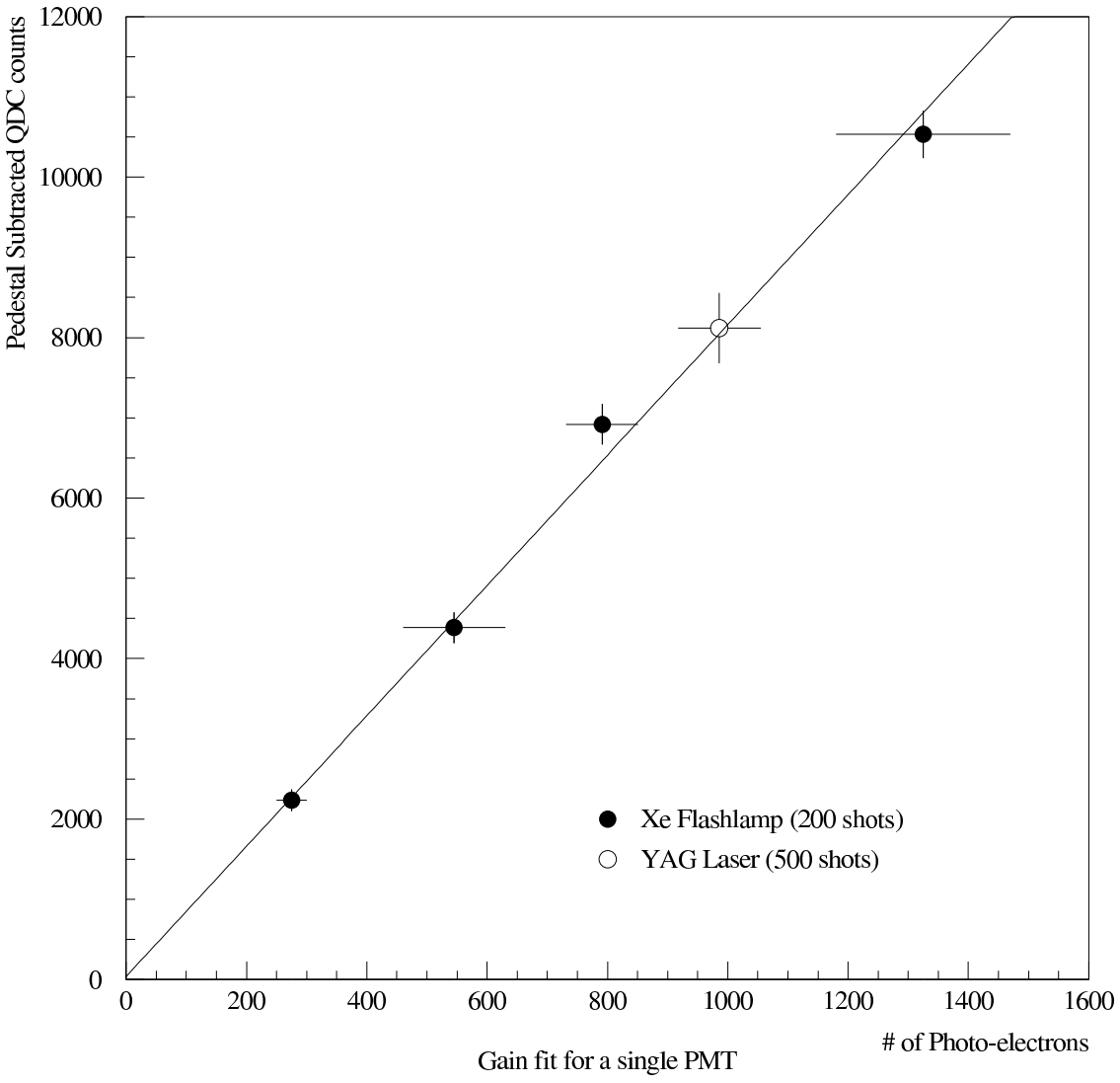

Figure 5.27. PMT gain linearity.

5.4.1.6 Hybrid Photo Diode Calibration.

A hybrid photo diode is a semiconductor device which precisely measures the amount of light falling on its sensitive area. It is calibrated by the National Institute for Standards and Testing. Periodic measurements of the amount of light from the mirror optical fibers are done. These measurements confirm the stability of the RXF.

5.4.2 Atmospheric Calibration

The fluorescence observation technique uses the atmosphere as the detector calorimeter. Unlike manmade calorimeters used in the accelerator experiments, atmospheric parameters can change rather quickly. Ideally, the atmospheric conditions should be known for each CR event to allow for an accurate reconstruction of the CR shower. The "shoot the shower" rapidly steered laser beam system [71] is an example of an atmospheric monitoring system which provides almost instantaneous information about the atmosphere in the vicinity of a particular CR shower. As such a system was implemented only recently, the data used in this dissertation were processed using the information provided by older atmospheric monitoring stations and weather observations.

5.4.2.1 Steerable Laser Systems

The HiRes steerable laser system consists of one laser at each detector site. Both lasers are installed in separate buildings and allow the beam to be steered to any desired direction making such a system perfectly suited for local atmosphere monitoring. The lasers operate at 355 nm, and thus, are visible to the HiRes detectors. The energy of the HiRes1 laser is 50 mJ and the HiRes2 laser – 7 mJ. The lasers sweep through the entire sky once per hour. The information about the beam direction and energy is saved in a log file for each laser shot, allowing for easy reconstruction of laser events during data processing. The laser clocks are synchronized by means of the Global Positioning System (GPS).

In case of an interesting CR event, the lasers switch to the "shoot the shower" mode. Suspending their regular sky sweep mode, the lasers turn to the direction of the shower and make several shots, providing valuable information about the atmospheric conditions near the CR shower vicinity at the time of the event.

A detailed description of the HiRes steerable laser system is provided by Roberts [72] and Wiencke [73].

5.4.2.2 Fixed Laser System

A third fixed HiRes laser system is located in Terra, 22 km from HiRes1 and 34 km from HiRes2. This laser operates at 355 nm wavelength. It fires shots vertically with the energy adjustable within 2–6 mJ range. Its primary purpose is to study atmospheric transmission further away than the steerable laser systems. The Terra laser location makes it suitable for testing the detector aperture at the highest energies [74].

5.4.2.3 Vertical Xenon Flashers

An array of stationary flashers is located in the desert between both detectors. There are 10 flashers located on two "spokes" from the HiRes2 detector (see Figure 5.28). These flashers utilize xenon bulbs with the light output in broadband UV. Xenon bulb light output has proven to be stable within 2% during the bulb lifetime. The beam direction of all flashers is fixed at the vertical position. The flashers independently fire light shots, which are seen by both detectors. The flasher tracks can be seen by operators at HiRes in real time and provide valuable qualitative information about the weather condition and confirm that the detector is operating properly. Figure 5.29 shows how the flasher track looks on the HiRes monitor when the atmosphere is clear. Figure 5.30 shows cloudy running conditions. A thick flasher track on the HiRes display would indicate a hazy atmosphere. Flashers can also serve as a reference to synchronize both detectors in case of GPS timing problems (see the detailed description of the HiRes flashers in [75]).

5.4.2.4 Weather Monitoring Stations

Two off the shelf weather monitoring stations are installed near the HiRes1 detector. One is at the central trailer and the other one is at the steerable laser system building. They provide information about the temperature, dew point, humidity, wind and pressure for the detector operator. This information is recorded every hour into the log file and also used to make a decision if the data collection is possible with current weather conditions. A US government weather station conveniently located near HiRes2 is also utilized.

5.4.2.5 The Weather Code

The skies are monitored by the detector operator on an hourly basis. Information about the clouds is recorded into the log file as a seven digit weather code. The first 4 digits indicate a horizon (less than 20 degrees in elevation) cloud coverage in N,E,S,and W directions correspondingly. a 0 indicates no cloud, and a 1 indicates some cloud. The

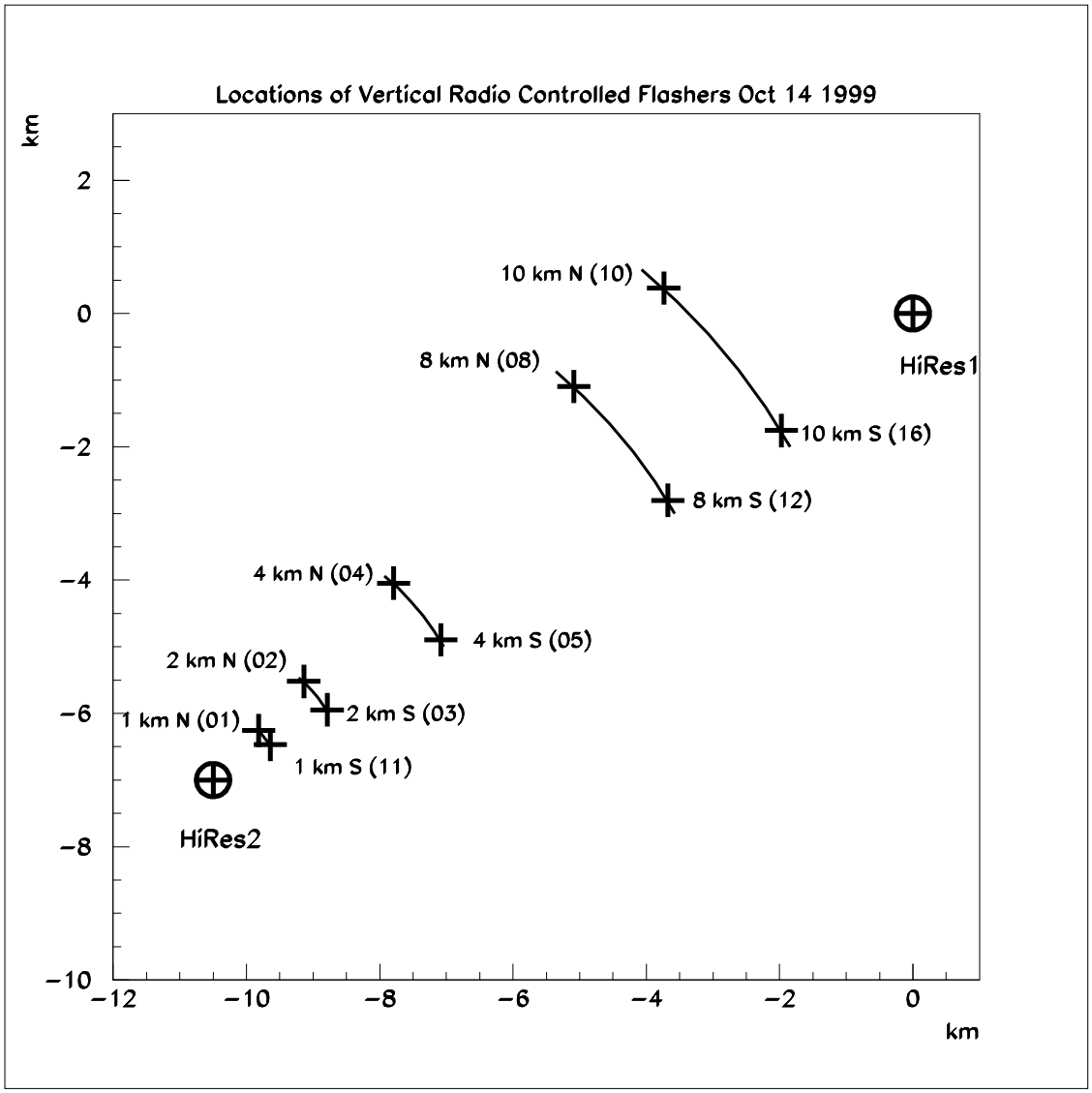

Figure 5.28. Xenon flasher array.

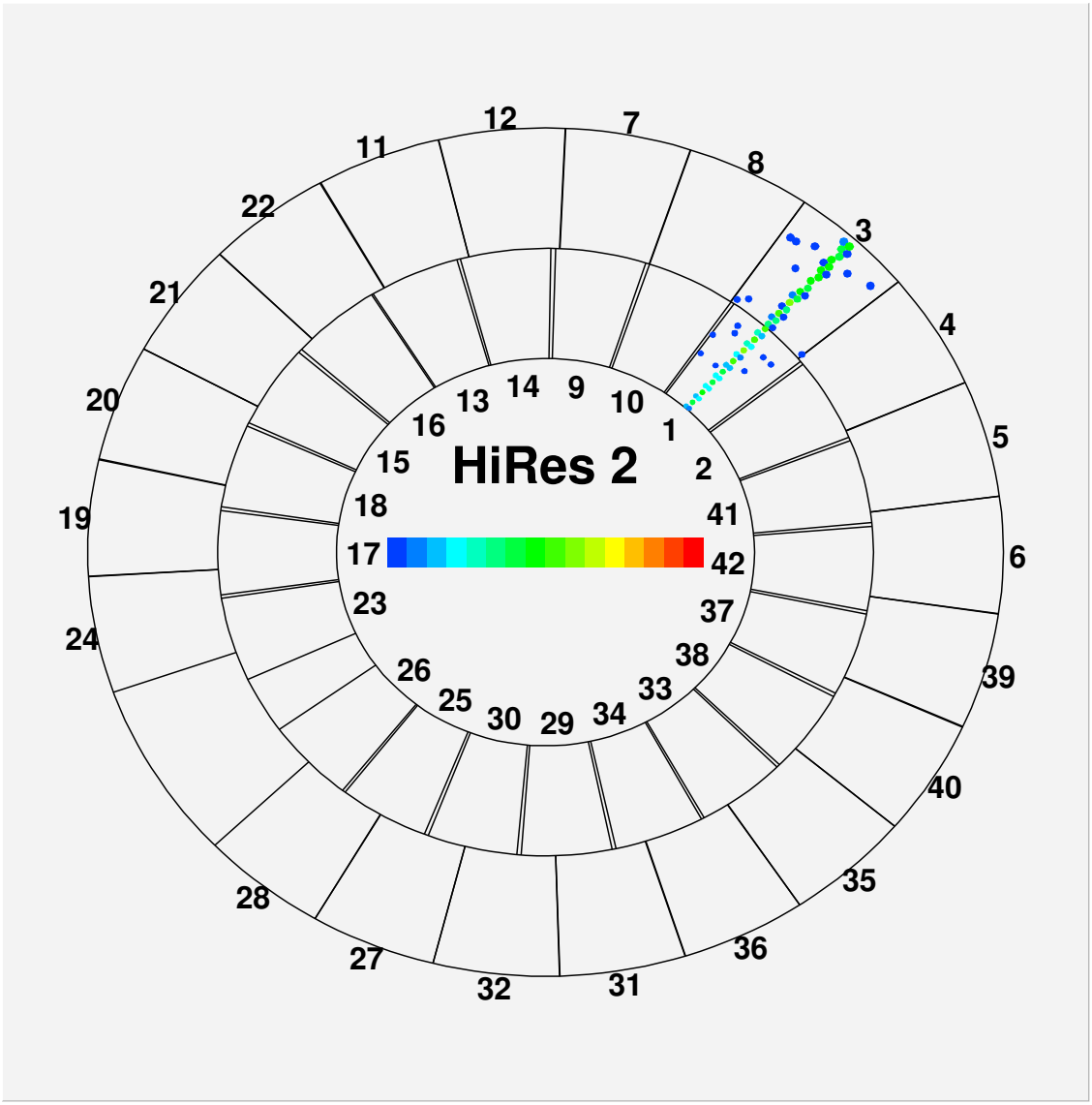

Figure 5.29. Flasher track. Clear atmosphere.

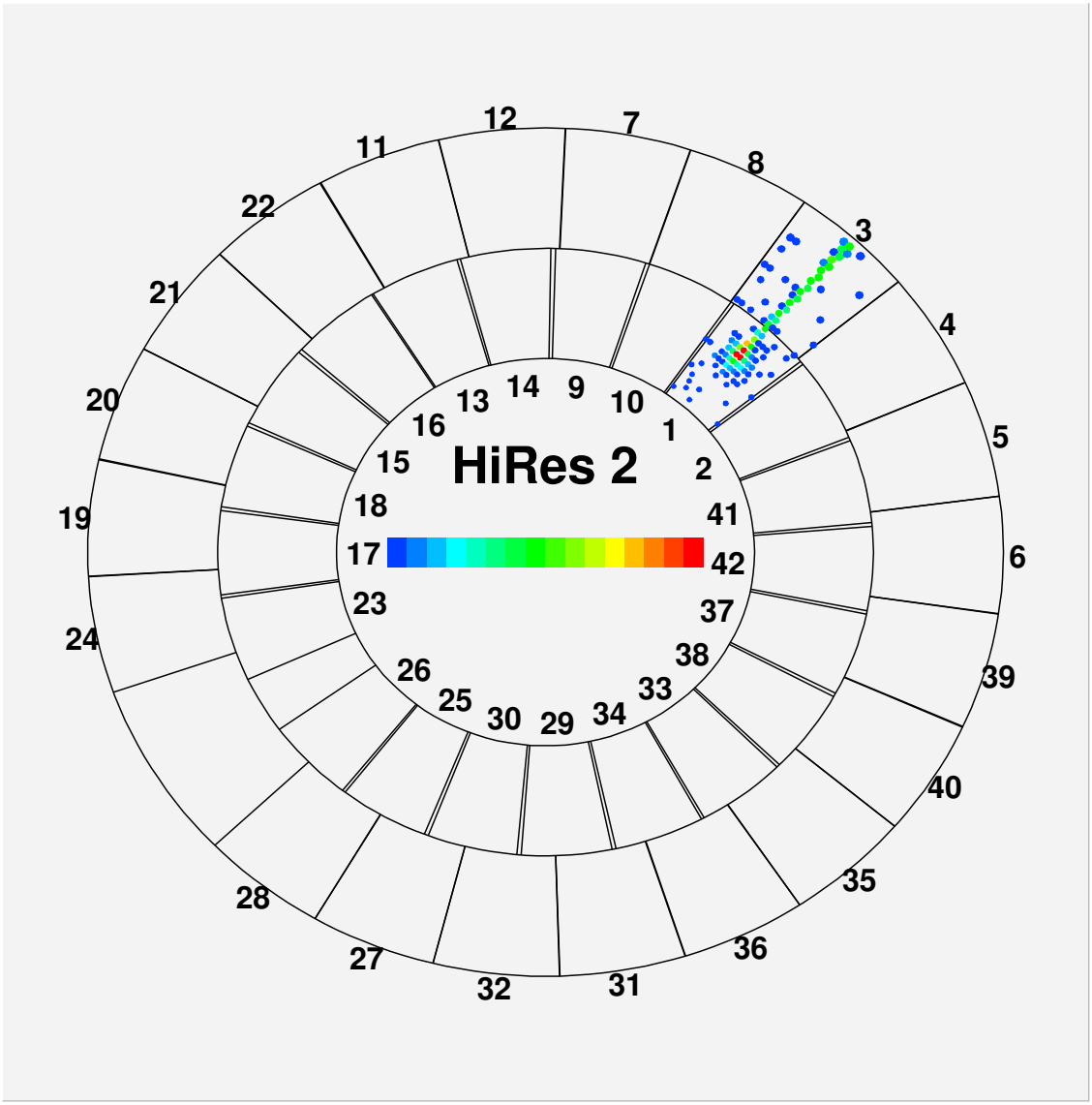

Figure 5.30. Flasher track. Cloudy weather.

fifth digit is an overhead (more than 20 degrees in elevation) cloud coverage (see Table 5.2).

The sixth digit of the weather code indicates the thickness of the overhead clouds. A 0 indicates a clear sky or a visibility of the stars through the clouds. A 1 indicates that the stars are invisible though the cloud coverage.

The last digit of the weather code is for haze indication. A 0 indicates no visible hazy, and a 1 indicates a hazy condition.

For example a 1100000 weather code indicates some clouds in north and east directions with clear overhead and no hazy.

This code is later used to select the data, taken during the desired weather condition.

5.4.2.6 The Cloud Monitors

Cloud monitors provide additional information about the cloud coverage during the data taking. There are 11 fixed wide angle cloud monitors, also called "horizon monitors," and one high resolution steerable cloud monitor, also referred as "scanning monitor."

The horizon monitor is an IR sensor with the sensitivity limited to 7–13 μm. It measures the temperature difference between the sky within its field of view of about 30° and the device aluminum canister. Eleven monitors cover about 330° in azimuth and 30° in elevation. The information from four of the monitors looking at north, east, south and west is displayed as plots in real time during data taking.

The scanning monitor utilizes the same IR sensor as the horizon monitors. Its field of view is limited to 3° by a fresnel lenz. The sensor is mounted on a pan-and-tilt platform which allows for a full sky scan to be completed in about 12 minutes. The scan data are recorded into a file and displayed on the computer monitor as an image. This image assists the observer in making a decision about the current cloud coverage.

A detailed description of both cloud monitoring systems is given in [76].

Table 5.2. Weather code: overhead coverage index.

overhead index	cloud coverage
0	clear
1	$< 1/4$
2	$< 1/2$
3	$< 3/4$
4	$> 3/4$

5.4.2.7 Measured Parameters of Utah Desert Atmosphere.

Rayleigh scattering by the molecular part of the atmosphere is stable and well known. "The US Standard Atmosphere" [77] is used to describe the atmospheric pressure change with altitude. Aerosol scattering by all other particles in the atmosphere is much more complex however. Matthews [78] describes the theoretical aspects of the light transmission correction due to aerosol scattering. Measurements done utilizing the HiRes2 steerable laser system have shown that the Dugway atmosphere is much clearer than "US standard desert atmosphere"[77]. Using a dirtier atmosphere leads to an overestimation of the primary particle energy. The aerosol density is described in a simplified model. In this model, the aerosol density falls exponentially with altitude. The parameters used in this model are: vertical scale height (H_s) and horizontal attenuation length (L_A). Assuming the light propagates from height h_1 to height h_2 and travels a distance dl we use:

$$T_A = e^{\frac{H_s dl}{(h_2 - h_1) L_A}(e^{-h_1/H_s} - e^{h_2/H_s})}, \tag{5.6}$$

where T_A is aerosol part of the optical transmission. This expression is usually simplified to:

$$T_A = e^{-AOD/\sin\theta}, \tag{5.7}$$

where

$$AOD = -H_s/L_A \tag{5.8}$$

– the total aerosol vertical depth and θ is the elevation angle [79]. The HiRes2 steerable laser system shots viewed by HiRes1 were used to measure the AOD at Dugway. A detailed discussion on this measurement is given in [79]. After subtracting the light losses due to Rayleigh scattering, T_A is "tuned" to recover the "missing" light. H_s is determined independently using vertical laser shots. The measured distributions for vertical AOD (VAOD) and horizontal attenuation length (HAL) are shown in Figure 5.31. The details about these measurements can be found in [80].

The following values of the parameters are used for the data reconstruction: $H_s = 1\ km$, $L_M = 25\ km$, $AOD = 0.04 \pm 0.02(stat) \pm 0.02(sys)$.

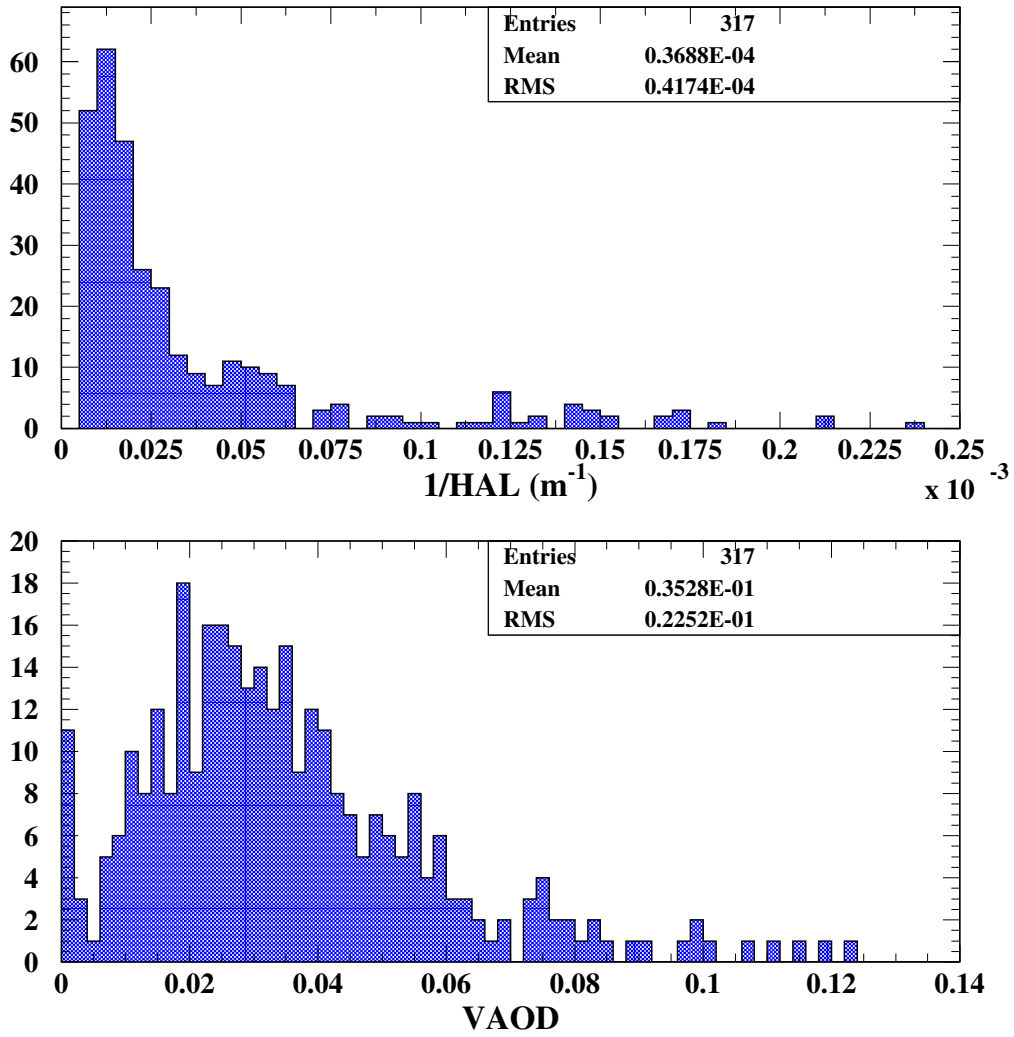

Figure 5.31. Measured VAOD and HAL.

CHAPTER 6

DATA

This chapter briefly describes all the stages of data processing. The reader is referred to [81] for additional details.

Because of the amount of raw data produced by each detector, the data can not be processed in real time. The data are first stored in a network packet format locally. The data then go through several processing stages, referred to as "passes," before the data are ready for the final analysis. Each processing stage is executed by a separate set of routines. Thus, when any of the input parameters, such as the atmosphere or the calibration is modified, it is not necessary to reprocess the data from the beginning. Only the affected stages need to be redone. This saves computational time and disk space.

The HiRes data storage utilizes a Data Summary Tape (DST) format. In the DST format, the data are stored in files by blocks. Each block contains one event and begins with the "START" and ends with the "END" keywords. Each event usually contain several data banks. A bank is an equivalent to a common block in FORTRAN or to a structure in the C programming languages. As the data go through more and more passes, the number of banks increases as more information is known about each event.

The raw data are stored in different file types. The data collected nightly for HiRes1 include:

- PKT – cosmic ray data;
- DIAG – electronic diagnostics;
- CAL – electronic calibration;
- NOISE-CLOSED & NOISE-OPEN -electronic noise with opened and closed mirror doors;
- YAGMIR-OPENED & YAGMIR-CLOSED – YAG calibration light emitted from the mirror fibers;

- YAGCLU-OPENED & YAGCLU-CLOSED – YAG calibration light emitted from the cluster fibers;

The data collected nightly for HiRes2 includes:

- FPKT1 – cosmic ray data;
- TEST – pedestal data;
- PULSER – electronic diagnostics;
- YAG12 – YAG calibration light emitted from the mirror fibers;
- YAG34 – YAG calibration light emitted from the cluster fibers;

The RXF calibration data are also collected between runs. See Section 5.4 for details about HiRes calibration data.

6.1 Data Transfer

The raw data are transferred nightly from the detector main computers to the HiRes servers at the University of Utah and Nevis Laboratories where all the processing is done independently.

6.2 PASS0

This is the first stage in data processing. The data are converted from the raw packet network format to the DST format. Because the raw packet format is different for HiRes1 and HiRes2, different routines are used for PASS0.

6.3 PASS1

At this stage, the number of photoelectrons is calculated using the calibration data taking into account measured mirror reflectivity, UV filter transmission, PMT gain and quantum efficiency (see Section 5.4 for details).

For the HiRes2, PMT gains are adjusted so that one FADC count is produced by one photo-electron. This is done by initially gain balancing each PMT within the cluster using the adjustable digital to analog converter amplifier (see Section 5.3.4 for description of the FADC system). The total number of photo-electrons is found by integrating the signal using the average quantum efficiency.

If multiple mirrors are triggered by an event, the information from all mirrors is combined into a single event. Thus, a multiple-mirror event is formed.

To find stereo events, time matching is done between the sites. A GPS clock is used to synchronize both detectors. If two detectors are triggered by an event within a 1 ms time window, this event is considered as a stereo candidate and put into a separate file.

The next step in the data processing is removing of the known sources. Reil [81] gives a detailed description of known source removal. Here we summarize briefly.

Known light sources to be removed include noise and artificial events:

- The HiRes1 and HiRes2 steerable laser;
- the roving steerable laser;
- the Terra laser;
- the vertical xenon flashers.

HiRes1 and HiRes2 steerable laser tracks and the roving laser tracks are removed by looking at the event time stamp. The GPS time when the lasers fire is known precisely. If the event falls within a 3 ms window around the expected laser firing time, the event is removed from the data stream and put into a special file for further atmospheric analysis.

The location and the GPS time of the Terra laser are known precisely, and its tracks are removed the very same way as for the other lasers. The Terra laser fires only vertical shots. These events can be removed using their geometry and time information.

The laser events account for about 6% of the total number of events.

The vertical flashers are removed based on their known geometry and the light angular speed as seen by the detectors. They account for about 2% of the total number of events. Cross checking the GPS using these events is possible only if they are seen in stereo.

6.4 PASS2 – Rayleigh Filter

The HiRes software uses a Rayleigh filter to filter out most noise events. The tube triggering order within each mirror is first established based on each tube's trigger timing information. A unit vector is next built from the first triggered tube to the next and so on until the last triggered tube is reached. The sum of these unit vectors is the Rayleigh vector $\overrightarrow{r}$. We next check if the probability of a total displacement R created by a random

walk is less than 1%, which is a compromise between an efficient noise filtering and loosing the real CR events. This probability is given by:

$$P(r > R) = e^{-R^2/n}, \tag{6.1}$$

where n is the number of unit vectors. Events that do not satisfy this condition are removed as noise. $\overrightarrow{r}$ also classifies the events as up going or down going using timing information. If an up going event has not been removed previously as a known source, it is cut off here. Events within 20° to the horizon are removed as well because the detector time resolution does not allow us to distinguish these events from upgoing ones. In total, the noise filter removes more than 91% of the events. Ref. [82] gives a complete description of the HiRes noise filter.

6.5 PASS3 – Plane Fitting

An amplitude weighted plane fit is performed by minimizing χ^2:

$$\chi^2 = \sum_i^n \frac{(\hat{n} \cdot \hat{n_i})S_i}{\sigma_i^2}, \tag{6.2}$$

where $\hat{n}$ is the plane normal, $\hat{n_i}$ is the tube pointing direction, S_i is the tube signal. The normalized error in the tube signal is calculated as:

$$\sigma_i^2 = \frac{S_i + S_n}{S_i}, \tag{6.3}$$

where S_n is the tube noise.

This procedure determines the shower-detector plane (SDP). Once the SDP is determined, we are ready for the next step, shower geometry reconstruction.

6.6 PASS4 – Shower Geometry and Binning

Once we know the SDP for both detectors, the shower geometry is fixed by their cross-product:

$$\hat{m_{tk}} = [\hat{n_{h1}} \times \hat{n_{h2}}], \tag{6.4}$$

where $\hat{n_{h1}}$ and $\hat{n_{h2}}$ are the HiRes1 and HiRes2 SDP normals correspondingly.

Once the shower geometry is established, we can now split the shower into bins. We must reconstruct the number of charged particles in the shower as a function of the shower slant depth.

6.6.1 Angular Binning

Only the total charge and the trigger time are known for each HiRes1 tube. This means we can do only so-called "angular binning." The track is split into bins, with each bin equal to 1°. The signal in the bin is calculated based on the overlap of the PMT's field of view with that bin. The total light flux for each bin is equal to:

$$\Phi_i = \frac{N^i_{pe}}{A^i_{eff}}, \tag{6.5}$$

where N^i_{pe} is the number of photo-electors contributing to that bin and A^i_{eff} is an effective mirror area for that bin. It should be noticed that many different factors are included in A^i_{eff}, so it is more reasonable to call this a correction coefficient. The factors that must be taken into account include:

- the position of the tube in the cluster;
- the tube response profile;
- the shower lateral distribution.

The tube position in the cluster determines the tube obscuration due to the cluster box, the image spot size due to mirror optics, and the dead space between the tubes. All these corrections are done using so called "ray tracing." In practice, a different ray-tracing table is used for each PMT in the cluster. The ray-tracing table averages the photon-by-photon ray trace over the tube. As a result, we have the correction factor for each PMT in the cluster as a function of the angular distance to the light source. An example of the ray-tracing function for one tube is shown on the Figure 6.1.

Since all HiRes tubes are tested in the laboratory (see Section 5.4.1.1), we know the response profile for each of the tens of thousands of tubes in both HiRes detectors. In practice, however, an average PMT response profile is used. See Figure 5.17.

The shower lateral distribution, which results in a broadening light source, is approximated by the NKG function, which is described in 8.2.

6.6.2 Time Binning

A different approach to binning can be used for FADC system where timing information is available. The number of bins is selected for each shower as a compromise between having enough bins to do a good profile fit, and avoiding excessive statistical

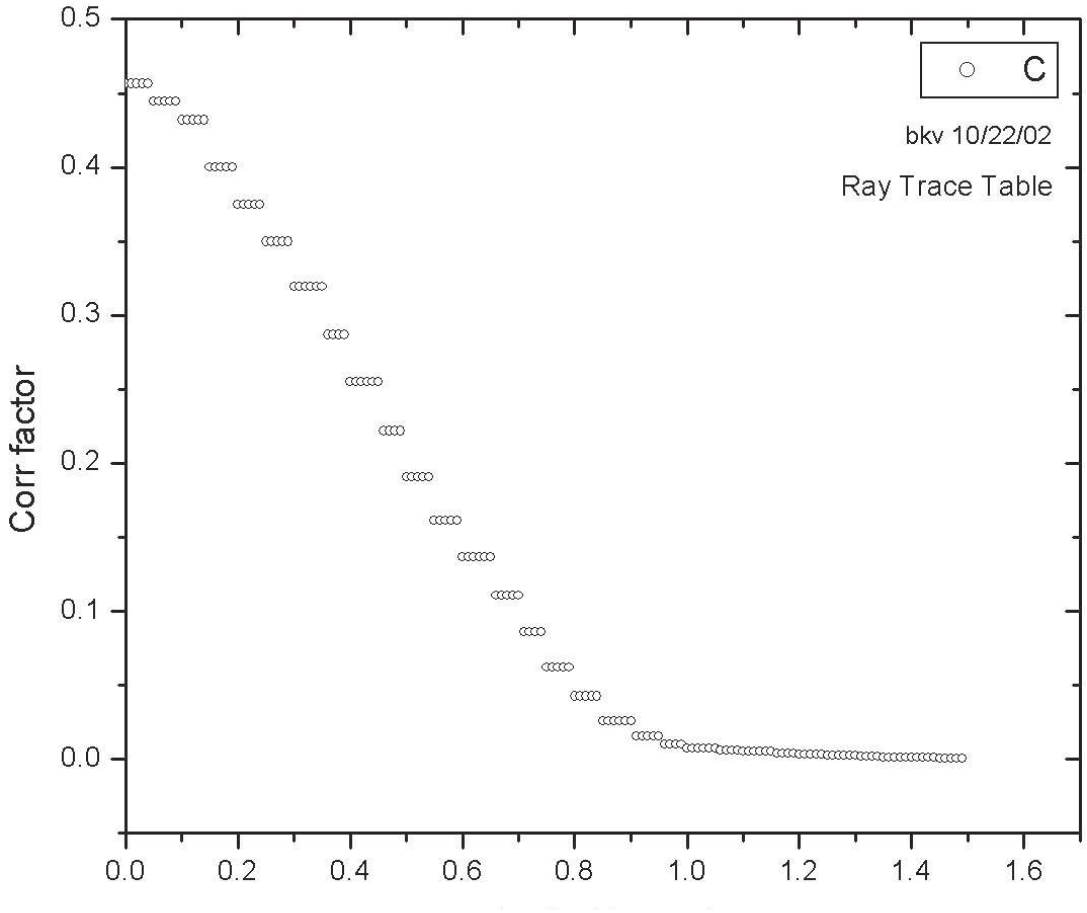

Figure 6.1. Ray-trace table.

fluctuations. The shortest time bin to be used is 100 ns. This is the hardware limit. The longest practical bin used is 600 ns. The bin angular size distribution for some of the cosmic ray stereo event candidates is shown in Figure 6.2. Next, for each time bin the total flux is calculated using:

$$\Phi_j = \frac{\sum_1^n N_{pe}^i}{\sum_1^n A_{eff}^i}, \tag{6.6}$$

where n is the number of tubes which trigger within the time bin. The other parameters have the same meaning as in 6.5.

The time binning allows us to improve the quality of the profile fit, and thus, to improve the energy and X_{max} resolution, which has a great impact on this work.

In rare cases where the time binning fails for the FADC, it is still possible to use standard angular binning. If both fail, however, the event can not be reconstructed and is discarded.

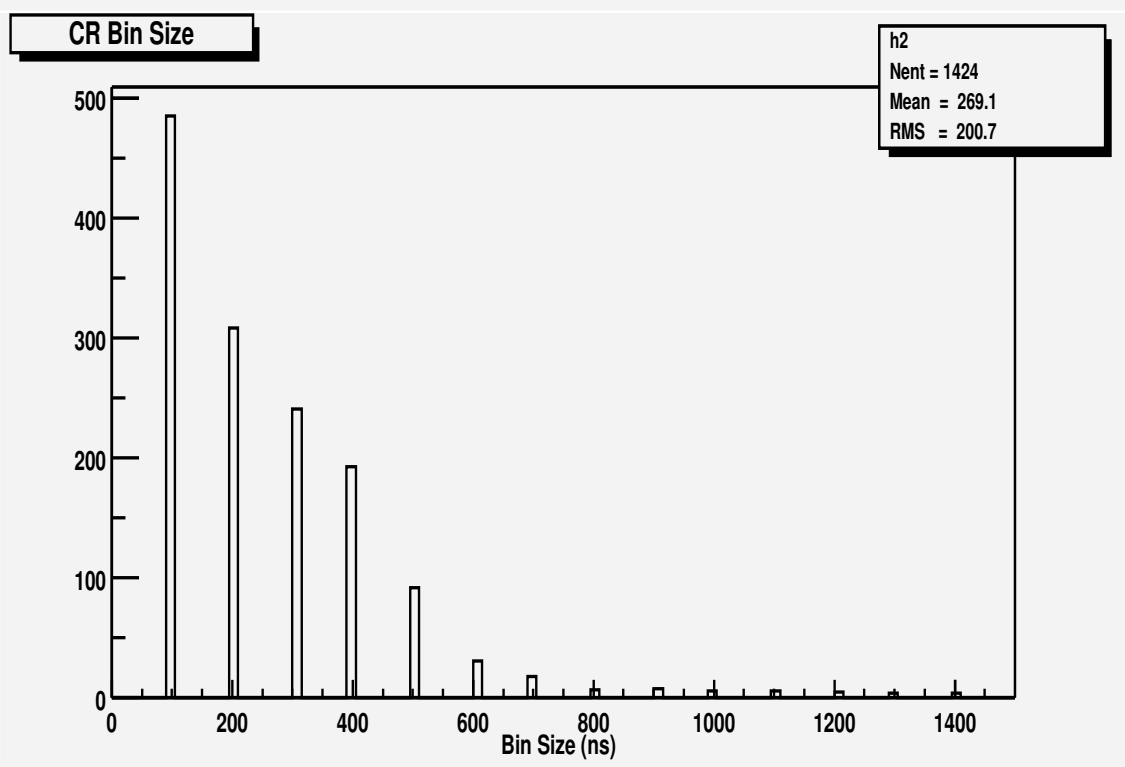

Figure 6.2. Time bin size distribution.

6.7 PASS5 – Profile Fitting

After Φ_i is known for each bin, the shower profile reconstructing is attempted. First, for each Φ_i a corresponding predicted value Φ_i^{GH} is calculated by assuming a Gaisser-Hillas shower profile (see Section 8.1.1). Next, the χ^2:

$$\chi^2 = \sum_1^N \frac{(\Phi_i - \Phi_i^{GH})^2}{\sigma_i^2} \tag{6.7}$$

is minimized, where σ_i is the error calculated using Poisson statistics and adding the measured sky noise:

$$\sigma_i^2 = (N_{pe}^i)^2 \sigma_{A_{eff}^i}^2 + \sigma_{N_{pe}^i}^2 / A_{eff}^i, \tag{6.8}$$

Here the sky noise contribution is:

$$\sigma_{N_{pe}^i}^2 = {N_{pe}^i}^2 + 40^2, \tag{6.9}$$

where 40 is the average amount of photo-electrons each tube gets in a trigger due to the dark sky noise. A real time measurement of the sky noise is possible, but was not implemented yet at the time of this study. The correction A_{eff}^i is determined from the Monte Carlo study by varying the shower geometry.

Figures 6.7 and 6.7 illustrate typical profile fitting curves for the HiRes1 and HiRes2. Figures 6.5 and 6.6 give the reader an idea of how the same events look on HiRes event displays.

The profile fitting gives us the X_{max} directly. The energy of the shower is than reconstructed, as described in Chapter 8.

The final step in the data processing is postprocessing quality cuts, which are described in detail in Section 8.6.

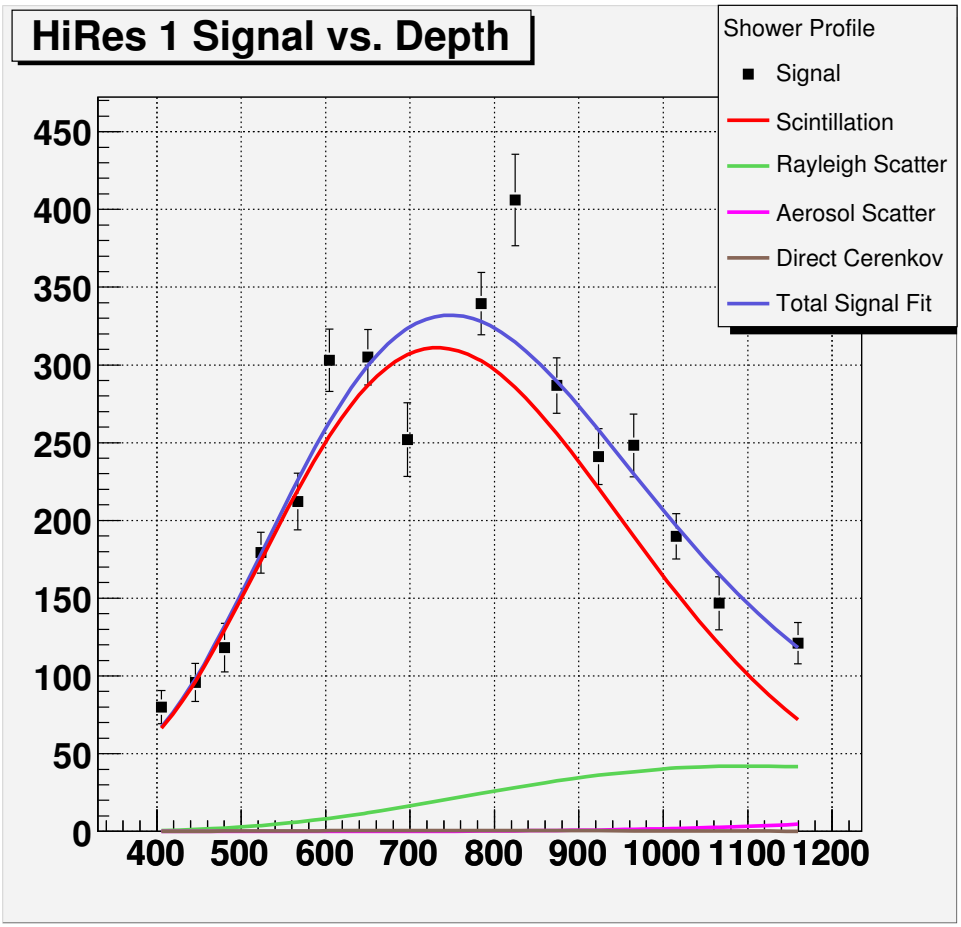

Figure 6.3. HiRes1 binning and profile fit.

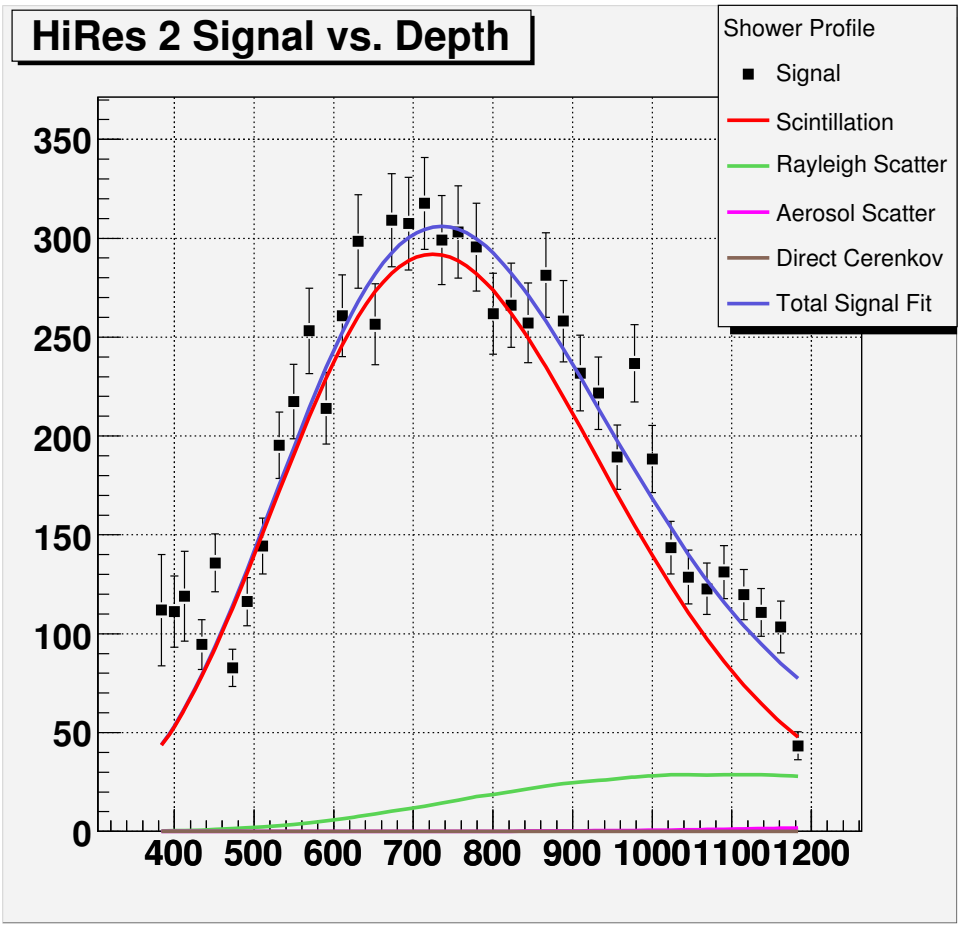

Figure 6.4. HiRes2 time binning and profile fit.

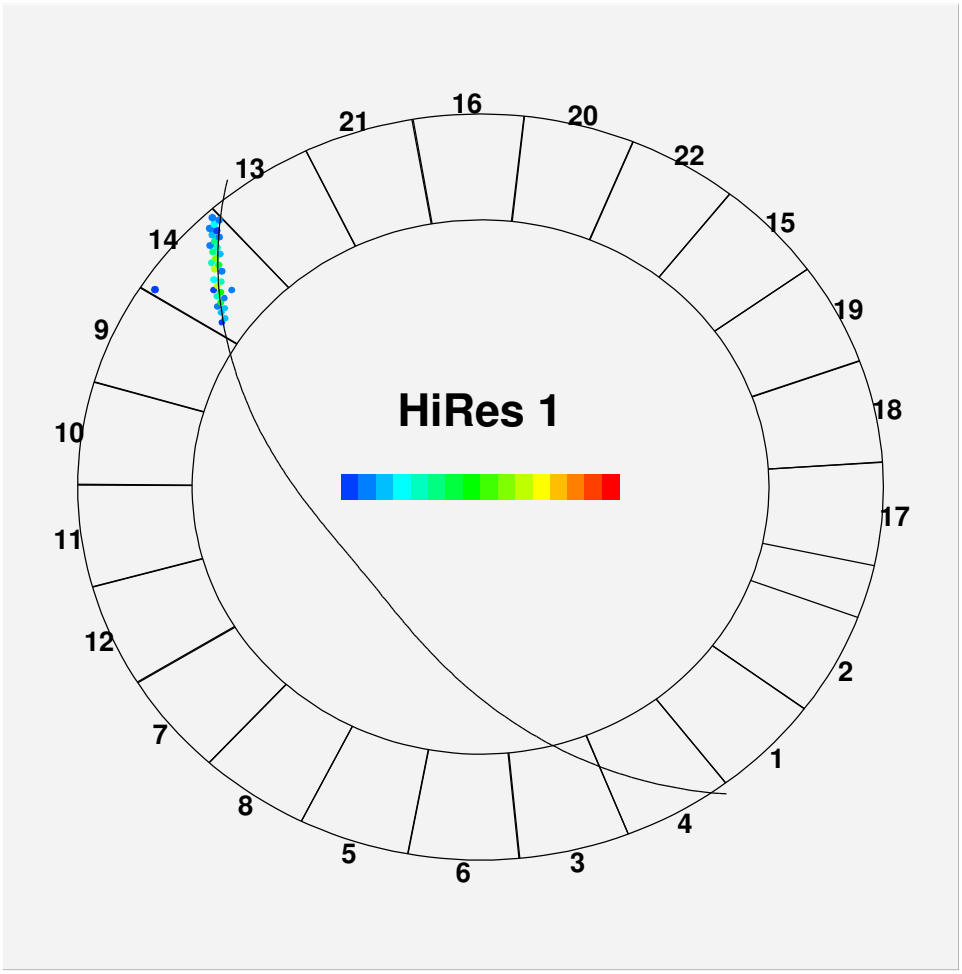

Figure 6.5. HiRes1 event display.

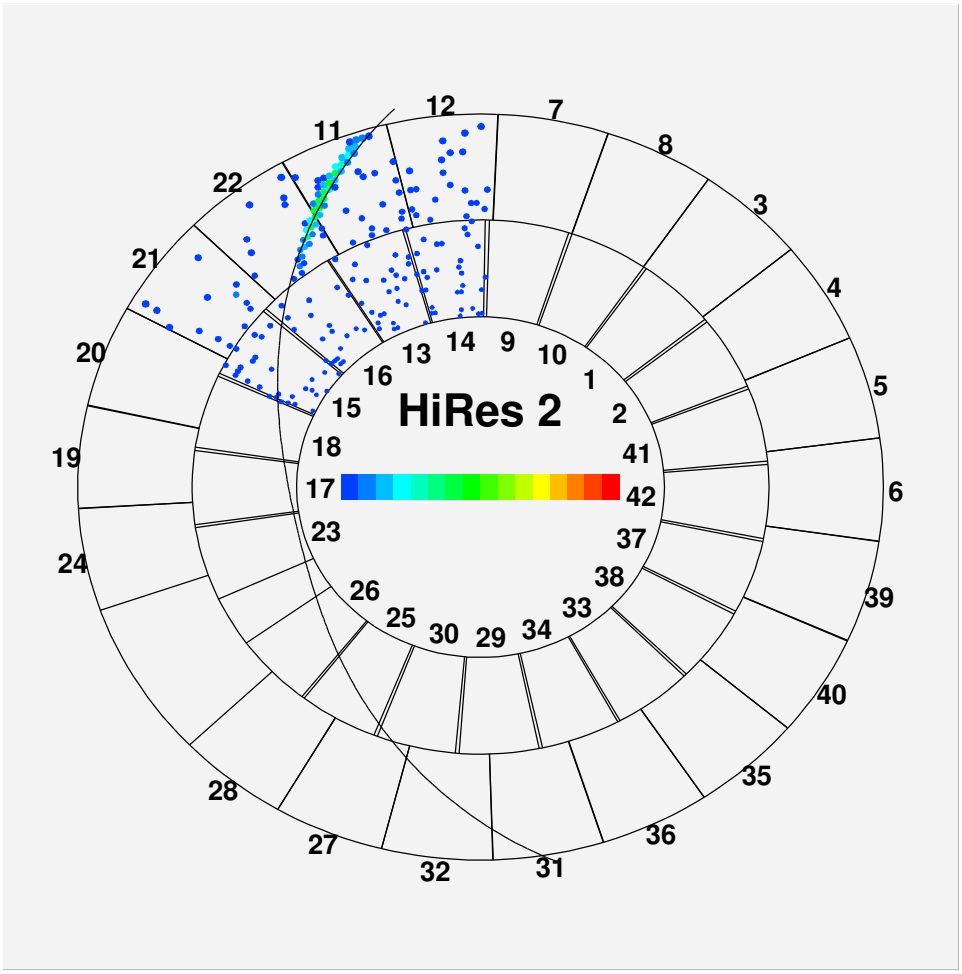

Figure 6.6. HiRes2 event display.

CHAPTER 7

P–AIR INELASTIC CROSS–SECTION MEASUREMENT TECHNIQUE

7.1 Observable Data

It is possible to measure the following parameters of UHECRs:

- energy of the primary particle;
- the air shower profile – the number of charged particles in the air shower vs. shower depth in the atmosphere;
- the arrival direction.

The atomic mass of the primary particle, however, can not be determined on a shower by shower basis. One has to use a statistical analysis to distinguish one group of showers from another. A precise arrival direction measurement is relevant only to an anisotropy study. A correct shower geometry reconstruction, however, helps to improve the air shower profile measurement and, thus, the estimation of the primary particle energy and the depth of the air shower maximum (X_{max}). Stereo measurements fix the shower geometry and, thus, greatly reduce the errors in the primary particle energy and the shower profile reconstruction. X_{max} is used to obtain p-air inelastic cross-section(σ_{in}^{p-air}).

7.2 Previous Results

The exponential slope of the X_{max} distribution has been shown to be related to σ_{in}^{p-air}. Indeed, as discussed in 7.3.1, there should be a relationship between the point of first interaction distribution and the X_{max} distribution. Baltrusaitis et al. [5] used this method successfully in the first σ_{in}^{p-air} measurement at $10^{17.5}$ eV. This method requires fitting the tail of the X_{max} distribution to obtain the exponential index, as shown in Figure 5 in [5]. The later is then related through a coefficient, k (see eq. (7.1)), to the proton mean free path λ_{p-air} by Monte Carlo simulation studies, similar to the ones

conducted for this dissertation. Baltrusaitis et al. [5] found σ_{in}^{p-air} to be $530 \pm 66 g/cm^2$ at 30 TeV center-of-mass energy.

$$\Lambda = k\lambda_{p-air} \tag{7.1}$$

In this thesis we present a novel technique for measuring σ_{in}^{p-air} using the HiRes stereo fluorescence detector CR data.

7.3 Measurement Technique

To measure σ_{in}^{p-air} using HiRes stereo fluorescence CR data the deeper part of the X_{max} distribution is fit by an empirical integral function. The only fitting parameter of this function, aside from normalization, is λ_{p-air}. Air shower fluctuations in the air are then described by a special complex function with three parameters.

7.3.1 Deconvolution Method

When a high energy particle enters the atmosphere, it will travel freely until it interacts with an air atom. The magnitude of this mean free path (X_1) depends solely on the particle total cross-section with the air and contributes to EAS fluctuations. From purely statistical considerations, the distribution of the point of first interaction, which will be referenced as distribution I, will be exponential (see Figure 7.1) with the exponential index (slope) by definition equal to the particle mean free path in the air, λ_{p-air}. The form of this distribution does not depend on the nature of the particle or the matter it is interacting with, but the magnitude of the slope does. This first interaction point distribution is one element of the shower development fluctuations.

After the first interaction occurs, the air shower starts to develop. The air shower development is described in Chapter 4. A shower profile is shown in Figure 2.2 as the number of charged particles vs. the slant depth. We take the point where the shower reaches its maximum, X_{max}, as our reference point. Any other point on the shower profile can play this role, but X_{max} is uniquely identified and relatively easy to measure by fitting the shower profile to a functional form (8.1). The cascade development from the point of first interaction to X_{max} is subject to statistical fluctuations. These fluctuations differ in nature from fluctuations in the point of first interaction, as described in Chapter 4. The simulated distribution of $X^{'} = X_{max} - X_1$ caused by shower development fluctuations in air, which will be referred to as distribution II, is shown in Figure 7.2.

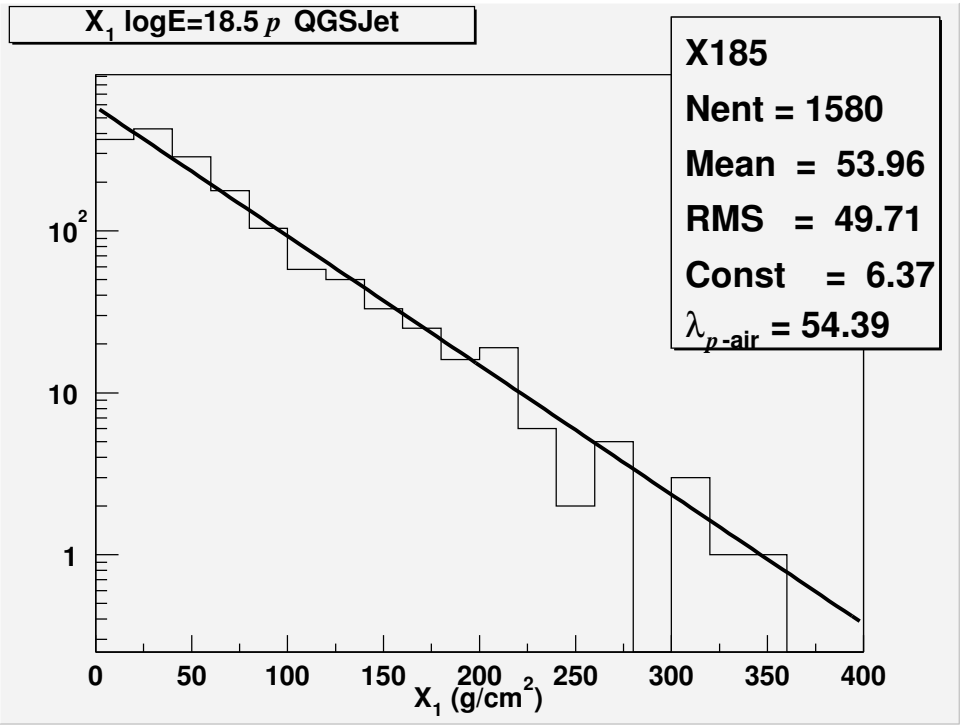

Figure 7.1. Point of first interaction distribution.

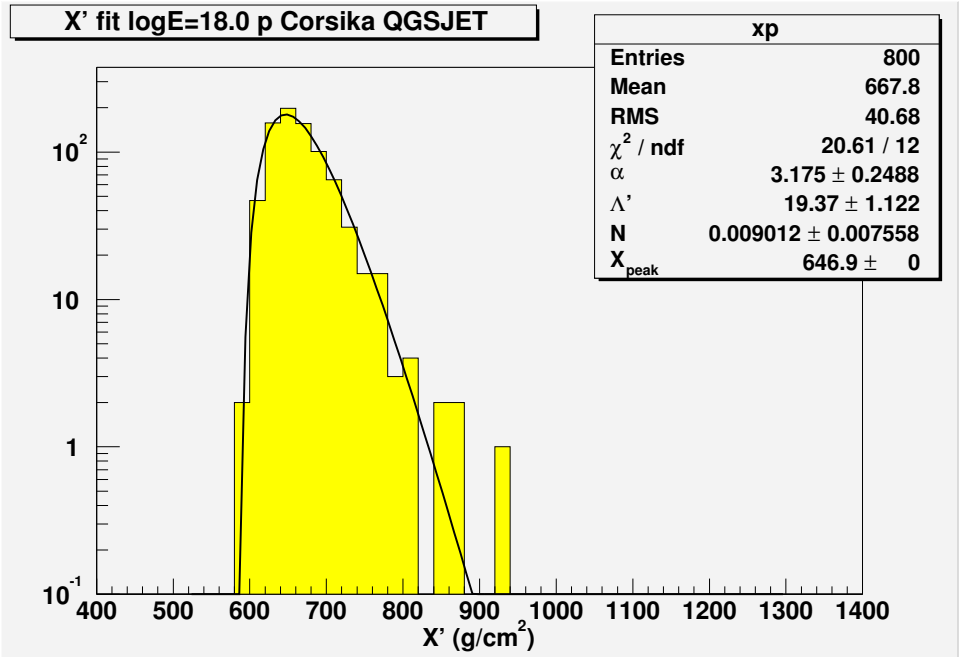

Figure 7.2. X' fit.

From the above considerations, the X_{max} distribution can be considered as a convolution of the distributions I and II. Fitting the X_{max} distribution with a function, which is a convolution of these two forms, should yield λ_{p-air} directly if distribution II can be robustly parameterized.

The form of the distribution I is known. To study and parameterize distribution II an extensive Monte Carlo simulation has been conducted.

7.3.2 Monte Carlo Studies

The Monte Carlo (MC) study pursues several goals:

- find the functional form to fit distribution II;
- develop a set of quality cuts for the data selection;
- study the detector resolution function;
- estimate systematic errors due to possible bias introduced by the detector itself as well as the data reconstruction and event selection procedures.

The MC study consists of two major stages: air shower simulations and detector MC study.

In the first stage, extensive air showers initiated by high energy particles are simulated. Our cross-section measurement technique was developed and tested by studying the properties of simulated air showers. These showers were then used for the second stage, where the detector response was simulated. This helped to develop the data reconstruction programs and to study the detector resolution and estimate systematic errors.

7.3.2.1 Air Shower Simulations

For the air shower simulations Corsika package v.6.003 has been used. The detailed description of the package can be found elsewhere [53]. A large library of air showers at fixed energies has been generated. The major part of the work was done for showers initiated by proton and iron primaries. γ and α-particle induced showers have also been generated for specific tests. The generated showers are summarized in Table 7.1. X_1, X_{max} and $X^{'}$ points were found for the simulated air showers and X_1, $X^{'}$ and X_{max} distributions were created for each energy bin.

Table 7.1. Corsika simulated air showers.

$log_{10}E$	QGSJET			SIBYLL		EGS4
log(eV)	p	Fe	CNO	p	Fe	γ
17.0*	792	800	800			
17.1	500					
17.2	500					
17.3	500					
17.4	500					
17.5*	800	603	800			
17.6	500					
17.7*	800	773	800			
17.8	500					
17.9	500					
18.0*	800	800	725	800	800	1000
18.1	500					
18.3	1000					
18.4	500					
18.5*	1580	2000	1880			1000
18.6	500					
18.7*	873	800	800			500
18.8	500					
18.9	500					
19.0*	850	800	800	800	800	750
19.1	500					
19.2	500					
19.3	500					
19.4	500					
19.5*	1768	1760	1715			800
19.6	500					
19.7*	699	800	790			671
19.8	740					
19.9	682					
20.0*	920	800	810	800	800	786
20.1	482					
20.3	342					
20.4	282					
20.5*	286	742	807			

7.3.2.2 Point of First Interaction Study

Distribution I was fit by an exponent 7.2 for each energy bin denoted by a star in Table 7.1.

$$e^{-\frac{x_1}{\lambda_{p-air}}} \tag{7.2}$$

The fitting is shown in Figure 7.1. The exponential index referred to as the slope in these figures is $1/\lambda_{p-air}$ and depends on the value of σ_{in}^{p-air} imbedded in the Corsika code. This λ_{p-air}, obtained from the X_1 distribution, will be referred as Λ_1 further on and is the input for our study.

7.3.2.3 $X^{'}$ Distribution Study

$X^{'}$ was calculated for all air showers for each energy bin mentioned in Section 7.3.2.2. After the $X^{'}$ distribution was plotted for each energy bin, it became clear that such a distribution can be approximated by a simple functional form:

$$P(X') \propto [\frac{X' - X_{peak} + \alpha\Lambda'_m}{e}]^{\alpha} e^{-\frac{X'-X_{peak}}{\Lambda'_m}}, \tag{7.3}$$

where X_{peak}, α and Λ'_m are the parameters obtained by fitting. Their values are summarized in Table 7.2. The search for the parameters was done in two steps. First all three parameters were allowed to be free. X_{peak} as a function of energy was obtained by fitting the $X^{'}$ distribution (see Figure 7.3).

Table 7.2. X' fitting parameters.

$log_{10}E$	X_{peak}	α	Λ'_m
17.0	594	3.28 ± 0.29	21.6 ± 1.3
17.5	620	2.44 ± 0.19	23.5 ± 1.3
17.7	631	3.20 ± 0.22	19.9 ± 1.1
18.0	647	3.18 ± 0.25	19.4 ± 1.1
18.5	673	2.09 ± 0.12	24.1 ± 0.9
18.7	684	2.49 ± 0.14	22.5 ± 1.1
19.0	700	2.19 ± 0.14	24.1 ± 1.2
19.5	727	2.86 ± 0.14	21.1 ± 0.8
19.7	737	2.18 ± 0.17	24.3 ± 1.4
20.0	753	2.45 ± 0.24	22.9 ± 1.3
20.5	780	2.10 ± 0.22	24.0 ± 2.1

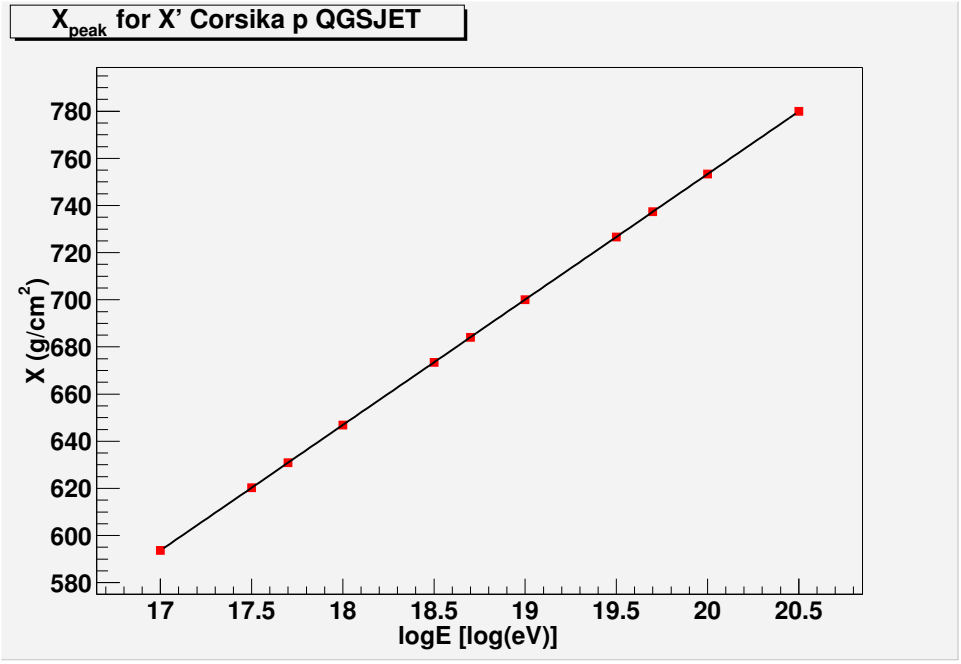

Figure 7.3. X_{peak} as a function of energy.

Next, X_{peak} was fixed to be:

$$X_{peak} = 53.21 \times \log E - 310.9 \ g/cm^2 \tag{7.4}$$

and α and Λ'_m values were obtained by refitting the same distribution with X_{peak} calculated from 7.4. An example of such a fit is shown in Figure 7.2. Finally, α was approximated by:

$$\alpha = -0.169 \times \log E + 5.628 \tag{7.5}$$

(see Figure 7.4) and Λ'_m was fixed as a constant:

$$\Lambda_m = 22.2 \ g/cm^2 \tag{7.6}$$

(see Figure 7.5). Thus, function (7.3) becomes known function of energy.

7.3.2.4 X_{max} Distribution Study

Once 7.3 is known, it is possible to fit the X_{max} distribution with a convolution function:

$$f(x_m) = \int_0^{x_m - x_{peak} + \alpha\Lambda'_m} \frac{N}{\lambda_{p-air}} e^{-\frac{x_1}{\lambda_{p-air}}} [\frac{x_m - x_1 - x_{peak} + \alpha\Lambda'_m}{e}]^\alpha e^{-\frac{x_m - x_1 - x_{peak}}{\Lambda'_m}} dx_1, \tag{7.7}$$

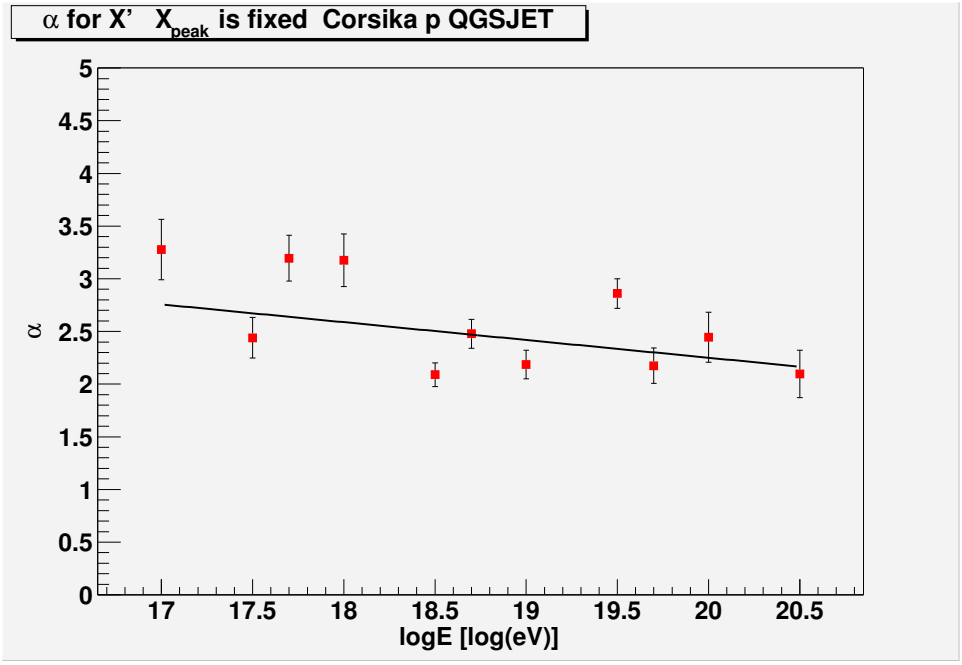

Figure 7.4. α as a function of energy .

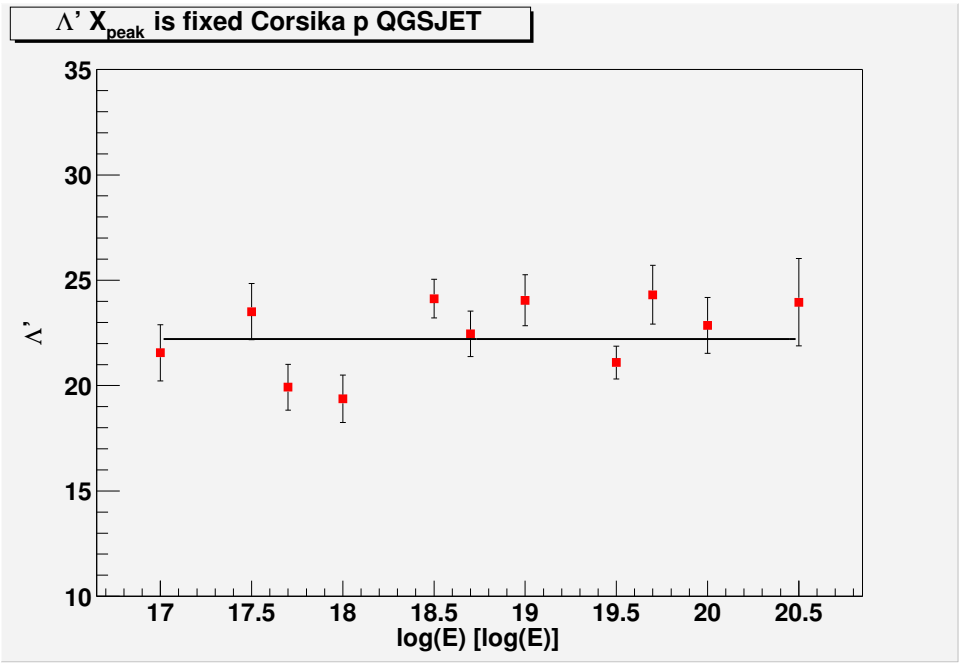

Figure 7.5. Λ_m as a function of energy .

where λ_{p-air} is the only fitting parameter, except for the normalization N. To test the technique, a comparison between Λ_1 and λ_{p-air} is made. Both numbers are shown in Figure 7.6 vs energy. The results are in agreement within statistical errors.

7.3.2.5 CR Composition Influence

Heavier nuclei can change the form of X_{max} distribution and thus influence the results. Since heavier nuclei tend to develop earlier in the atmosphere, their X_{max} is shifted towards shallower slant depths. A recent study of CR composition [51] demonstrates that at the highest energies only 20% of the CR primaries are heavier nuclei. As an example, Figure 7.7 shows the possible influence of 20% iron on the X_{max} distribution fitting using equation 7.7 at 10^{18} eV. The contribution of heavy nuclei can be almost completely avoided by cutting on $X_{max} > 740\ g/cm^2$. After this cut, the 20% of iron contamination contributes less than 1% to the systematic error in λ_{p-air}.

It can be concluded, that the proposed measurement technique allows us to obtain λ_{p-air} and hence, σ_{in}^{p-air}, from observable CR data.

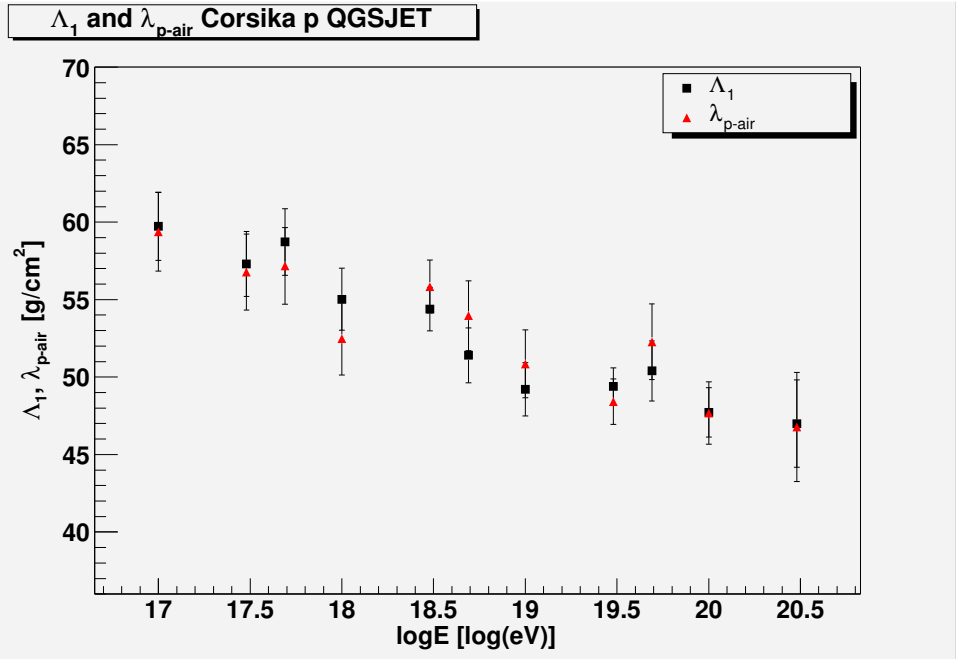

Figure 7.6. λ_{p-air} and Λ_1 as a function of energy .

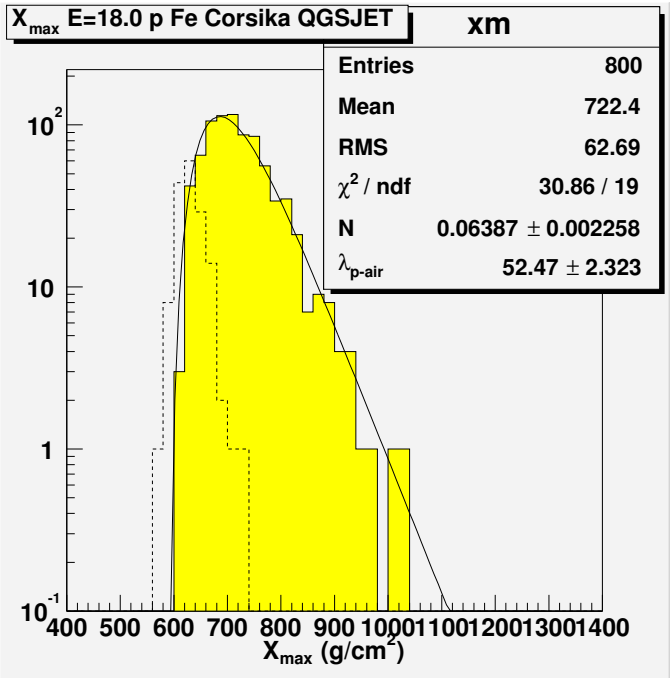

Figure 7.7. 20% iron and 80% proton X_{max} distribution.

CHAPTER 8

DETECTOR MONTE CARLO

The detector MC is a computer program designed to simulate the HiRes stereo detector response. It accurately simulates the sky noise and the finite detector time and spatial resolution. Several major steps are involved in the detector MC program. These include:

- the shower longitudinal profile;
- the shower lateral distribution;
- light production;
- light propagation;
- detector response.

The same assumptions about the shower longitudinal profile and lateral distribution as well as about the light production and propagation are also used in the real data reconstruction. All these steps will be briefly highlighted is this chapter. Reference [83] gives a detailed description of the detector MC program.

8.1 Air Shower Profile Simulation

The simulated shower profile serves as an input for the detector MC. The shower electromagnetic profile can be simulated using one of the following:

- a Gaisser-Hillas parametrization;
- a gaussian in age parametrization;
- a direct output of Corsika simulation package.

All these methods produce equivalent results.

8.1.1 Gaisser-Hillas Parametrization

An air shower longitudinal development profile can be well approximated by a Gaisser-Hillas formula [84]:

$$N(X) = N_{max}(\frac{X - X_0}{X_{max} - X_0})^{\frac{X_{max}-X_0}{\lambda}} e^{\frac{X_{max}-X}{\lambda}}. \quad (8.1)$$

There are four fitting parameters in the functional form (8.1). X_0, X_{max}, N_{max} and λ. N_{max} is the number of charged particles at shower maximum, X_{max} is the shower slant depth at the maximum, measured in g/cm^2. The later parameter has extreme importance for this work. As shown by Pryke [85] and Simpson [86] X_0 is just a fitting parameter and has nothing to do with the point of first interaction. λ is a characteristic length and is fixed at 70 g/cm^2.

By using the Corsika air shower simulations, Z. Cao showed [87] that:

$$\frac{E_{em}}{E_0} = 0.9437 - 0.0963E_{em}^{-0.126}, \quad (8.2)$$

where E_{em} is electromagnetic energy in EeV deposited into a shower, E_0 – the primary particle energy also in EeV. This empirical formula accounts for the energy that is not converted into the electromagnetic portion in the atmosphere and that is lost when the particles reach the surface and can no longer be detected.

Additionally, heavier nuclei deposit less energy into the atmosphere (see Figure 8.1). Since the fluorescence technique can not determine the primary particle atomic weight on event-by-event basis, equation (8.2) represents an average between protons and iron. The error on energy resolution introduced by this uncertainty is about 5%. The fluctuations of the mean, which are not shown in Figure 8.1 are of the order of 7%. Since the same assumptions are used for the data processing, these uncertainties are valid for the CR data as well.

Groom [88] gives the following formula to convert E_{em} into a total number of charged particles in the shower:

$$E_{em} = \frac{E_C}{X_0}\int_0^\infty N(X)dX, \quad (8.3)$$

where

$$E_C = \frac{710MeV}{Z + 0.92}. \quad (8.4)$$

Taking into account that $Z = 7.22$ – the average atomic weight of air, $E_C = 87.22MeV$ – the electron critical energy in air. Calculating equation (8.3) we vary fitting parameters X_{max} and N_{max} to conserve the ratio 8.2.

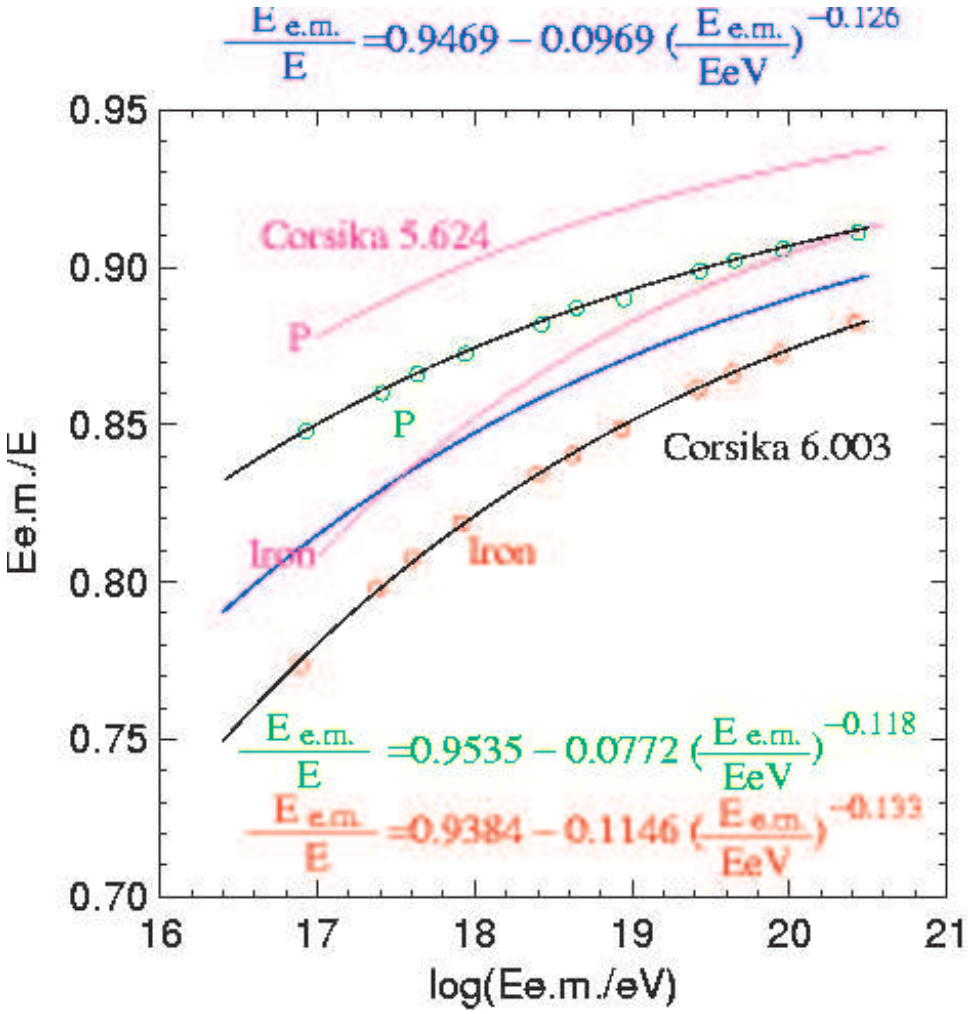

Figure 8.1. E_{em} deposit into the atmosphere.

8.1.2 Gaussian in Age Parametrization

A Gaussian-in-age parametrization of the CR showers has been recently proposed [87]. The number of charged particles in the shower can be approximated by:

$$N(X) = N_{max} e^{\frac{(s-1)^2}{2\sigma^2}}, \tag{8.5}$$

where the shower age s is defined as:

$$s = \frac{3X}{X + 2X_{max}}. \tag{8.6}$$

Equation (8.5) has fewer parameters compared to the GH formula (8.1) Unlike GH, equation (8.5) has a symmetric form. It should be noted that $s = 0$ at point X_1, the first interaction, $s = 1$ when the shower reaches N_{max} and $s \to 3$ when the shower is deep under the ground. Both X_{max} and σ can provide clues about the CR composition.

All the shower parameters for use this Gaussian-in-age parametrization were derived from a library of simulated air showers generated by the author of this thesis and described in Section 7.3.2.1.

8.1.3 Corsika Profile

It would be preferable to generate a simulated air shower initiated by the desired primary particle with desired energy and geometry each time the detector MC requests one as the input. It is not feasible however from the practical point of view. Typical statistics needed for a particular study is on the order of 10000 showers which trigger the detectors. Taking into account about 10% detector efficiency this grows to approximately 100000. It takes a few minutes to generate a shower using the Corsika simulator and a computer running at 1 GHz CPU speed. This time exceeds 1 hour per shower at energies of 10^{20} eV and above. Even simulating the observed steeply falling CR spectrum $\sim E^{-3}$, the calculational time would still be extremely long.

To overcome this limitation, we generated a library of air showers using the Corsika simulation package. The library is described in greater detail in Section 7.3.2.1.

Corsika uses the so called "thinning" algorithm to save computational time significantly at an expense of introducing greater fluctuations. The thinning is performed by assigning one particle to be the model for thousands of others and propagating only that model particle down to the critical energy. This causes significant fluctuations in the number of charged particles, especially at lower energies. To overcome this problem, we applied a special smoothing algorithm, which preserves the unique shape of the shower

and smooths out most of the fluctuations. The smoothing uses averaging of several neighboring points with a gaussian weighting function. The width of the weighting function can be adjusted to affect the influence of the neighboring points. The number of neighbors participating in the smoothing can also be adjusted. The result of this shower smoothing is shown in Figure 8.2.

A special subroutine has been developed to pick up a random shower from the library, scale it up or down to the requested energy and feed its longitudinal profile into the detector MC simulator. It is necessary to scale the shower because the library is generated at fixed energies, which are almost always different from one requested by the detector MC. The scaling is done by adjusting the position of X_{max} and recalculating the numbers of charged particles at each requested slant depth. The X_{max} scaling is taken from a study of the elongation rate, described in Section 8.8.3. The X_{max} elongation rate for the Corsika output for proton, iron and CNO using QGSJET and SIBYLL2.1 models is shown in Figure 8.3. Fitting these plots reveal the elongation rates summarized in the Table 8.1. The elongation rates are in g/cm^2 per energy decade. It should be noted, however, that there should be a more sophisticated approach to the elongation rate for gamma

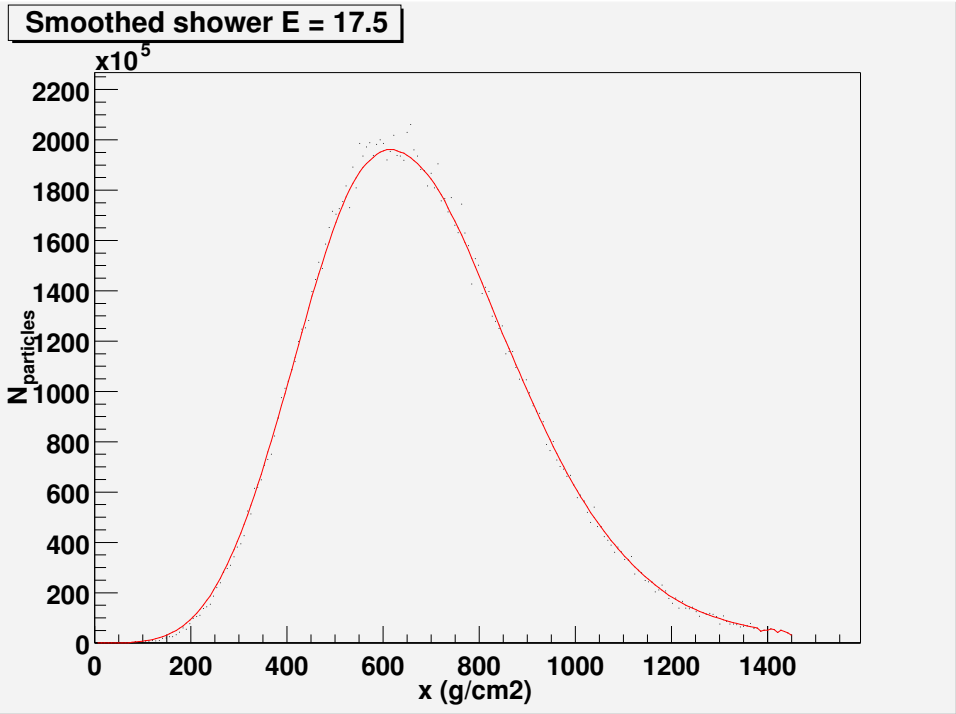

Figure 8.2. Air shower profile.

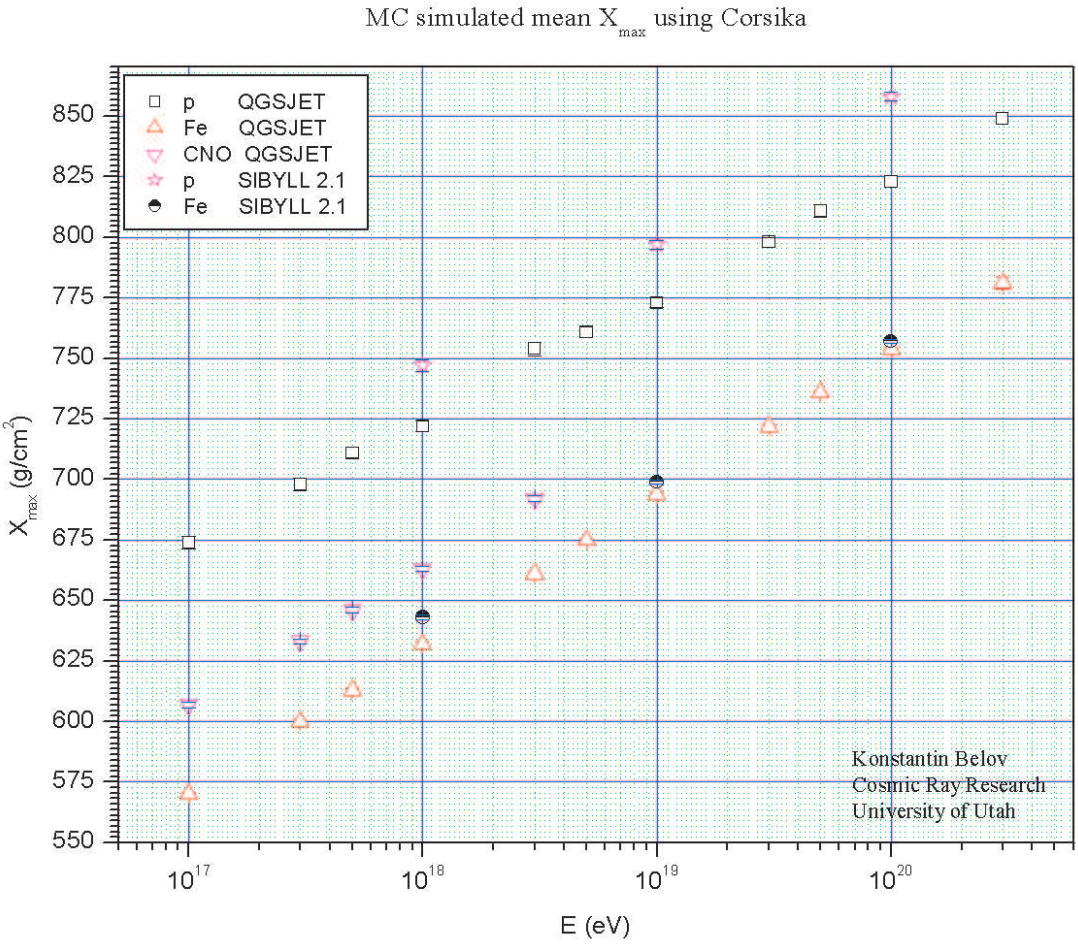

Figure 8.3. Corsika elongation rates.

Table 8.1. Corsika elongation rates.

QGSJET		SIBYLL		EGS4
p	Fe	p	Fe	γ
49.62	60.76	56.18	57.05	127.1

induced showers. Fitting it to a simple polynomial is not that accurate as for hadronic induced showers because of the Landau–Pomeranchuk–Migdal (LPM) effect, which causes the elongation rate to change at the energies higher than 5×10^{19} eV. Fortunately, it is not an issue for this study as the statistics of those events, and thus, their influence on the results, is very low.

The shower N_{max} dependance on the energy is shown in Figure 8.4 for proton and iron generated using QGSJET and SIBYLL2.1 models. N_{max} for the scaled showers are also shown on this plot.

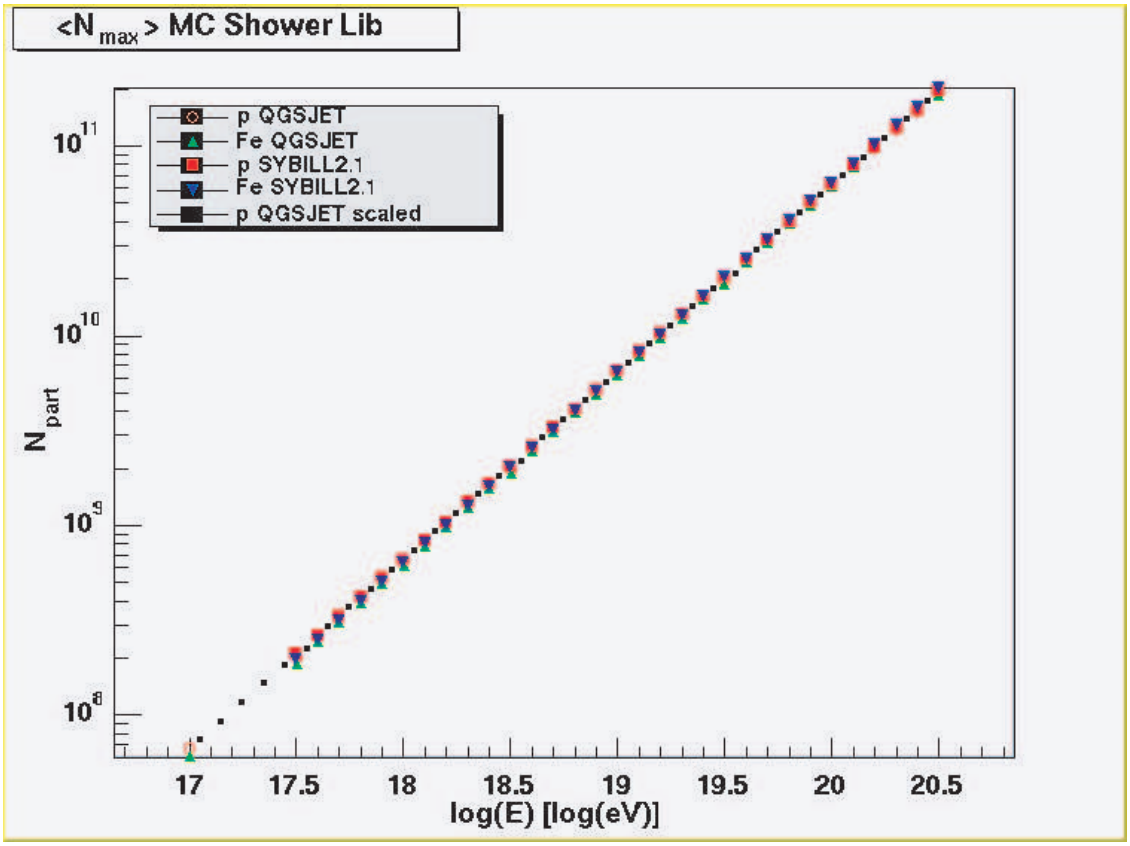

Figure 8.4. Shower N_{max} for p and Fe. .

8.2 Shower Lateral Distribution

The air shower particle density in the radial direction is approximated by the Nishimura–Kamata–Greisen (NKG) formula [89]:

$$\rho(r, X) = \frac{N(X)}{r^2} f(s, \frac{r}{r_M}), \tag{8.7}$$

where $N(X)$ is the number of charged particles as a function of the slant depth X, s is the shower age 8.6, r_M is the Moliere radius for multiple scattering and f is:

$$f(s, \frac{r}{r_M}) = (\frac{r}{r_M})^{s-2}(1 + \frac{r}{r_M})^{s-4.5} \frac{\Gamma(4.5 - s)}{2\pi\Gamma(4.5 - 2s)} \text{ [89]} \tag{8.8}$$

– the Nishimura-Kamata function.

The finite shower lateral distribution is not important for distant showers, but can introduce a significant correction for close ones.

8.3 Light Propagation in the Atmosphere

Based on the e-m profile picked, the light production and propagation in the atmosphere is modeled utilizing the same basic assumption which are used for the shower profile reconstruction described in Section 6.7. The detector MC allows us to simulate UHECR shower development and the fluorescence light propagation to the HiRes detector.

8.4 HiRes Electronics Simulation

We divide the light production into small (0.04 degree) angular bins. This helps us to model the mirror abberations and the electronics time slewing. Next the light signal from each bin is divided among the relevant photo-multiplier tubes. This is done using the ray tracing a standard table. All these steps result in the generation of a tube electronic signal profile as a function of time. Sky noise fluctuations are now added to each time bin. Since the real OMBs have an RC filter at the input, this is simulated by a special routine. After the RC filter is simulated, for the HiRes1 the signal is checked against the tube threshold, which is fixed for all tubes of the detector, unlike the real one, which is automatically adjustable. If the threshold is exceeded, the timing of the threshold crossing is recorded and the tube is tagged as triggered. For the HiRes2 the first and the confirming trigger is simulated. The pattern of triggered tubes is checked against the mirror trigger. The information about the triggered tubes is saved in HRAW1 (HiRes1) or FRAW1 (HiRes2) banks.

8.5 Simulated Detector Output

The output of the detector MC is a shower profile "as seen by the detector," with noise, imperfect optics and electronics, finite resolution and the atmospheric influence mixed in. The detector MC simulates the trigger efficiency of the real detector as well. The showers passed through the HiRes detector are then reconstructed, using the same data reconstruction routines as are used for real data processing. This multistage process helps to develop a set of "quality cuts" to select only CR events which has been well reconstructed as well as to study the HiRes detector X_{max} and energy resolution functions. Biases due to the detector trigger efficiency dependance on X_{max} can also be studied at this point.

8.6 Quality Cuts

Quality cuts are used to get rid of poorly reconstructed events. A delicate balance must be achieved between removing poorly reconstructed events and preserving statistics to do physics analysis. The quality cuts can potentially introduce a bias in the data reconstruction, so extreme care must be taken to avoid this. Quality cuts are applied at the very end after full event reconstruction is done.

An example of X_{max} distribution before any quality cuts were applied is shown in Figure 8.5.

The x axis on this plot is X_{max} in g/cm^2. An example of the X_{max} resolution with no quality cuts applied is shown in Figure 8.6. The x axis on this plot is $X_{max}^{MC} - X_{max}^{rec}$, where X_{max}^{MC} is the known value for each shower from MC input and X_{max}^{rec} is the reconstructed value.

Figure 8.7 illustrates the energy distribution before cuts. The x axis here is $\log E$ in $\log eV$. A normalized energy resolution is shown in Figure 8.8 with x axis in units of $(E_{MC} - E_{rec})/E_{MC}$. The resolution plots show that many poorly reconstructed CR events will be passed through to the final stage of the physical analysis if no effort is made to remove those events.

To develop a set of quality cuts, a set of CR events is generated by the detector MC program described in the beginning of this chapter. To achieve good statistics, the MC data set should be several times larger than the expected number of real events. The MC events are next reconstructed using the standard set of the data reconstruction routines, described in detail in Chapter 6. The same routines are used to reconstruct real CR events.

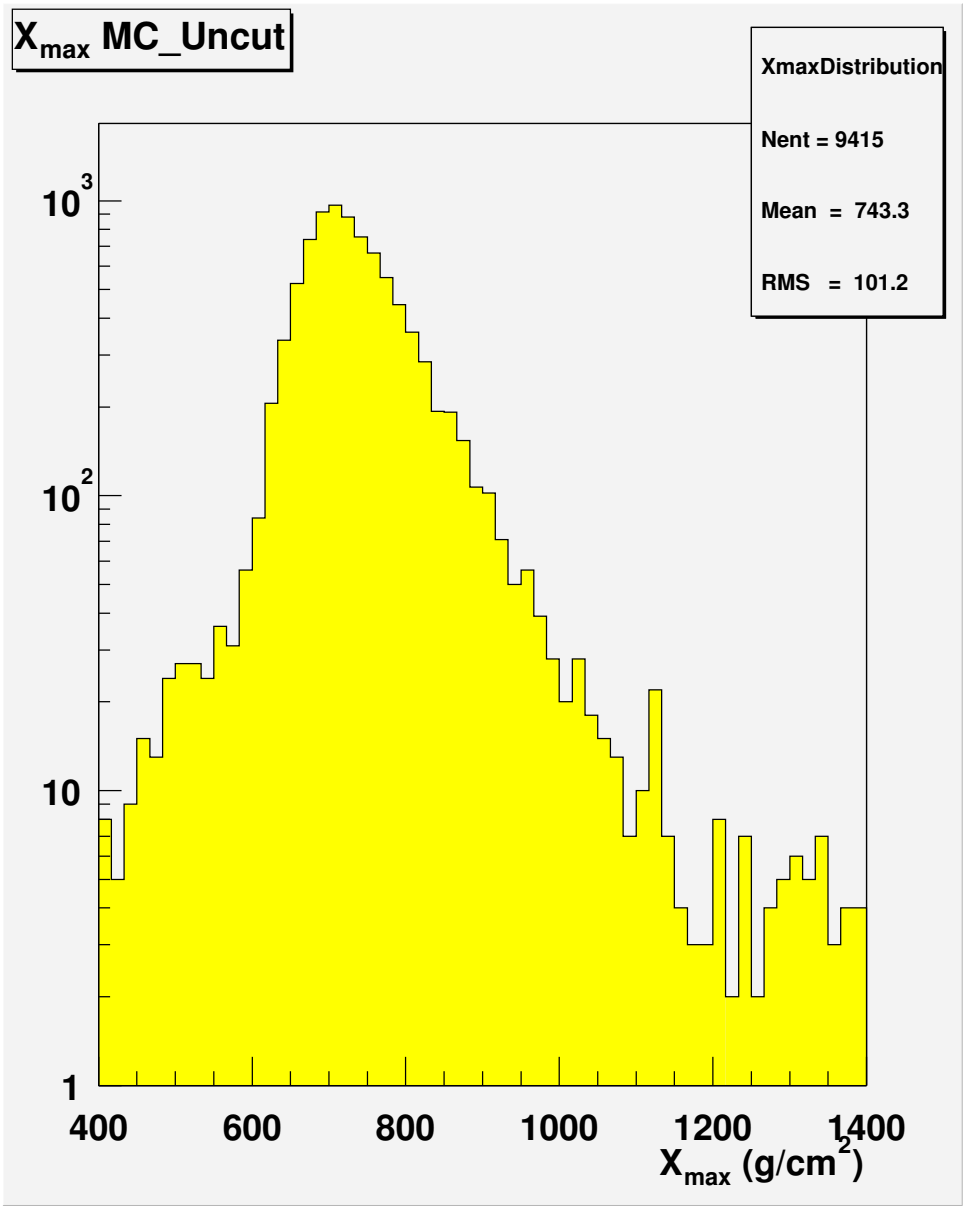

Figure 8.5. X_{max} distribution. No cuts applied.

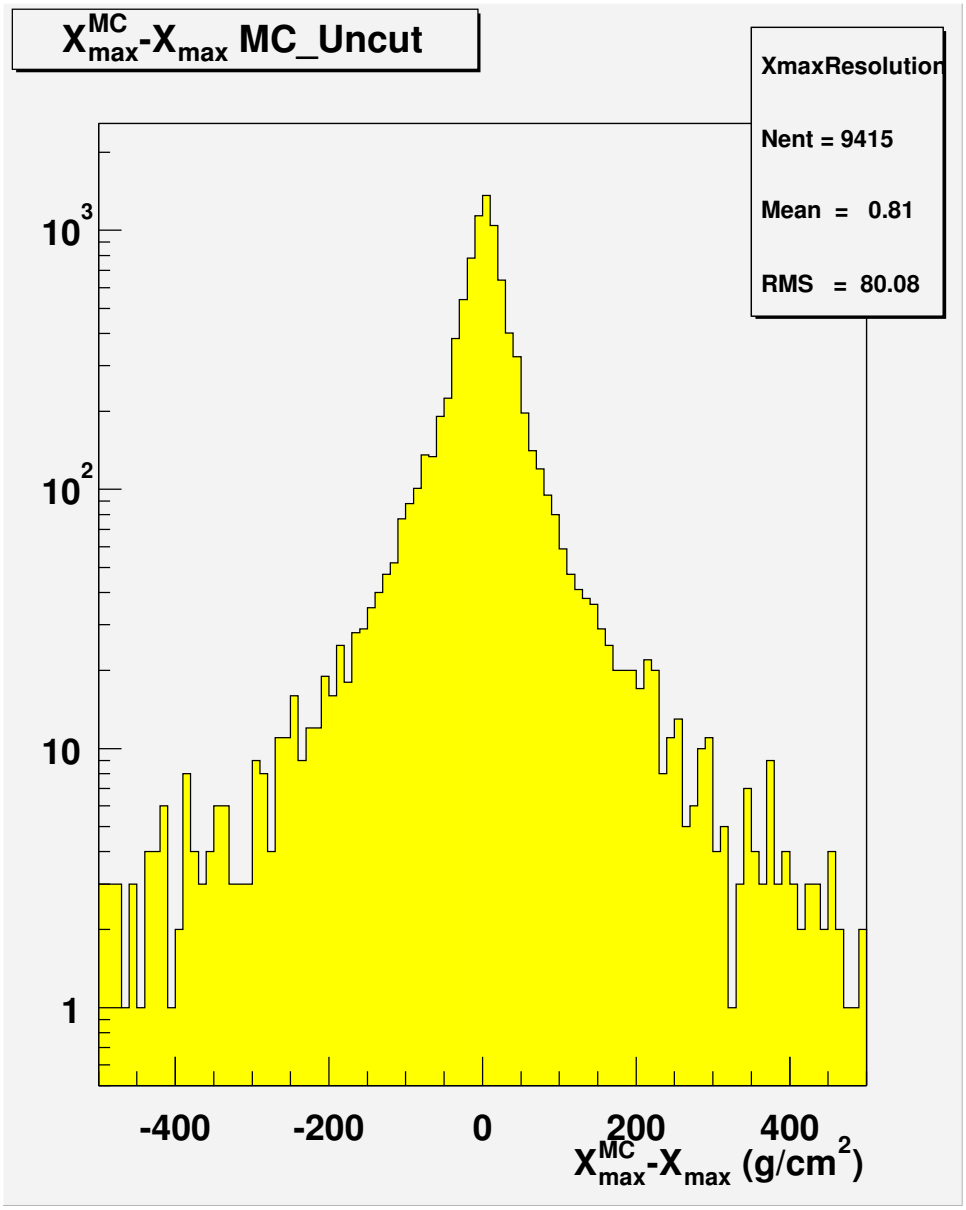

Figure 8.6. X_{max} resolution. No cuts applied.

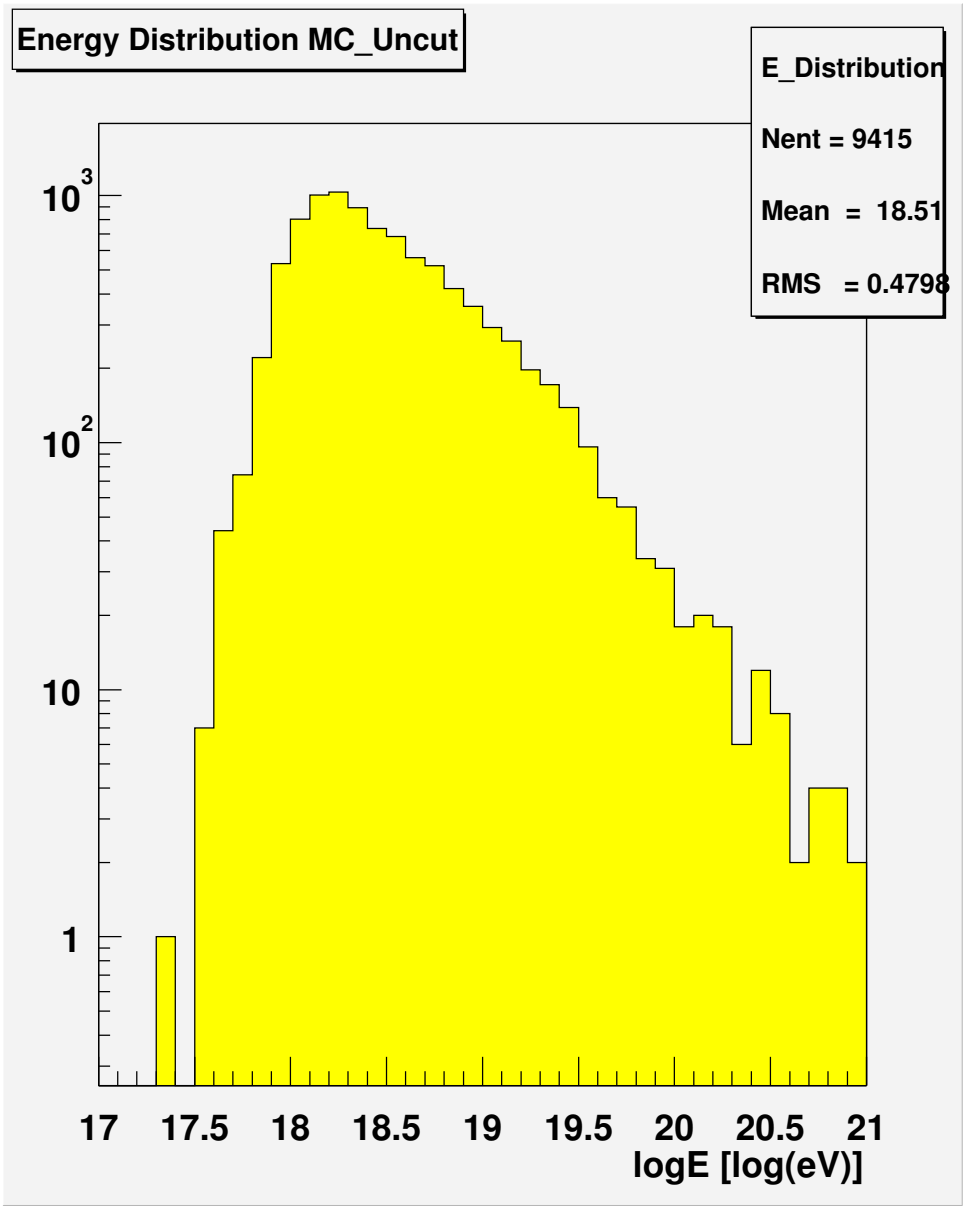

Figure 8.7. Energy distribution. No cuts applied.

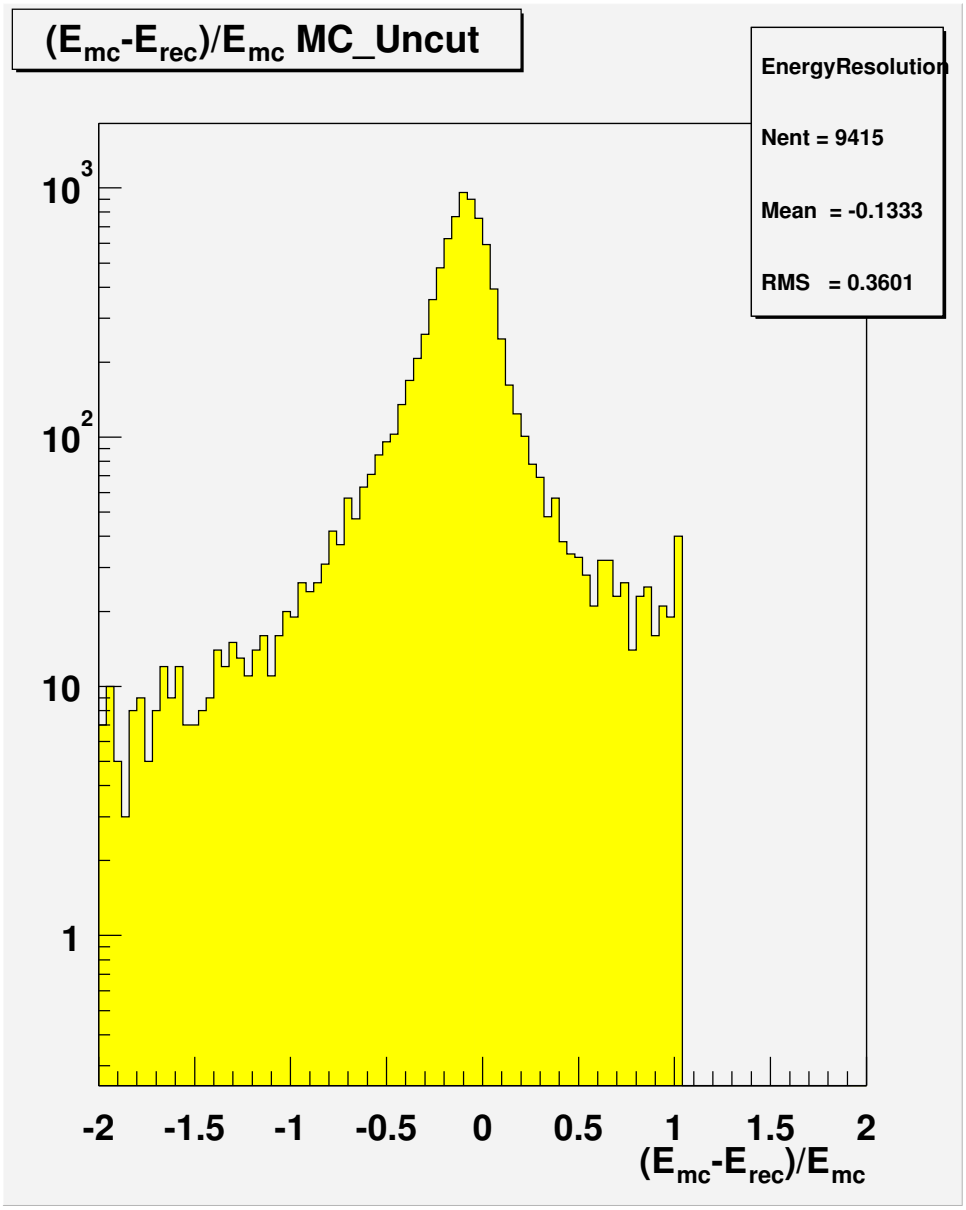

Figure 8.8. Energy resolution. No cuts applied.

Since all the parameters for any MC event are known, an event reconstructed with significantly different parameters would indicate potential problems. One can get rid of such poorly reconstructed events by applying a cut on one or several of the parameters that failed the event reconstruction.

The following parameters have been studied to establish a set of the quality cuts:

- Energy exceeding 10^{22} eV – this cuts out the events reconstructed with bogus energy.
- The shower slant depth reconstructed to be less than 200 g/cm^2 . The shower is too short to have its profile reconstructed correctly.
- The shower Zenith angle, θ, is more than 60°. These events are usually poorly reconstructed, as it was seen on a scatter plot similar to 8.9 before the cut was applied.
- The shower width in shower age, σ_s is less than 0.105 or more than 0.295. Analysis of the X_{max} resolution as a function of the shower width in shower age showed that X_{max} resolution significantly degrades if the shower width is off the above limits.
- The shower profile fit χ^2 is more than 40 or equal to zero. Zero χ^2 indicates bogus error estimation, while large χ^2 value implies a poor fit.
- The shower detector plane (SDP) opening angle is less than 10° or more than 170°. In this case, the stereo geometrical reconstruction is bad.
- Shower X_{max} reconstructed $50g/cm^2$ above the detector upper field of view (FOV) boundary. Otherwise, the shower profile will be fit incorrectly.
- $X_{max}cos\theta$ is more than 900 g/cm^2. This means that X_{max} is reconstructed deep under the ground, and thus, far away from the detector lower (FOV) boundary.
- The estimated error on X_{max} reconstruction, ΔX_{max}, exceeds 25 g/cm^2.
- The normalized error in energy reconstruction, $\frac{\Delta E}{E}$ is more than 0.063.
- A loose bracket cut. Reconstructed X_{max} should be within 200 g/cm^2 from the detector field of view boundary.

A decision to apply a particular cut is based on a correlation between the accuracy in reconstructing the major shower parameters, X_{max} and energy, and the parameter in question.

The following figures illustrate the reasons for certain cuts. Figure 8.9 shows the X_{max} resolution as a function of the zenith angle θ. The x-axis here is θ in radians. The y-axis is $X_{max}^{MC} - X_{max}^{rec}$, the X_{max} resolution.

Figure 8.10 shows the X_{max} resolution as a function of the estimated X_{max} reconstruction error, ΔX_{max}.

The X_{max} resolution as a function of:

- the shower width in age is shown in the Figure 8.11;
- the plane opening angle is shown in the Figure 8.12;
- the shower slant depth is shown in the Figure 8.13;
- the shower plane fit χ^2 is shown in the Figure 8.14.

Similar plots were made for all the shower parameters in question. Figures 8.15, 8.16, 8.17 and 8.17 demonstrate the result of applying the quality cuts mentioned above. Comparison with plot in Figures 8.5, 8.6, 8.7 and 8.7 shows significant reductions of the tails in the distributions.

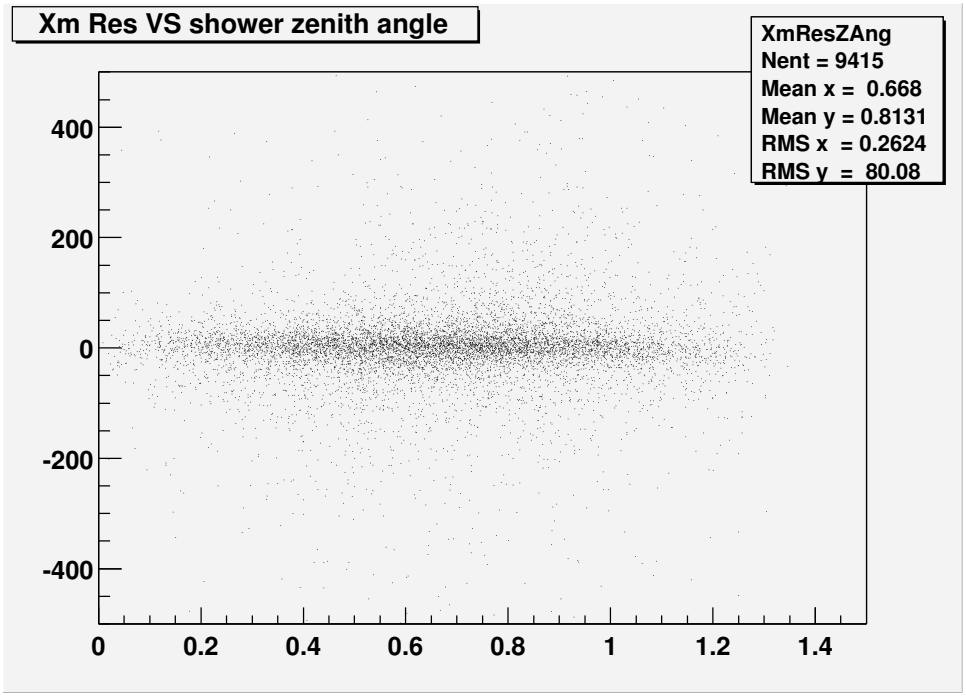

Figure 8.9. X_{max} resolution vs zenith angle.

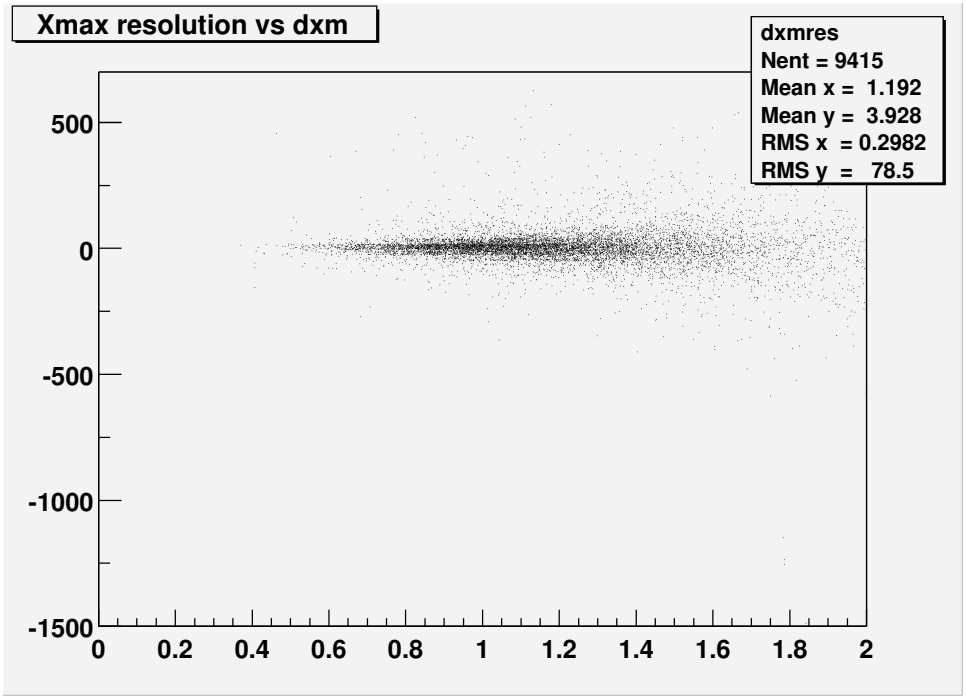

Figure 8.10. X_{max} resolution vs ΔX_{max}.

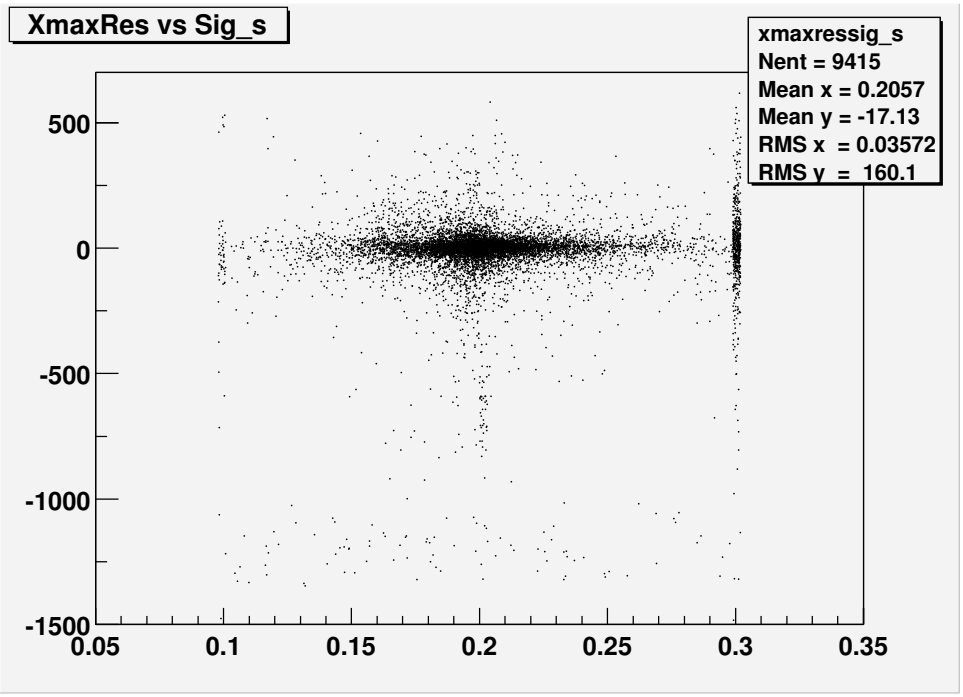

Figure 8.11. X_{max} resolution vs σ_s.

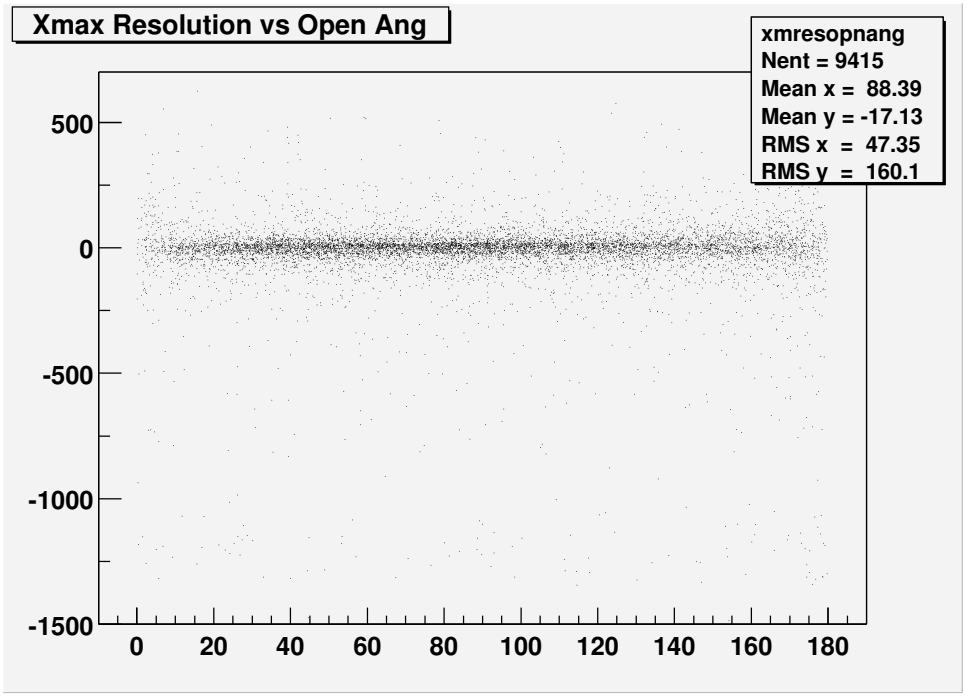

Figure 8.12. X_{max} resolution vs plane open angle.

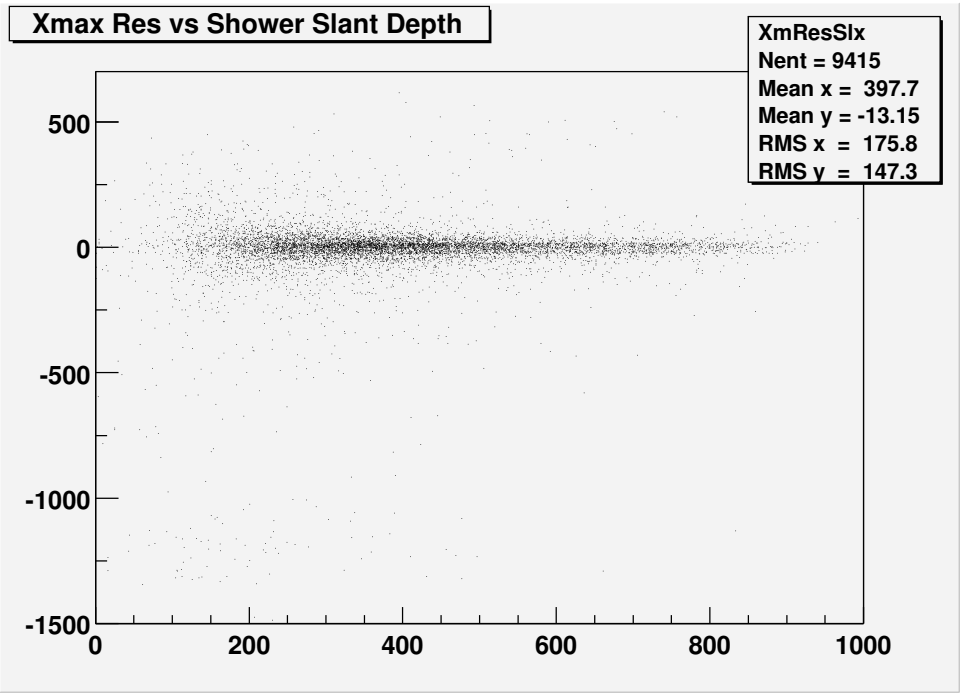

Figure 8.13. X_{max} resolution vs shower slant depth.

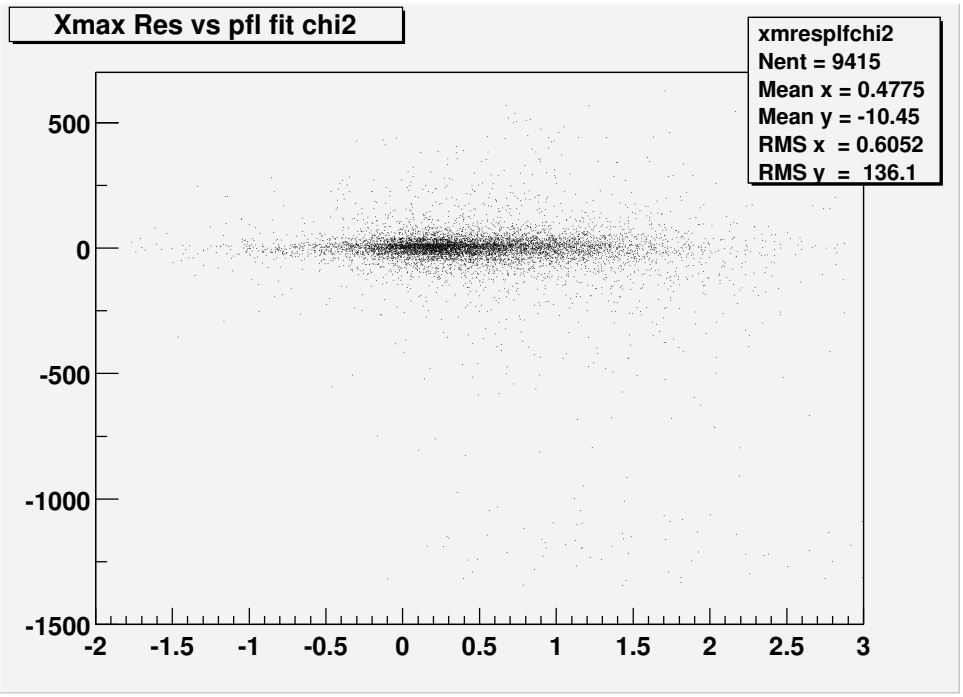

Figure 8.14. X_{max} resolution vs plane fit χ^2.

8.7 Detector Resolution Function

The resolution plots in Figures 8.16 and 8.18 provide the detector X_{max} and energy resolution functions. As can be seen in Figure 8.16 the detector X_{max} resolution is about 27 g/cm^2 with asystematic shift of the mean on the order of 2 g/cm^2. The achieved energy resolution is about 12% (see Figure 8.18). The reader should be warned, however, that very little effort has been made to preserve the true energy spectrum as this was not the primary goal of this work. In order to claim that shown energy distribution is indeed the CR energy spectrum, one should check for bias, possibly introduced at any stage of the data processing. This lies outside of this dissertation. Steps that has been taken in order to check that no significant bias was introduced to the X_{max} distribution are discussed in the next section.

8.8 Bias Study

A series of tests have been performed to check that no biases have been introduced to the X_{max} distribution during all stages of the data processing.

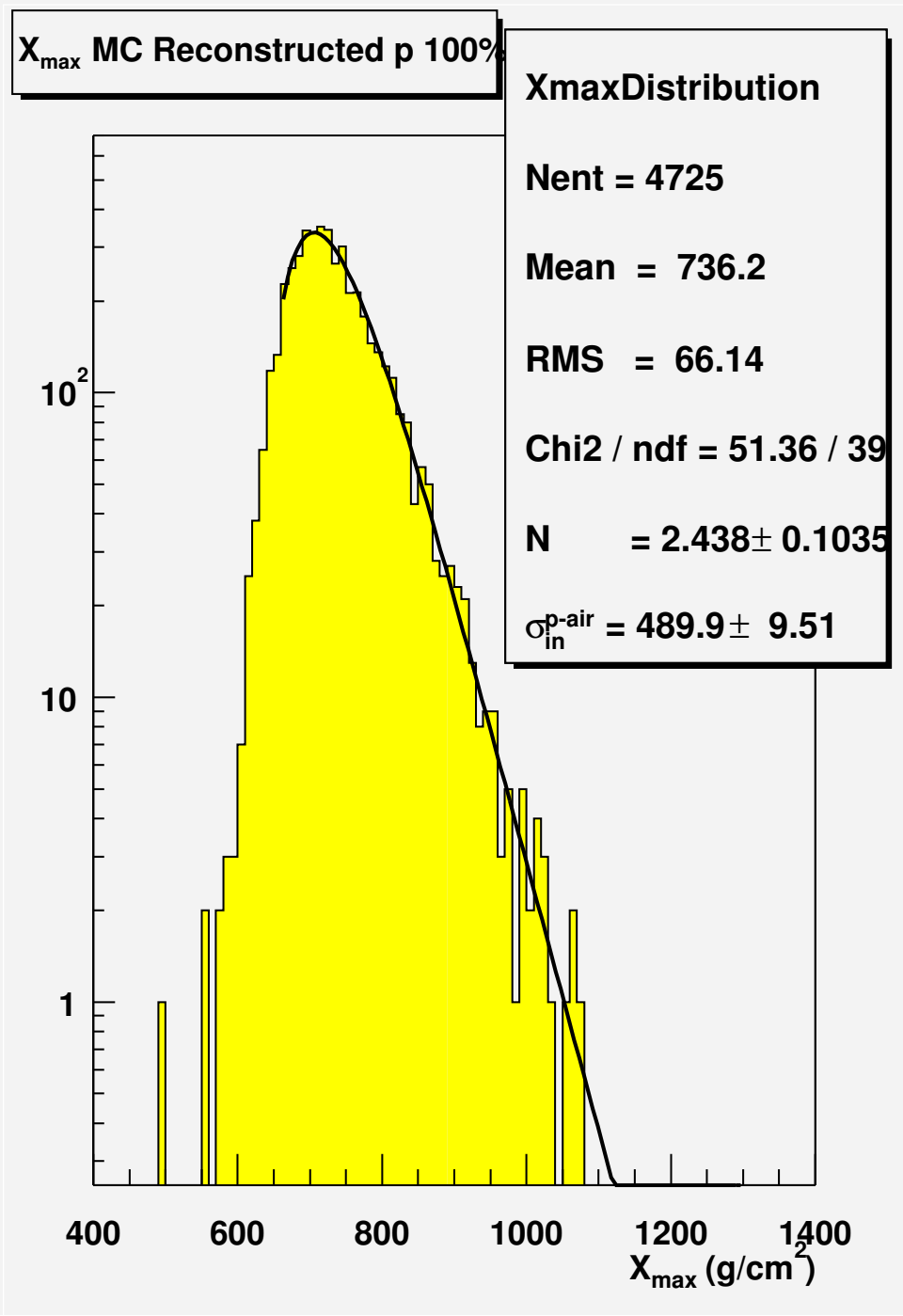

Figure 8.15. X_{max} distribution. After quality cuts.

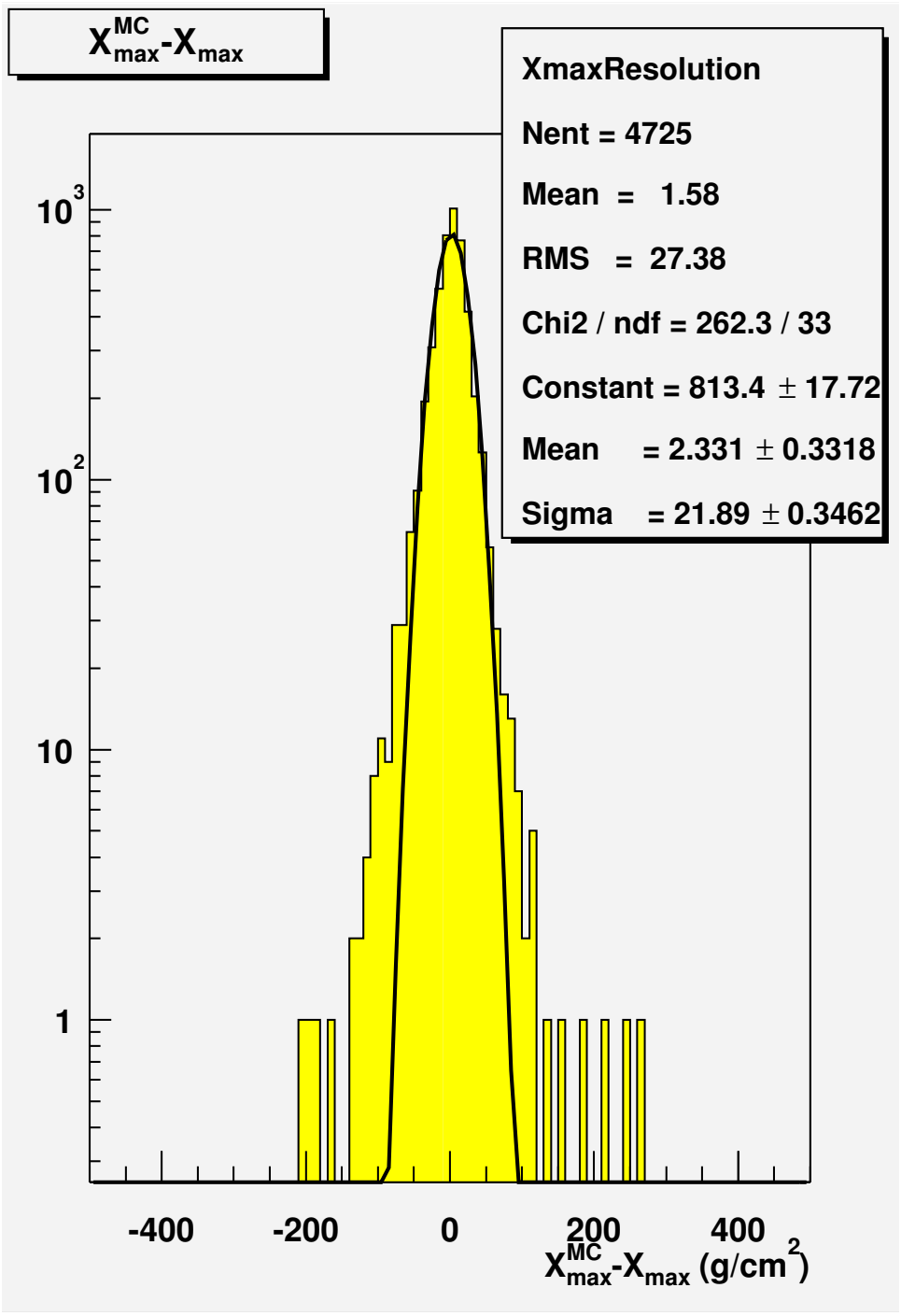

Figure 8.16. X_{max} resolution. After quality cuts.

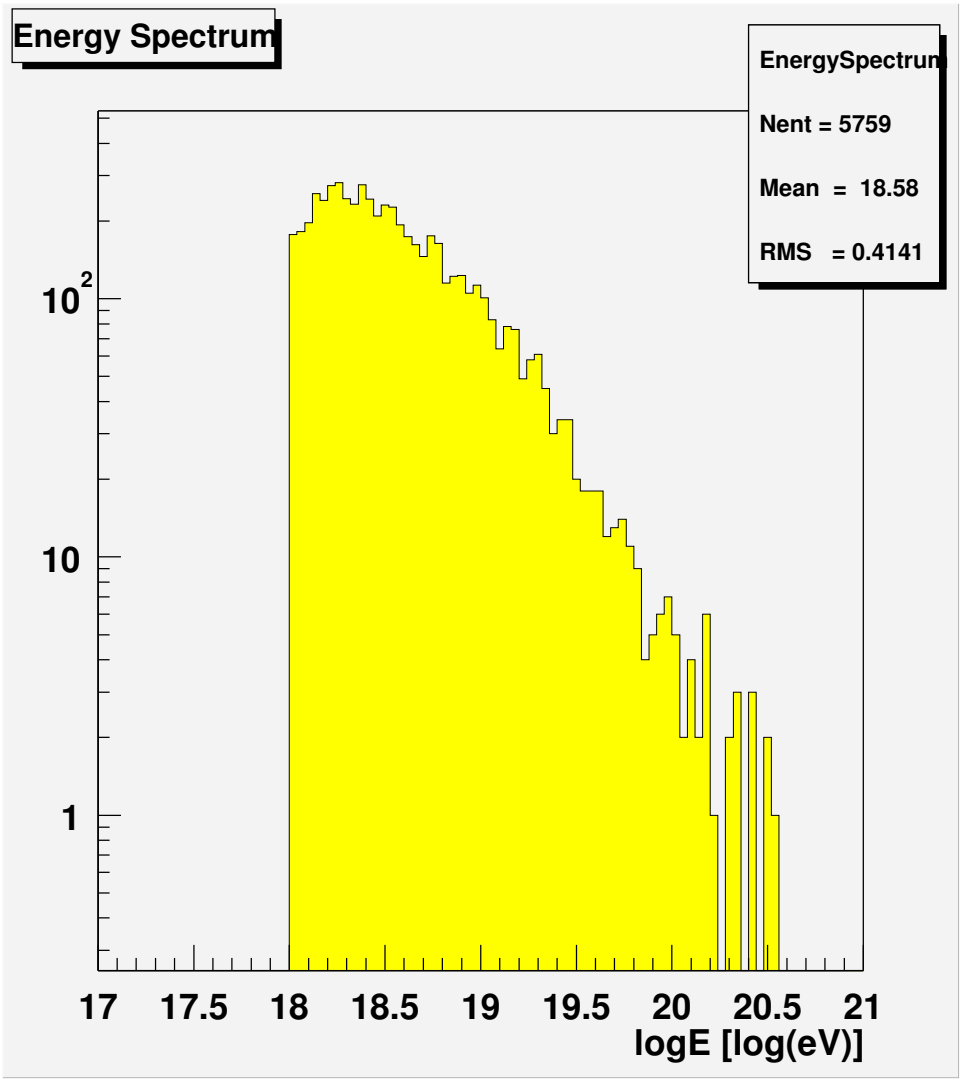

Figure 8.17. Energy distribution. After quality cuts.

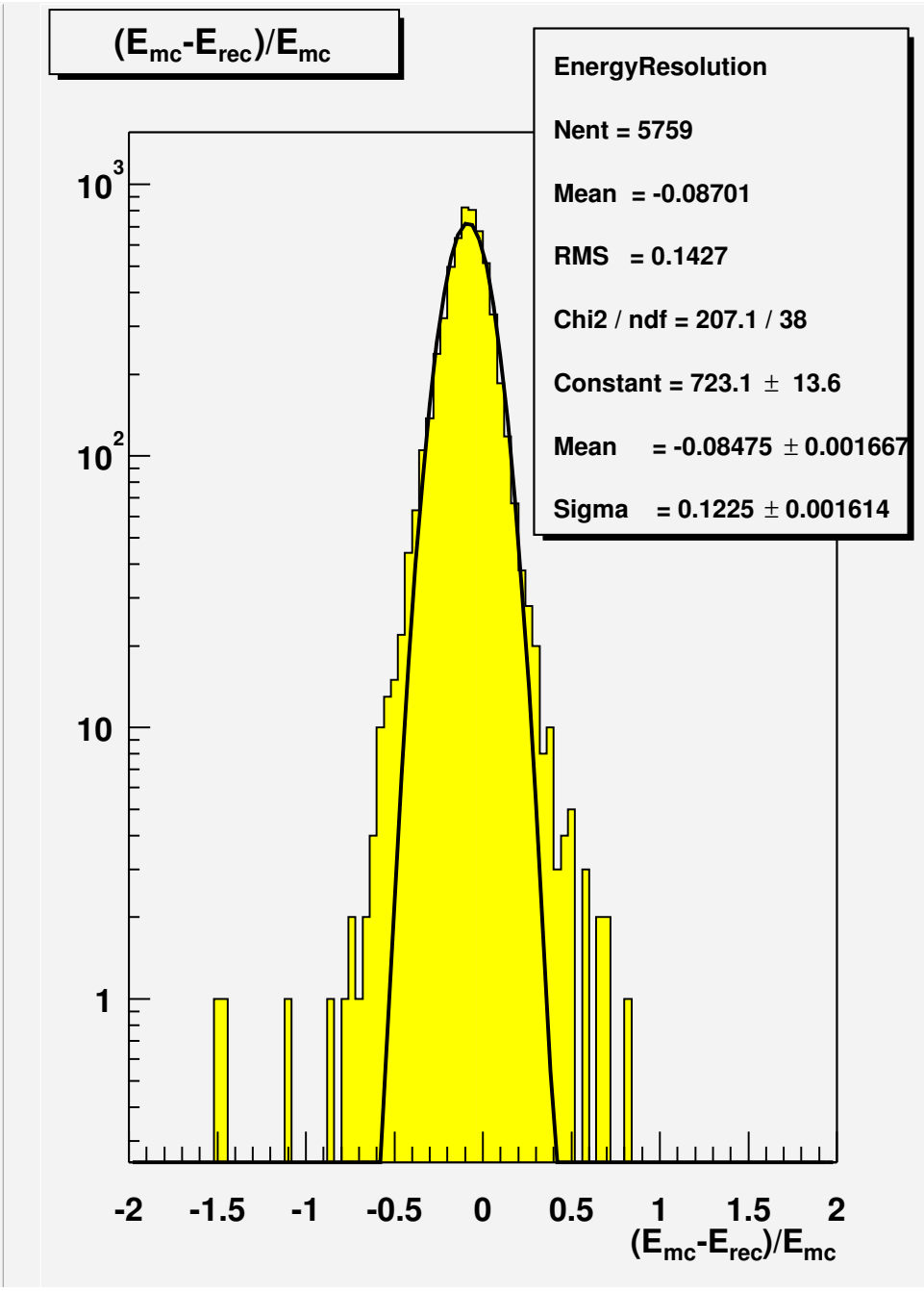

Figure 8.18. Energy resolution. After quality cuts.

8.8.1 X_{max} Aperture Dependance

Because of the geometrical restrictions of the HiRes detector field of view, it can trigger less effectively on the CR events that develop earlier in the atmosphere and thus have smaller X_{max}. The detector efficiency is the number of CR events which did trigger the detector within an X_{max} bin divided by the total number of CR events thrown by a MC simulation into the same X_{max} bin. The HiRes trigger efficiency as a function of X_{max} is shown in Figure 8.19. The figure illustrates that indeed, the HiRes detector is less efficient at shallower X_{max} and this dependance should be taken into account if one is going to use events with X_{max} less than $700 g/cm^2$. For the cross-section study we use a deeper portion of the X_{max} distribution to avoid heavier nuclei contamination, (see Section 8.8.5). This insures a negligible influence of the HiRes X_{max} trigger bias on the cross-section measurement.

8.8.2 X_{max} Resolution Mean and RMS

A significant shift of the X_{max} resolution mean value or its RMS would indicate yet another potential bias problem. We divide our MC data set into eight energy bins. For each bin we create an X_{max} resolution distribution to find its mean value and RMS. The

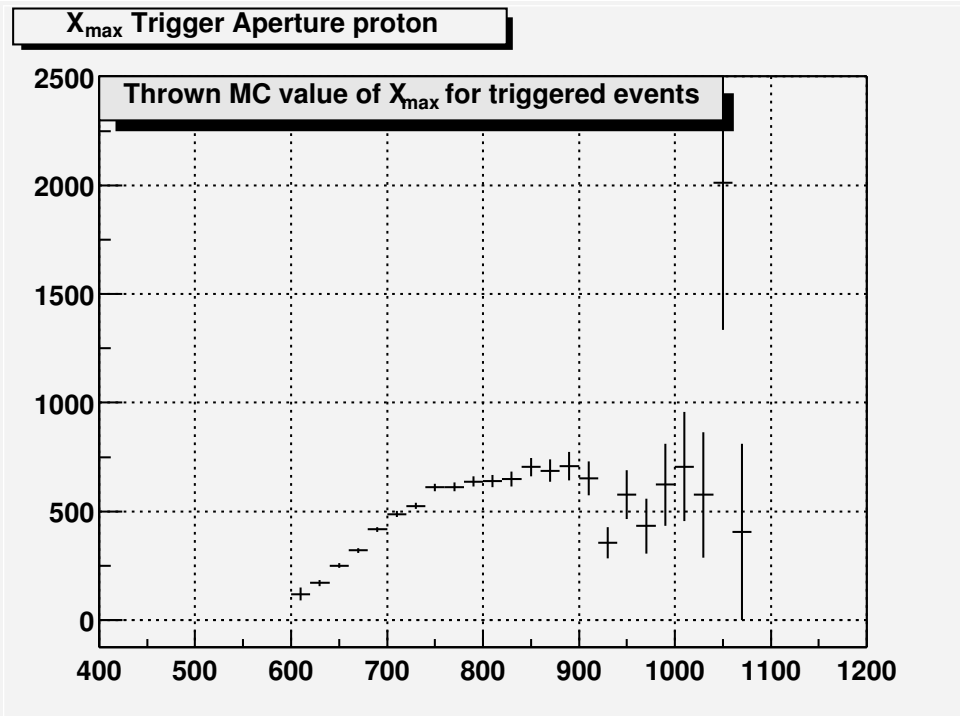

Figure 8.19. X_{max} aperture dependance.

results are shown in Figure 8.20. The RMS of these distributions shows no shift with energy. The minor shift in the mean value is much less than the detector X_{max} resolution, and can be safely ignored as such.

8.8.3 Elongation Rate Check

The purpose of this check is to verify that the detector triggering and the data reconstruction do not introduce any significant change into $< X_{max} >$ dependance on energy, the elongation rate. This is best done by comparing the elongation rate from the air shower simulation program with the elongation rate after all those showers go through the detector response simulation, with all reconstruction stages and the quality cuts. These graphs are shown in Figure 8.21 for proton (the upper set of the data points) and iron (the lower set of the data points) primaries. The minor elongation rate change is well within the statistical errors and can be safely ignored.

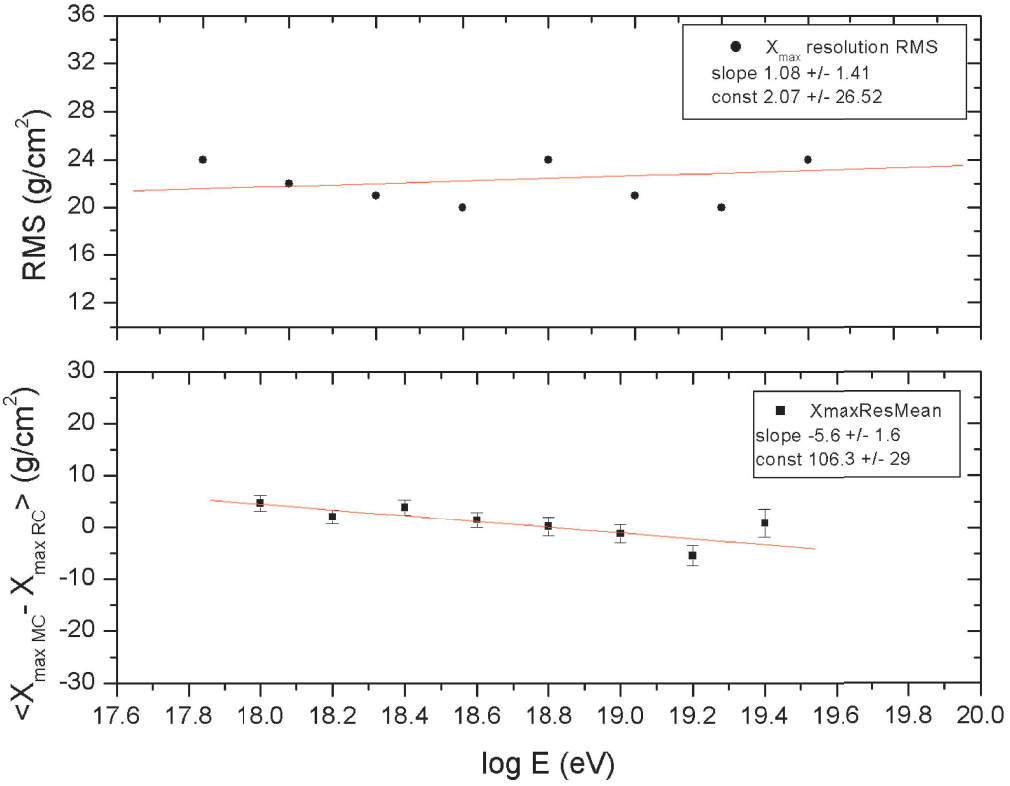

Figure 8.20. X_{max} resolution function vs energy.

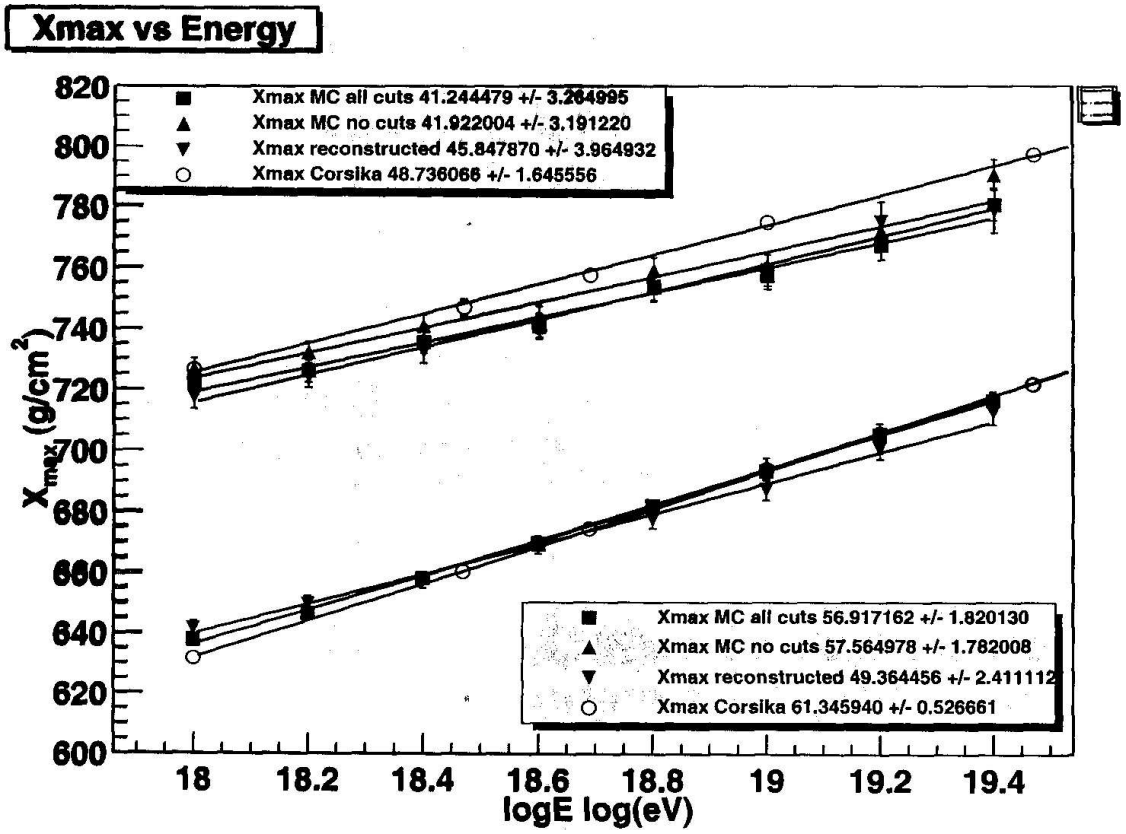

Figure 8.21. X_{max} elongation rate.

8.8.4 Data Pull

For the events where $< X_{max} >$ is reconstructed by both detectors, it is possible to check if the following reconstructed distribution is centered around zero:

$$P = \frac{X^1_{max} - X^2_{max}}{(X^1_{max} + X^2_{max})/2}, \tag{8.9}$$

where X^1_{max} and X^2_{max} are the X_{max} values reconstructed by HiRes1 and HiRes2 correspondingly.

Eq. 8.9 is usually referred to as a data pull. Any significant deviation of the 8.9 distribution mean value from zero or a significantly scewed distribution would indicate a potential bias problem.

The data pull for the MC simulated events is shown in Figures 8.22.

The data pull shown in Fig. 8.22 is well centered and symmetrical. This indicates the absence of a potential bias.

In conclusion to this section, we can say that no significant bias was found to be introduced by the HiRes detector, the data reconstruction procedure or the quality cuts.

8.8.5 The Heavier Nuclei Contamination

A Hires previous study [51] indicated that heavier nuclei can contribute up to about 20% into CR composition at the highest observed energies. Figure 8.23 shows Corsika simulated X_{max} distributions:

- proton - solid line;
- CNO - dotted line. 20% of the proton events;
- Fe - dashed line. 20% of the proton events.

The heavier nuclei influence can be minimized if a deeper portion of the X_{max} distribution is used. A $740 g/cm^2$ cut off point has been chosen for this study. The deconvolution technique makes the value of the cut off point to have very little influence on the fitting result, so it is safe to use a portion of the X_{max} distribution deeper than $740 g/cm^2$.

It should be noted that the technique, proposed in Chapter 7 can be used for a CR composition study independently from the mean X_{max} method used in [51]. Indeed, assuming a strong interaction model, QGSJet or SIBYLL2.1 for example, it is possible to search for the best fit of the X_{max} distribution by the convolution function 7.7 varying the CR composition. In this case, the exponential index (see Section 7.3.2.2) should be

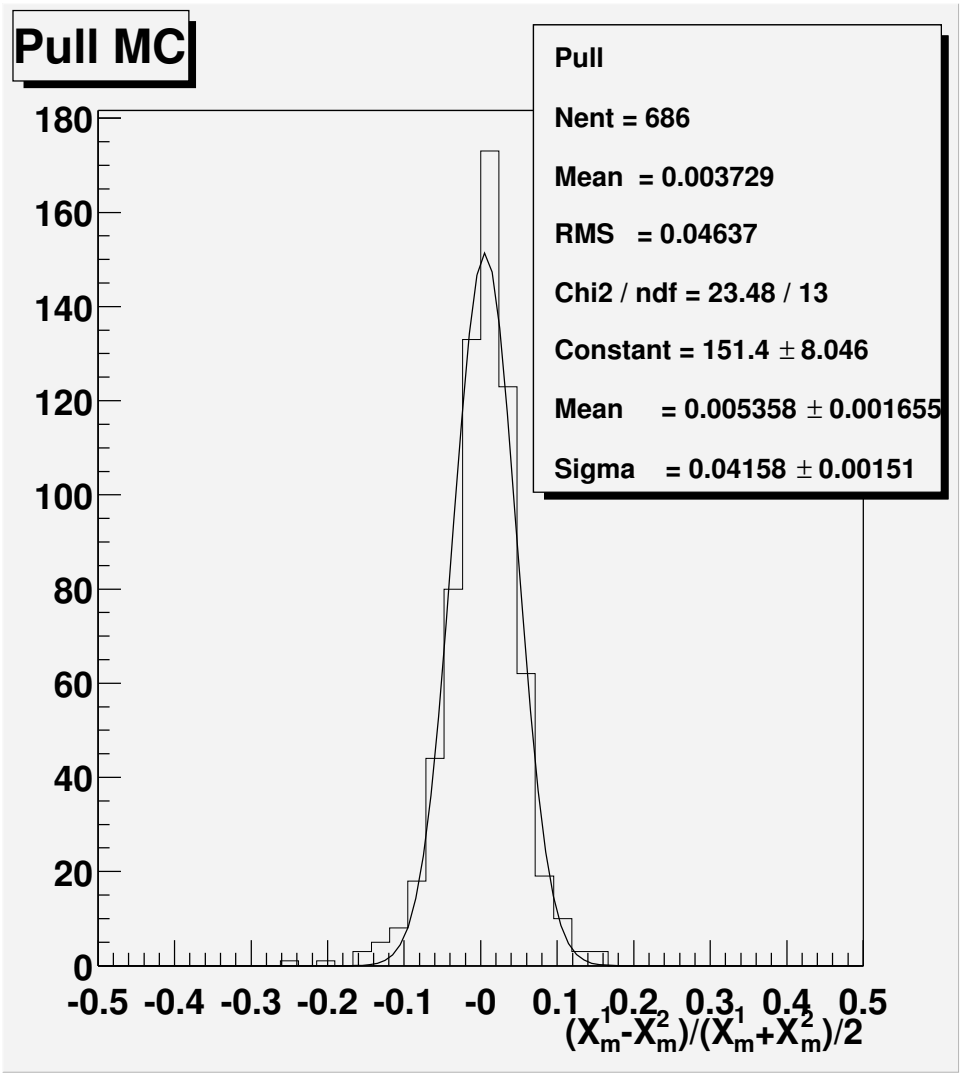

Figure 8.22. Data pull. MC.

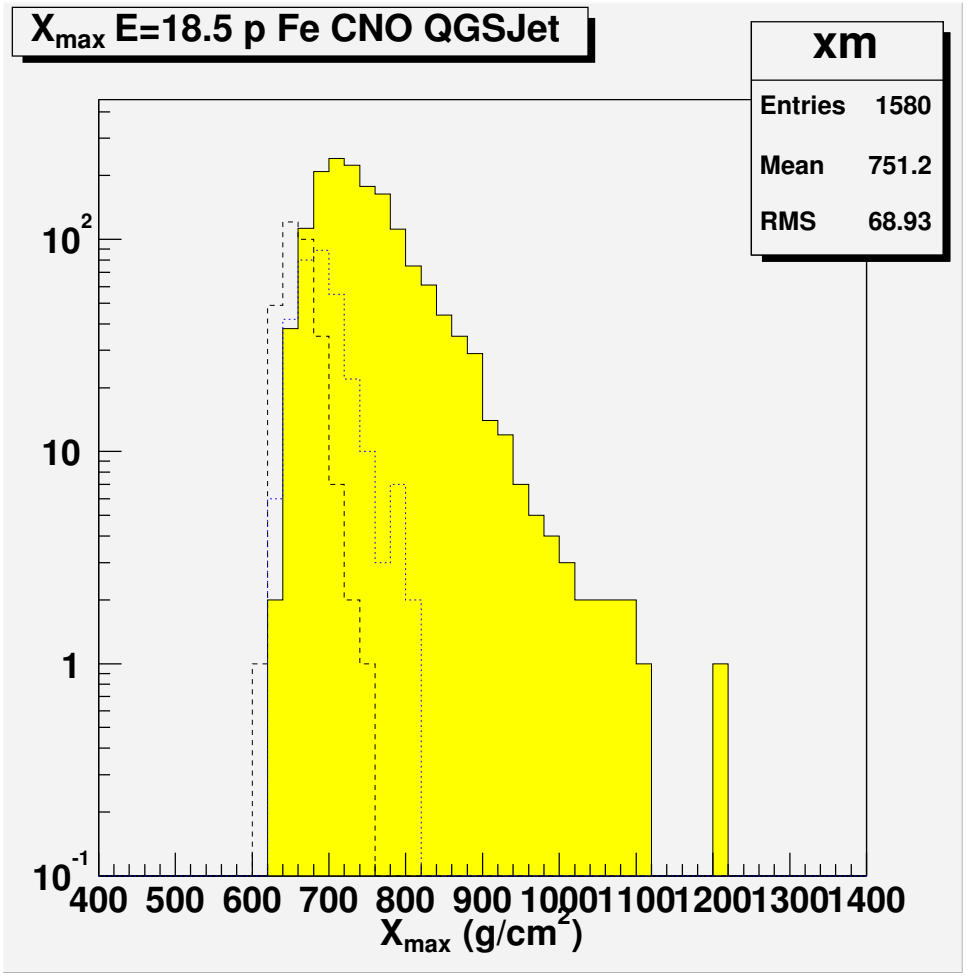

Figure 8.23. X_{max} distribution for proton, CNO and Fe.

replaced with two indexes, for proton and iron, respectively. A combined "mean X_{max}" and "deconvolution" study can reduce systematic uncertainties in the CR composition measurements.

8.8.6 Gamma Ray Contamination Influence

Potential gamma ray contamination poses a bigger challenge than the heavier nuclei contamination because gamma ray induced air showers can not be simply cut from the X_{max} distribution. Gamma ray induced showers tend to develop deeper in the atmosphere than the proton induced ones. This results in a tail at the deeper portion of the X_{max} distribution. We can safely neglect the gamma ray influence if there is only a small number of the CR events induced by gamma rays contributing into the X_{max} distribution. This is because a small number of CR events at the tail of the X_{max} distribution has little effect on the fitting result. This effect is already included into the systematic error. If, however, the gamma ray flux is significant at around $10^{18.5}$ eV, the gamma ray influence must be taken into account.

A study to estimate the systematic error that can be potentially introduced into the σ^{inel}_{p-air} measurement was done. It should be noted that this study is only a preliminary estimation of the potential systematic error due to gamma ray flux. A more precise approach should include a gamma ray flux measurement, which can be done using the proposed technique (see Chapter 7).

Indeed, as in the case of heavier nuclei, the X_{max} distribution can be fit by the convolution equation (7.7), taking into account that the exponential component due to the point of first interaction will have two indexes instead of one due to the protonic component and due to the gamma component of the CR flux. Assuming the gamma ray cross-section to be known from a model, one can vary the gamma ray flux until the best fit of the X_{max} distribution is achieved. This gamma ray flux measurement is not only interesting by itself, but also allows us to estimate correctly the systematic error of the σ^{inel}_{p-air} measurement due to gamma ray contamination.

To estimate a potential systematic error due to the gamma ray flux, sets of MC simulated events have been used. About 12000 proton induced simulated air showers (in E^{-3} spectrum) were sequentially "contaminated" by gamma ray induced showers. The contamination ranges from 0 to 20% in 1% steps below 5% contamination and 5% steps above 5% contamination. A cross-section was measured for each data set using the deconvolution method. The measured cross-section as a function of gamma ray

contamination is shown in Figure 8.24. The upper and lower curve are the upper and lower statistical error limits. This study is applied to the final systematic error calculation described in Chapter 9.

It should be noted that the HiRes data are inconsistent with the gamma ray flux exceeding 5%. This value has been used to estimate the σ^{inel}_{p-air} measurement systematic error due to gamma ray flux.

A simultaneous mass composition/cross-section study using the deconvolution technique is not limited to the gamma ray flux study. The component of heavier nuclei flux in conjunction with the proton cross-section can be measured as well by the proposed deconvolution method.

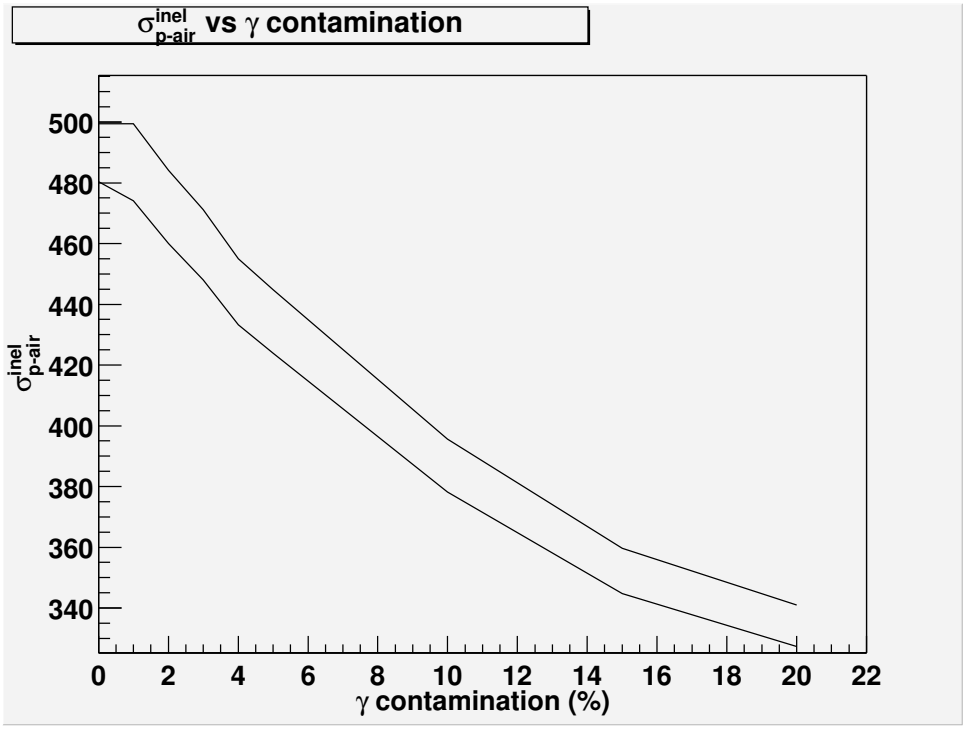

Figure 8.24. Cross-section vs gamma contamination.

CHAPTER 9

PHYSICS RESULTS

9.1 Data Set

CR events that trigger both HiRes detectors within $200\mu s$ time window become stereo candidates and are placed in a special data file. They undergo a reconstruction attempt. The same routines that are used for the Detector MC study are used for the real event reconstruction. The reconstructed events are then selected using the following criteria:

- the event must be observed during clear weather conditions (see Section 5.4.2);
- the event profile must be reconstructed by at least one of the detectors.

There are 3356 events collected from January 2000 to March 2003 that pass these selection criteria. A set of quality cuts discussed in Section 8.6 is applied next. It should be noted that it is the same set of the quality cuts that are used for the detector MC study. 1348 out of 3356 CR events pass the quality cuts. These 1348 stereo CR events are our data set.

9.2 Energy Distribution

The energy distribution for the data set is shown in Figure 9.1. Note that the energy distribution shown in Figure 9.1 should not be associated with the CR spectrum at the energies above 10^{18} eV. The set of the quality cuts (see Section 8.6) is designed to remove poorly reconstructed CR events while introducing no bias into the X_{max} distribution, which is important for this cross-section study. This does not guarantee the absence of a bias towards the energy distribution. A CR spectrum study requires a separate analysis, which is not the goal of this work. We should only conclude that the energy distribution of the data set is similar to the observed CR spectrum (see Section 3.3) and that the mean energy for the data set is $10^{18.52}$ eV.

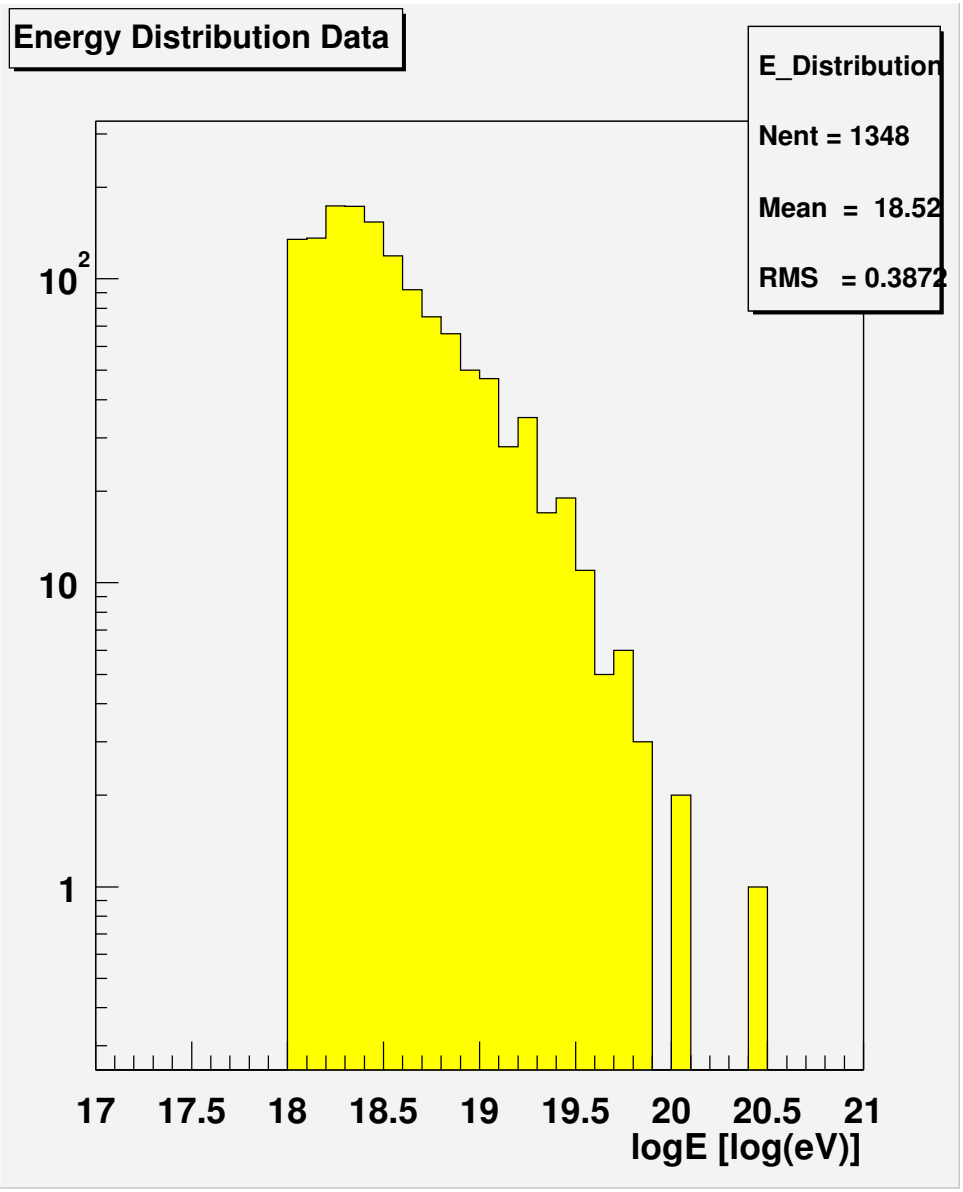

Figure 9.1. Energy distribution for the selected CR events.

9.3 X_{max} Distribution. σ^{inel}_{p-air} at $10^{18.5}$ eV

The X_{max} distribution for the selected 1348 events is shown in Figure 9.2. Applying the deconvolution technique discussed in Chapter 7 yields a value of the p-air inelastic cross-section of $456 \pm 17(stat)$ mb at $10^{18.5}$ eV. A fit of the convolution function 7.7 is also shown on the figure.

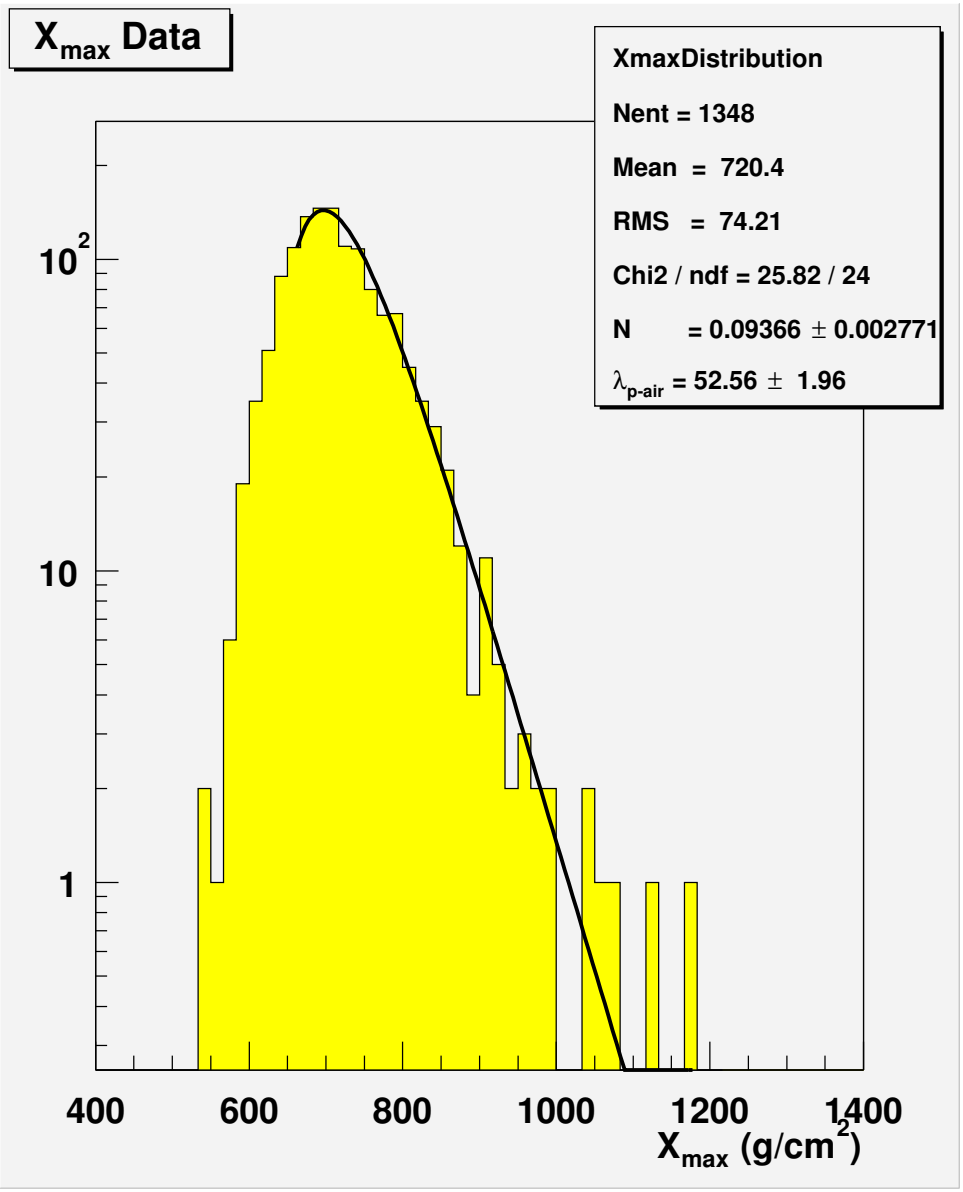

Figure 9.2. X_{max} distribution for the selected CR events.

9.4 Systematic Error Analysis

In order to evaluate the σ_{p-air}^{inel} systematic uncertainty potential sources for systematic errors were checked, including the following:

- the strong interaction model dependence;
- the influence of atmospheric conditions;
- the heavy nucleus contamination;
- the influence of gamma contamination;
- the detector X_{max} trigger bias;
- the reconstruction and quality cuts bias;
- the fitting bias;
- the X_{max} distribution tail influence.

All of the systematic error and bias analysis done with MC simulations is described in detail in Chapter 8. Only analysis applicable to the CR data or skipped in Chapter 8 will be discussed below.

9.4.1 Strong Interactions Model Dependance

After the first few interactions, the primary particle energy is reduced down to energies, which can be achieved by modern accelerators. This lower energy region is extensively studied. All strong interaction models, including QGSJet and SIBYLL2.1, agree very well with accelerator data and with each other in this energy region. The influence of the strong interaction model on the air shower fluctuations in the atmosphere, where secondary particle energies are much lower than the energy of the primary particle, is minimal (see Section 7.3.2.3). There should be negligible model dependance on our cross-section measurement and the corresponding systematic error can be safely ignored.

9.4.2 The Influence of Atmospheric Conditions

In order to reduce the influence of the atmosphere on the result, the data collected during poor weather conditions have been cut (see section 9.1). The weather code (see Section 5.4.2.5), as well as the operator log, have been used for this selection. This insures minimal distortion of the result due to changing atmospheric conditions. It

should be noted that, on average, clouds and fluctuating horizontal attenuation length and vertical scale height can potentially lead to the broadening of the X_{max} resolution function contributing to a systematic error, but should not change the measured value. This is true as long as the X_{max} resolution function is gaussian and centered at zero and average atmospheric parameters are known very well. As shown in Chapter 8, the achieved X_{max} resolution function satisfies the above criteria. Many HiRes publications demonstrated that the Utah desert atmosphere around the HiRes detector is known very well and atmospheric fluctuations are minimal. Due to the above mentioned factors, the atmospheric influence on the measured cross-section value can be safely ignored.

9.4.3 Data Pull

The same data pull analysis that was done for the Monte Carlo simulated events and discussed in Section 8.8.4 is done for the CR events. The data pull distribution for the CR events is shown in Figure 9.3.

One hundred and thirty of the real CR events are reconstructed by both detectors well enough to pass all quality cuts. A symmetrical data pull with a negligible shift of the mean does not indicate any significant bias in X_{max} reconstruction by both detectors, which must be taken into account.

9.4.4 Gamma Ray Contamination Influence

The gamma ray contamination influence is discussed in details in section 8.8.6. Here we show the same plot as Figure 8.24, but with the measured cross-section value (see Figure 9.4) to demonstrate the error envelope for the cross-section measurement produced by a possible gamma ray flux contamination. The possible gamma ray flux introduces an asymmetrical systematic error in the cross-section measurement, which is reflected in the final result.

9.5 Systematic Error Balance

The final systematic error budget for λ_{p-air} composed of:

- possible gamma ray contamination $< 4g/cm^2$, (assuming $< 5\%\gamma$ ray flux);
- reconstruction and quality cut bias $< 1.5g/cm^2$;
- fitting bias $< 1g/cm^2$.

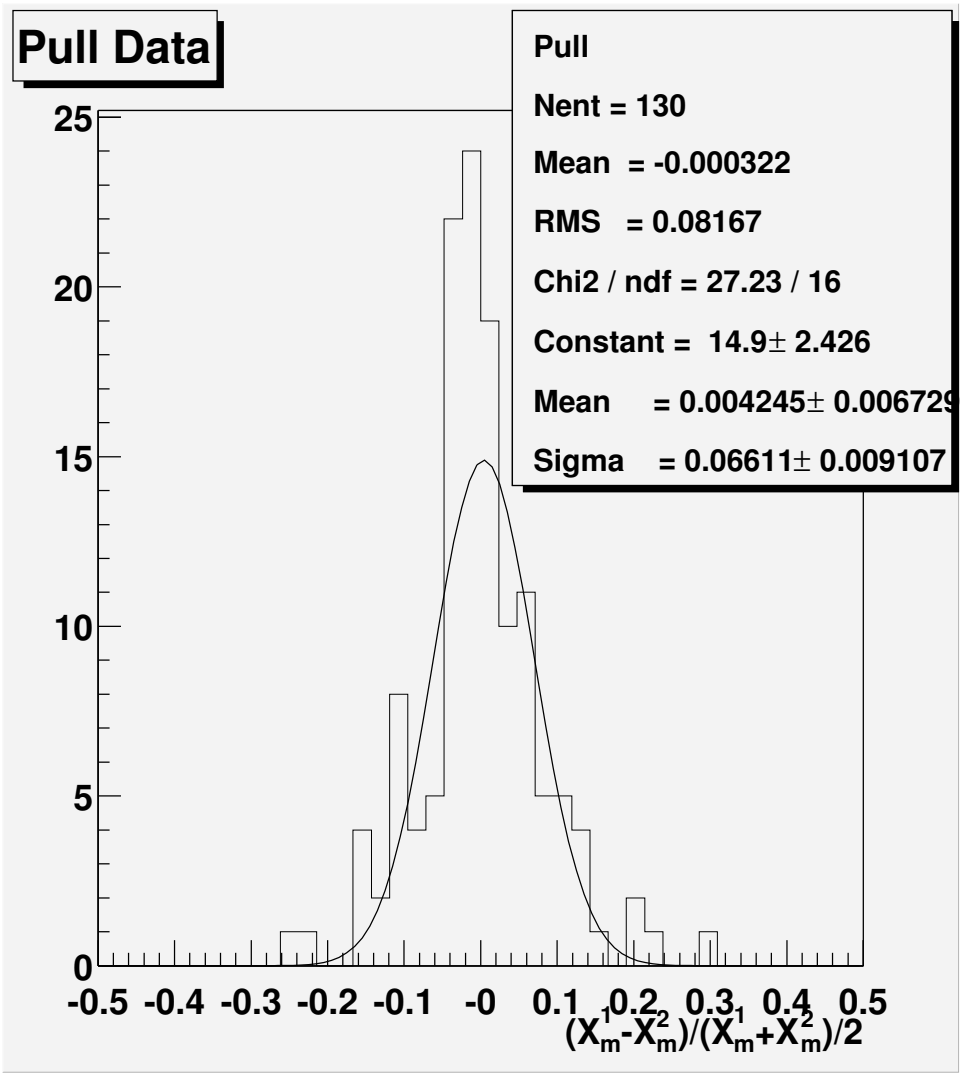

Figure 9.3. Data pull. CR events.

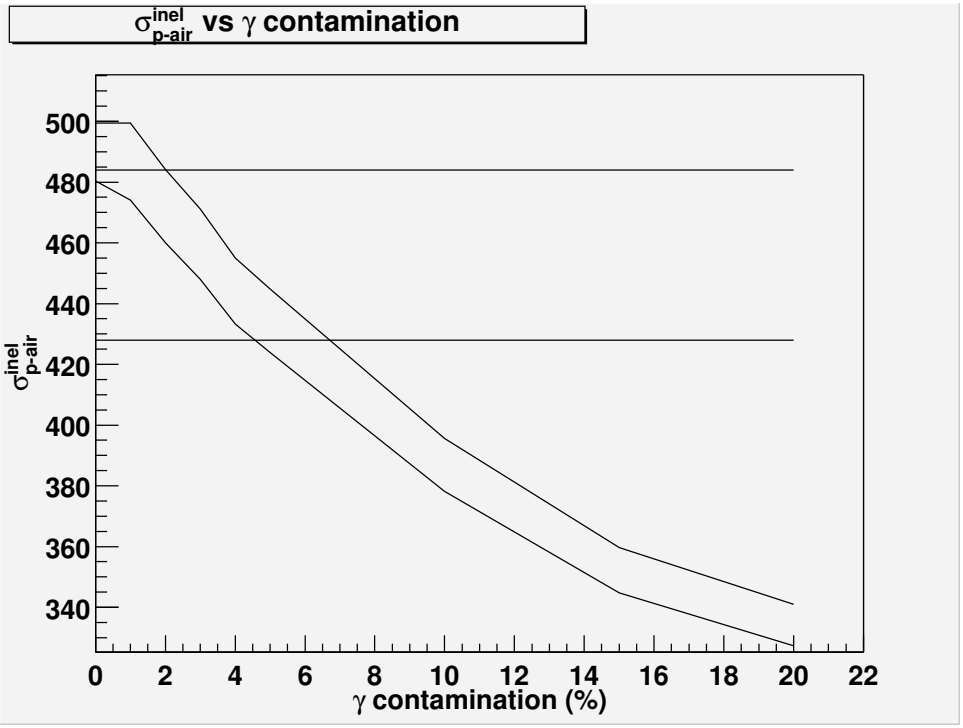

Figure 9.4. Cross-section vs gamma contamination error envelope.

One should keep in mind that the gamma ray flux contribution to the systematic error is asymmetrical. Converting p-air inelastic cross-section units we get:

$$\sigma^{inel}_{p-air} = 456 \pm 17(stat) + 39(sys) - 11(sys)mb \tag{9.1}$$

at $10^{18.5}$ eV.

9.6 Discussion

The measured value of the p-air inelastic cross-section at $10^{18.5}$ eV is in good agreement with the rising trend for the cross-section predicted by many theoretical models and previously measured using cosmic ray data at lower energies (see Figure 9.5, [90]). As was mentioned at the end of Chapter 2, previous cross-section measurements using cosmic ray data are very sensitive to the interaction model used. Rescaling the previous results with new models reduces the previous measurements by about 10-15% (see figure at the end of Chapter 2, [19]). Hoerandel [91] recently adjusted the QGSJet model to accomodate new accelerator data for the p-p cross-section measurements. The resultant plot together with this new cross-section measuremnt at $10^{18.5}$ eV is shown in Figure 9.6. We claim that the new HiRes p-air inelastic cross-section measurement is much less sensitive to

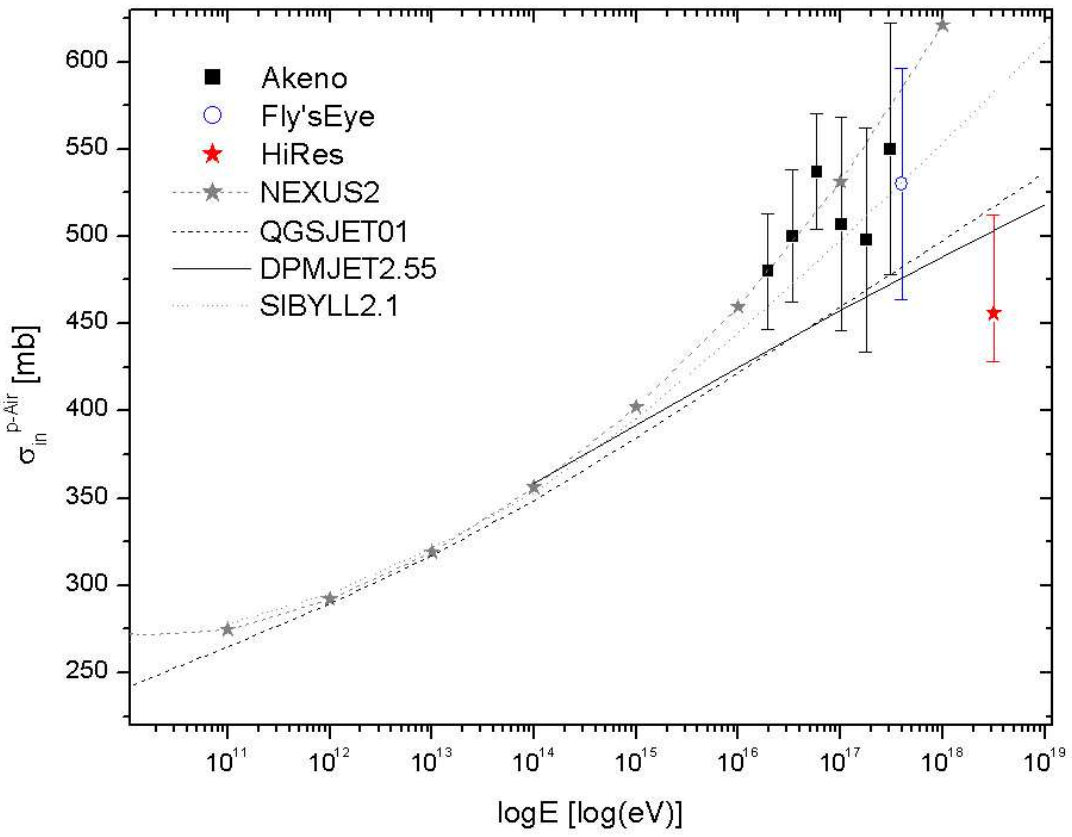

Figure 9.5. Measured cross-section in comparison.

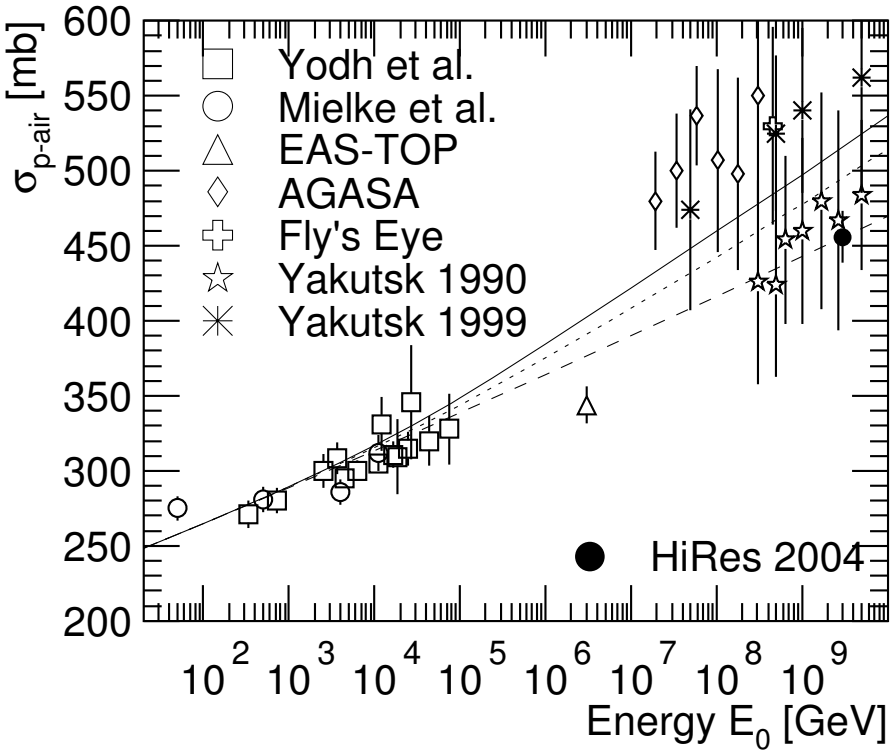

Figure 9.6. An adjusted QGSJET model and HiRes cross-section measurement.

the interaction model used for the MC simulations than the previous measurements due to the new measurement technique. This newly measured cross-section value presents a necessary check and a feedback for the old interaction models and new models to come.

REFERENCES

[1] P.G. Tinyakov and I. I. Tkachev. *JETP Lett. Pisma Zh.Eksp.Teor.Fiz.*, (74):445–448, 2001.

[2] C. Finley et al. *In preparation for Astroparticle Physics*, 2005.

[3] K. Greisen. *Physical Review Letters*, 16(17):748–750, 1966.

[4] G. T. Zatsepin and V. A. Kuzmin. *Sov. Phys. JETP Lett.*, 4(78), 1966.

[5] R. M. Baltrusaitis et al. *Phys. Rev.*, 52(1380), 1984.

[6] M. Honda et al. *Phys. Rev. Lett.*, 70(525), 1993.

[7] F. W. Stecker. *J. Phys. G: Nucl. Part. Phys.*, 29(R47-R88), 2003.

[8] A.N. Parmar, G. Gianfiglio, and J. Schiemann. *ESA Bulletin*, (110):49–55, 2002.

[9] M. J. Kidd. *Properties of Extensive Air Showers Around* $10^{17}eV$. PhD thesis, University of Illinois at Urbana-Champaign, 1997.

[10] Sandy Donnachie, Gunther Dosch, and Peter Landshoff. *Pomeron Physics and QCD*. Cambridge University Press, 2002.

[11] J. Ranft. *Phys. Rev. D*, 51(64), 1995.

[12] J. Ranft. *Preprint hep-ph/9911213*, 1999.

[13] H.J. Drescher et al. *Phys. Rep.*, 350(93), 2001.

[14] R.S. Fletcher et al. *Phys. Rev. D*, 50, 1994.

[15] R. Engel et al. In 26^{rd} *ICRC*, volume 1, page 415, 1999.

[16] J. N. Capdevielle et al. Report kfk 4998. Technical report, Kernforrschungszentrum Karlsruhe, 1992.

[17] K. Werner. *Phys. Rep.*, 232, 1993.

[18] T. K. Gaisser et al. *Phys. Rev. D*, 47:1919, 1993.

[19] M. M. Block. *Phys. Rev. D*, 62:077501, 2000.

[20] D. J. Bird et al. *Ap.J.*, 441, 1995.

[21] M. Takeda et al. *JETP Lett. Pisma Zh.Eksp.Teor.Fiz.*, (81):1163–1166, 1998.

[22] E. Fermi. *Phys. Rev.*, 75, 1949.

[23] M.S. Longair. *High Energy Astrophysics*, volume 2. Cambrige University Press, 1994.

[24] A. R. Bell. *Mon. Not. Roy. Astron.*, 182, 1978.

[25] R. D. Blanford and J. P. Ostriker. *Astrophys. J.*, 221, 1978.

[26] J. F. Ormes and J. Protheroe. *Astrophys. J.*, 272(757), 1983.

[27] J. Kota and J. R. Jokipii. *Astrophys. J.*, 265, 1983.

[28] M. E. Pesses, J. R. Jokipii, and P. Eichler. *Astrophys. J.*, 2604, 1982.

[29] J. R. Jokipii and G. E. Morfil. *Astrophys. J.*, 190, 1985.

[30] A. M. Hillas. *Nature*, (312), 1984.

[31] C. W. Misner, K. S. Torne, and J. A. Wheeler. *Gravitation.* W H Freeman, 1973.

[32] E. Witten. Superconducting strings. *Nucl. Phys.*, B249, 1985.

[33] A. Vilenkin and E. P. S. Shellard. *Cosmic Strings and Other Topological Defects.* Cambridge University Press, New York, NY., 1994.

[34] J.P. Ostriker, C. Thompson, and E. Witten. *Phys. Lett.*, B180(757), 1986.

[35] Christopher T. Hill, David N. Schramm, and Terry P.Walker. *Phys. Rev.*, D36, 1987.

[36] Zoltan Fodor, Sandor D. Katz, and Andreas Ringwald. *J. High Energy Phys.*, 046(6), 2002.

[37] S.Yoshida, G. Sigl, and S. Lee. *Phys.Rev.Lett.*, 81, 1998.

[38] Pierre Sokolsky. *Introduction to Ultrahigh Energy Cosmic Ray Physics.* Westview Press, 2004.

[39] The Auger Collaboration. *Pierre Auger Project Design Report*, 1997. Available at http://astroparticle.uchicago.edu/cosmic_ray_spectrum_picture.htm.

[40] Seo et al. *Ap.J.*, 378, 1991.

[41] M. Nagano et al. *J. Phys. G*, 10, 1984.

[42] M. Nagano et al. *J. Phys. G*, 18, 1992.

[43] D. J. Bird et al. *Ap.J.*, 424, 1994.

[44] Afanasiev et al. In *Proceedings Int. Symposium of Extremely High Energy Cosmic Rays. (ICRR Tokyo)*, page 32, 1996.

[45] Grigorov et al. In *Proceedings* 12^{th} *ICRC, Hobart*, volume 5, 1971.

[46] Lawrence, Reid, and Watson. *J. Phys. G.*, G17, 1991.

[47] Roger H. Hildebrand. *Astrophysical Letters and Communications*, 26:263–275, 1988.

[48] B. D. Fields, K. A. Olive, M. Casse, and E. Vangioni-Flam. *Astronomy Astrophysics*, 370, 2001.

[49] G. B. Christiansen, G. V. Kulikov, and Yu. A. Fomin. *Ultrahigh Energy Cosmic Rays (in Russian)*. Atomizdat, 1975.

[50] W. Springer for the HiRes collaboration. *University of Utah*, 2004.

[51] G. Archbold and the HiRes Collaboration. UHECR composition studies with hires stereo data. In 28^{rd} *ICRC*, pages 405–408, 2003.

[52] K. Kasahara. Cosmos: The user's manual. 2002.

[53] A. Haungs et al. *Nuovo Cim.*, 24C:599–605, 2001.

[54] S. J. Sciutto. Aires: A system for air shower simulations. Technical report, Auger technical note GAP 98-032, 1998.

[55] T. K. Gaisser et al. *Rev. Mod. Phys.*, (4):859–880, 1978.

[56] M. V. S. Rao and B. V. Sreekantan. *Extensive Air Showers*. World Sceintific Publishing Co. Pte. Ltd., 1998.

[57] *Extensive Air Showers*. World Scientific Publishing Co. Pte. Ltd., 1998.

[58] M. Nagano, K. Kobayakawa, N. Sasaki, and K. Ando. *arXiv:astro-ph/0406474 v1*, 2004.

[59] J. Beltz et al. Slac proposal e-165: Fluorescence in air from showers. 2002.

[60] A. N. Bunner. *The Atmosphere as a Cosmic Rays Scintillator*. PhD thesis, Cornell Univ. Ithaca, N.Y., 1964.

[61] C. R. Wilkinson. *The Application of High Precision Timing in the High Resolution Fly's Eye Cosmic Ray Detector*. PhD thesis, University of Adelaide, 1998.

[62] R. M. Baltrusaitis et al. *Nuclear Instruments and Methods in Physics Research*, A(240):410–428, 1985.

[63] D. J. Bird et al. In 23^{rd} *ICRC*, volume OG 10.2.4, pages 462–465, 1993.

[64] E. Loh, M. Cassiday, P. Sokolsky, and M. Salomon. Universitry of utah: High resolution eye proposal. 1987.

[65] K. Belov. PMT selecton for HiRes FADC mirrors. Technical report, High Energy Astrophysics Institute, 2001.

[66] Julien Girard. The hires ii fiber-optic calibration system. Master's thesis, University of Utah, 2000.

[67] J. Boyer et al. In 26^{rd} *ICRC*, volume 5, page 441, 1999.

[68] K. Belov. Study of the photo-multiplier tube response profile function. Technical report, High Energy Astrophysics Institute, 2001.

[69] S. Thomas. Hires mirror reflectivity. Technical report, University of Utah, 2004.

[70] Zhen Cao. Hires mirror reflectivity for hires data analysis. Technical report, University of Utah, 2004.

[71] J. Boyer, E. Mannel, L. Wiencke, and the HiRes Collaboration. In 28^{rd} *ICRC*, volume HE 1.3, pages 481–484, 2003.

[72] M.D. Roberts and the HiRes Collaboration. In 27^{rd} *ICRC*, pages 627–630, 2001.

[73] L. R. Wiencke and the HiRes Collaboration. In 27^{rd} *ICRC*, pages 631–634, 2001.

[74] L. R. Wiencke and the HiRes Collaboration. In 28^{rd} *ICRC*, 2003.

[75] L.R. Wiencke et al. *Nucl. Instr. Meth.*, A428, 1999.

[76] R.W. Clay, B.R. Dawson, and the HiRes Collaboration. In 27^{rd} *ICRC*, pages 649–652, 2001.

[77] *U.S. Standard Atmosphere, 1976.* U.S. Government Printing Office, Washington, D.C., 1976.

[78] J. A. J. Matthews et al. In 26^{rd} *ICRC*, volume 5, page 412, 1999.

[79] L. R. Wiencke and the HiRes Collaboration. In 27^{rd} *ICRC*, pages 635–638, 2001.

[80] A. Zech. *A Measurement of the Ultra-High Energy Cosmic Ray Flux with the HiRes FADC Detector*. PhD thesis, Rutgers University, 2004.

[81] K. Reil. *The Energy Spectrum of Ultra High Energy Cosmic Rays Measured by The High Resolution Fly's Eye Detectors*. PhD thesis, University of Utah, 2002.

[82] C. Song. *Study of Ultra High Energy Cosmic Rays with the High Resolution Fly's Eye Prototype Detector*. PhD thesis, Columbia University, 2001.

[83] Tareq AbuZayyad. *The Energy Spectrum of Ultra High Energy Cosmic Rays*. PhD thesis, University of Utah, 2000.

[84] T. K. Gaisser and A. M. Hillas. In 15^{rd} *ICRC*, page 353, 1977.

[85] J. Ranft. *Astroparticle Physics*, 14(319), 2001.

[86] K. Simpson. PhD thesis, University of Adelaide, 2001.

[87] Zhen Cao. Private conversation, University of Utah. 2003.

[88] D. E. Groom et al. *The European Physical Journal*, C15(1), 2000.

[89] T.K. Gaisser. *Cosmic Rays and Particle Physics*. Cambrige University Press, 1990.

[90] D. Heck. Private conversation, XIII ISVHECRI, Pylos, Greece. 2004.

[91] J. R. Hörandel. In *XIII ISVHECRI, Greece*, 2004.